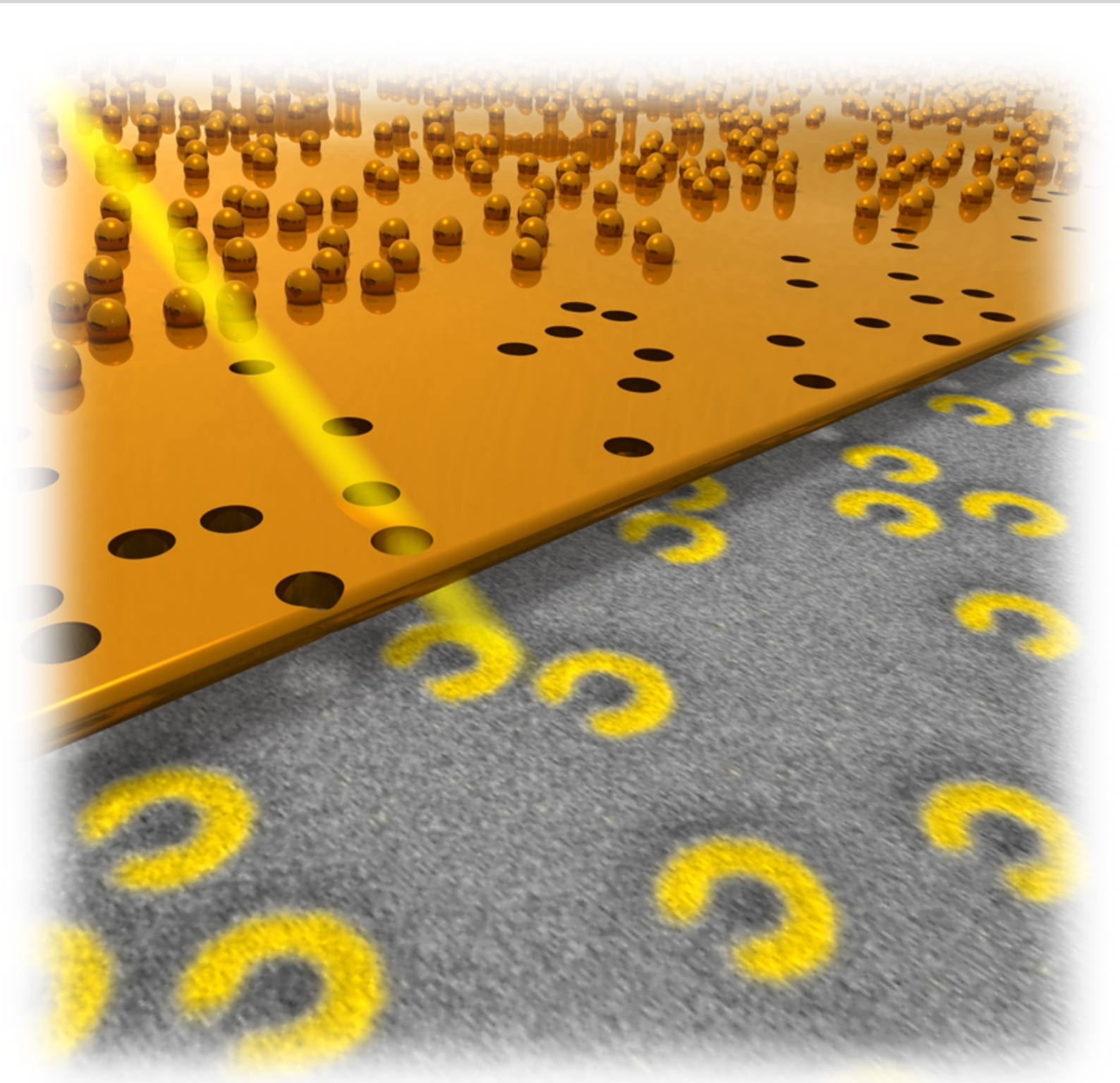


*Large-area Low-cost Fabrication of
Complex Plasmonic Nanostructures
for Sensing Applications*



Jun Zhao

Large-area Low-cost Fabrication of Complex Plasmonic Nanostructures for Sensing Applications

Von der Fakultät für Mathematik und Physik der Universität Stuttgart
zur Erlangung der Würde eines Doktors
der Naturwissenschaften (Dr. rer. nat.) genehmigte Abhandlung

vorgelegt von
Jun Zhao
aus Hubei, V. R. China

Hauptberichter: Prof. Dr. Harald Giessen
Mitberichter: Prof. Dr. Clemens Bechinger
Tag der mündlichen Prüfung: 5. Februar 2015

4. Physikalisches Institut der Universität Stuttgart
2014

Abstract

In this thesis, we introduce hole-mask colloidal lithography and nanosphere lithography techniques for low-cost nanofabrication of large-area (about 1 cm²) plasmonic nanostructures with different complex shapes. For the first one, we use thin film PMMA-gold hole-masks, which are first prepared with polystyrene colloids, combined with following tilted-angle-rotation evaporation to fabricate large-area *randomly* deposited plasmonic nanostructures. For the second one, we use hexagonal close-packed polystyrene nanosphere monolayers directly as evaporation masks to fabricate large-area *periodic* plasmonic nanostructures. We describe the fabrication process step by step, and manufacture a variety of different plasmonic nanostructures for different sensing applications. For example, we use split-ring-resonators for antenna-assisted surface-enhanced infrared absorption measurements to detect monolayer molecules with an up to 20000-fold enhancement factor. We also utilize asymmetric double split-ring-resonators for localized surface plasmon resonance sensing with experimental sensitivities of up to 520 nm/RIU and figures of merit up to 2.9. Furthermore, we investigate plasmonic oligomers consisting of touching triangular building blocks, which show fundamental modes, higher-order modes, as well as Fano resonances due to coupling between bright and dark modes within the same complex structures. Large-area low-cost direct contact Au-Pd hydrogen sensors are demonstrated, which show much improved spectral shifts as large as 30 nm upon hydrogen exposure. Additionally, we improve hole-mask colloidal lithography for three-dimensional and multishape fabrication. With multiple repetitions of hole-mask lithography, single-layer metasurfaces with complex, multi-shape plasmonic nanostructures can be created that exhibit desired optical functionalities. Large-area and low-cost fabrication of different samples with independently tunable resonances is demonstrated. These single-layer metasurfaces could find possible applications as bifunctional surface-enhanced infrared absorption and surface-enhanced Raman spectroscopy, multi-line, as well as broadband substrates. The fabrication method is particularly suited for the creation of large-area, single-layer C₃-symmetric chiral metasurfaces, and this approach circumvents common problems with elliptical birefringence and can be utilized for interaction with chiral substances.

Zusammenfassung

In dieser Arbeit führen wir zwei kostengünstige Herstellungsmethoden für großflächige (ca. 1 cm^2), komplexe, plasmonische Nanostrukturen mittels verschiedener Nanokugel-lithographietechniken ein. Für die erste Methode verwenden wir Dünnschicht-PMMA-Goldlochmasken, die mit Hilfe von Polystyrolkolloiden hergestellt werden. In Kombination mit gekipptem und rotierendem Aufdampfen lassen sich großflächige, willkürlich angeordnete, metallische Nanostrukturen herstellen. Bei der zweiten Methode verwenden wir eine hexagonal dichtest gepackte Monolage aus Polystyrolnanokugeln als Aufdampfmaske, um großflächige, periodische, plasmonische Nanostrukturen zu realisieren. Wir beschreiben den Herstellungsprozess Schritt für Schritt und die optische Eigenschaften der plasmonischen Nanostrukturen für verschiedene Anwendungen. Wir verwenden Split-Ring-Resonatoren für antennenunterstützte, oberflächenverstärkte Infrarot-Absorptionsspektroskopie an einer Molekülmonolage. Dabei untersuchen wir Streckschwingungen der aufgebrachten Moleküle und erhalten einen Verstärkungsfaktor von bis zu 20.000. Ein weiteres Beispiel sind asymmetrische Doppel-Split-Ring-Resonatoren, die für plasmonische Sensoren mit experimentellen Empfindlichkeiten von bis zu 520 nm/RIU und Gütezahlen von 2,9 verwendet werden. Außerdem untersuchen wir Oligomerstrukturen, die aus dreieckigen, sich berührenden Bausteinen bestehen. Sie zeigen die fundamentale Mode und Moden höherer Ordnung, sowie die Fano-Resonanz aufgrund der Kopplung zwischen hellen und dunklen plasmonischen Moden innerhalb derselben Strukturgeometrie. Großflächige, kostengünstige Au-Pd Wasserstoffsensoren mit einer deutlich verbesserten spektralen Verschiebungen von 30 nm bei Wasserstoffexposition werden in ihrer Herstellung und Funktion vorgestellt. Darüber hinaus erweitern wir unsere Lochmaskenlithographiemethode auf die Herstellung dreidimensionaler Strukturen und realisieren unterschiedliche Geometrien auf einem Substrat. Für eine bestimmte optische Multifunktionalität lassen sich durch wiederholtes Durchführen unseres Lochmaskenlithographieverfahrens monolagige Metaoberflächen aus komplexen, verschiedenen Nanostrukturen herstellen. Wir demonstrieren großflächige und kostengünstige Herstellung von verschiedenen Proben mit unabhängig einstellbaren Resonanzen. Diese monolagigen Metaoberflächen ermöglichen bifunktionelle oberflächenverstärkte Infrarot-Absorption und Raman-Spektroskopie, Multiresonanzen- und Breitband-Substrate. Diese Methode ist besonders gut geeignet für die Herstellung von großflächigen, einlagigen, C_3 -

symmetrischen, chiralen Metaoberflächen. Dieser Ansatz umgeht Probleme mit elliptischer Doppelbrechung und kann zur Untersuchung der Wechselwirkung mit chiralen Substanzen verwendet werden.

Publications

Part of this work have been published in the scientific journals or presented at international conferences:

- J. Zhao, S. Jaber, P. Mulvaney, P. V. Braun, and H. Giessen, *Repetitive hole-mask colloidal lithography for the fabrication of large-area low-cost plasmonic multi-shape single-layer metasurfaces*, Adv. Opt. Mater. in press (2014).
- J. Zhao, B. Frank, F. Neubrech, C. Zhang, P. V. Braun, and H. Giessen, *Hole-mask colloidal nanolithography combined with tilted-angle-rotation evaporation: A versatile methode for fabrication of low-cost and large-area complex plasmonic nanostructures and metamaterials*, Beilstein J. Nanotechnol. **5**, 577 (2014).

Video:

1. Fabrication of low-cost and large-area complex nanostructures: An overview to the concept. Beilstein TV, 2013

<http://www.beilstein.tv/tvpost/fabrication-of-low-cost-and-large-area-complex-nanostructures-an-overview-to-the-concept/> (accessed April 14, 2014)

2. Fabrication of low-cost and large-area complex nanostructures: The fabrication process step by step. Beilstein TV, 2013

[http://www.beilstein.tv/tvpost/fabrication-of-low-cost-and-large-area-complex-nanostructures-the-fabrication-process-step-by-step /](http://www.beilstein.tv/tvpost/fabrication-of-low-cost-and-large-area-complex-nanostructures-the-fabrication-process-step-by-step/) (accessed April 14, 2014)

- J. Zhao, C. Zhang, P. V. Braun, and H. Giessen, *Large-area low-cost plasmonic nanostructures in the near infrared region for Fano resonant sensing*, Adv. Mater. **24**, 247 (2012).
- S. Cataldo, J. Zhao, B. Frank, F. Neubrech, C. Zhang, P. V. Braun, and H. Giessen (The 1st and 2nd authors contributed equally to this work), *Hole-mask colloidal nanolithography for large-area low-cost metamaterials and antenna-enhanced SEIRA substrates (Cover page)*, ACS Nano **6**, 979 (2012).

- J. Zhao, B. Frank, S. Burger, and H. Giessen, *Large-area high-quality plasmonic oligomers fabricated by angle-controlled colloidal nanolithography*, ACS Nano **5**, 9009 (2011)
- J. Zhao, N. Strohfeldt, A. Tittl, and H. Giessen, *Hybrid plasmonic oligomer for large-area low-cost nano-size direct contact hydrogen sensors*, DPG Spring Meeting 2014, Dresden (Germany).
- J. Zhao, S. Jaber, P. Mulvaney, P. V. Braun, and H. Giessen, *Multilayer hole-mask colloidal nanolithography for large-area low-cost complex plasmonics*, SPIE Photonics West 2014, San Fransisco, California (USA).
- J. Zhao, S. Jaber, P. Mulvaney, P. V. Braun, and H. Giessen, *Repetitive hole-mask colloidal lithography for large-area multi-shape plasmonic nano-structures*, DPG Spring Meeting 2013, Regensburg (Germany).
- H. Giessen, J. Zhao, S. Cataldo, F. Neubrech, N. Strohfeldt, B. Frank, C. Zhang, and P. V. Braun, *Hole-mask colloidal nanolithography for large-area low-cost metamaterials and sensing applications*, SPIE Photonics West 2013, San Fransisco, California (USA).
- J. Zhao, B. Frank, S. Burger, and H. Giessen, *Fabrication of high-quality large-area plasmonic oligomers by angle-controlled colloidal nanolithography*, SPIE Photonics West 2013, San Fransisco, California (USA).
- J. Zhao, S. Cataldo, F. Neubrech, B. Frank, C. Zhang, P. V. Braun, and H. Giessen, *Hole-mask colloidal nanolithography for large-area low-cost metamaterials and antenna-enhanced SEIRA substrates*, META 2012, Paris (France).
- J. Zhao, B. Frank, and H. Giessen, *Fabrication of high-quality large-area plasmonic oligomers*, DPG Spring Meeting 2011, Dresden (Germany).
- J. Zhao, B. Frank, and H. Giessen, *Nanosphere lithography of sub-50 nm and complex plasmonic structures*, DPG Spring Meeting 2010, Regensburg (Germany).

Additional scientific publications which are not presented in this thesis:

- Z. Wang, J. Zhao, B. Frank, Q. Ran, G. Adamo, H. Giessen, and C. Soci, *Enhanced polaron photogeneration in conjugated polymers on plasmonic infrared nanoantennas*, submitted (2014).

- B. Frank, X. Yin, M. Schaeferling, J. Zhao, S. Hein, P. V. Braun, and H. Giessen, *Large-area 3D chiral plasmonic structures*, ACS Nano **7**, 6321 (2013).
- L. Fu, P. Schau, K. Frenner, H. Schweizer, J. Zhao, B. Frank, L. Wollet, P. Gaiser, B. Gompft, H. Giessen, and W. Osten *Experimental demonstration of dispersion engineering through mode interactions in plasmonic microcavities*, Proc. SPIE **8423**, 8423I (2012).
- C. Soci, Z. Wang, J. Zhao, B. Frank, Q. Ran, J. Yin, G. Adamo, H. Giessen, Plasmon-polaron coupling in conjugated polymer on resonant nanoantennas, MRS Fall Meeting 2014, Boston, Massachusetts (USA).

Contents

Abstract	iii
Zusammenfassung	iv
Publications	vi
Table of contents	ix
1 Introduction	1
2 Theoretical background	4
2.1 Optical properties of noble metals	4
2.1.1 Dielectric function of free electron metals	4
2.1.2 Drude-Sommerfeld theory	5
2.1.3 Interband transitions	7
2.2 Particle plasmons in metallic nanostructures	9
2.3 Introduction of metamaterials	12
2.4 Introduction of Fano resonances	14
3 Experimental methods	17
3.1 Large-area nanofabrications	17
3.1.1 Hole-mask colloidal lithography	17
3.1.2 Nanosphere lithography	23
3.1.3 Tilted-angle-rotation evaporation	25
3.2 Optical measurements and numerical simulation techniques	28
4 Antenna-assisted SEIRA substrates	31
4.1 Fabrication of SRR antenna	32
4.2 Detection of ODT monolayer	36
4.3 Detection of d-ODT monolayer	38
5 Asymmetric double SRRs for Fano resonant sensing	42
5.1 Optical properties of asymmetric double SRRs	43
5.2 In-situ annealing	48

5.3	Fano resonance for LSPR sensing	50
6	Complex plasmonic oligomers	53
6.1	Fabrication details for touching triangular oligomers	54
6.2	Optical properties of different oligomers	55
6.3	Self-induced Fano resonance	59
6.4	Self-induced Fano resonance for LSPR sensing	63
7	Direct contact Au-Pd sandwiches for hydrogen sensing	65
7.1	Introduction of Pd-based hydrogen sensing	65
7.2	Introduction of indirect Pd-based optical hydrogen sensing	67
7.3	Direct contact Au-Pd sandwiches for hydrogen sensing	70
8	Advanced 3D and multishape hole-mask colloidal lithography	76
8.1	3D fabrication	76
8.2	Repetitive hole-mask colloidal lithography	80
8.2.1	Control of the mask-hole densities	83
8.2.2	Correction factor for multiple evaporation	84
8.3	Multishape plasmonic nanostructures	86
8.4	Large-area C ₃ -symmetric 3D SRRs as chiral metamaterials	88
9	Summary and outlook	92
	Abbreviations	94
	Bibliography	96
	Acknowledgement	106
	Curriculum vitae	107

1 Introduction

Optics with metallic nanostructures has generated keen interest over the last few years. The resonant excitation of particle plasmons and their ability to concentrate light on subwavelength scales has led to a plethora of fundamental investigations. Initially, investigations on tuning of single and simple plasmonic nanostructures were carried out, demonstrating the tunability of particle plasmon resonances by geometrical, material, and substrate variation. Recently, more complex geometries such as dimers, oligomers, stacked and chiral structures were examined [1, 2]. Metamaterials based on metallic split-ring resonators (SRRs) were able to demonstrate simultaneously negative dielectric permittivity as well as magnetic permeability, leading to a negative refractive index [3]. First applications in the area of sensing in the visible and near-infrared spectral range as well as antenna-assisted surface-enhanced infrared absorption (SEIRA) were demonstrated [4, 5]. Also, nanoantennas with their ability to enhance light emission from single emitters as well as to concentrate incoming light into hot spots were utilized. The exceptionally large optical field enhancements in cubic-nanometer volumes has inspired researchers to construct refractive index sensors that apply localized surface plasmon resonances (LSPRs) [6]. Mode coupling, plasmon hybridization, and interaction of bright and dark modes which leads to plasmonic Fano resonances were discussed [7–9]. Single hybrid palladium (Pd) and gold (Au) systems were used as antenna-enhanced hydrogen sensor by detecting the changing optical properties [10]. The combination of plasmonic nanostructures and semiconductors led to surface plasmon lasers (SPASERs) [11, 12]. Hybrid materials that combined magneto-optical layers with plasmonic nanostructures enhanced the Faraday and magneto-optical Kerr effects [13]. Tailored nanostructures were able to lead to surface-enhanced Raman scattering (SERS), in particular when the particle plasmon resonance was tuned to the pump laser wavelength. Novel applications such as coupling of plasmons to atomic gases are on the horizon [14].

Most of these fundamental effects as well as the early applications have been demonstrated with samples fabricated by electron-beam or ion-beam lithography. These methods are quite advantageous for high-quality samples of limited size (typically on the order of $100 \times 100 \mu\text{m}^2$), but they are very costly and not really suited for mass fabrication. In particular, nanostructures with small gaps over large areas, stacked nanostructures, or multiple materials aligned with respect to each other cause major effort. Also the creation of 3D chiral materials is extremely

1 Introduction

difficult with this method [15]. An alternative method for nanofabrication includes nanoimprint lithography [16] and nanostencil-type fabrication [17], which requires a new large-area mask for every different pattern. Such masks are usually prepared also by electron-beam lithography. Direct laser writing by two-photon polymerization is a promising approach, since it allows for more flexibility and large areas, as well as for chiral structures [18–20]. However, this method is still quite costly. Interference lithography is large-area and low-cost, but only a limited range of well-ordered simple periodic structures are available, such as lines or dots [21, 22]. However, more complex shapes are required to attain the desired tailored optical functionality, which is important in the context of chiral plasmonics [23–27], plasmonic nanoantennas [28, 29], and materials for active plasmonics [30, 31].

Here, we present hole-mask colloidal lithography [32–34] and nanosphere lithography [35–37] techniques, combined with tilted-angle-rotation evaporation [38] for really low-cost fabrication of large-area nanostructures with flexible complex geometries. Our methods are low-cost, as they can be added simply to standard thermal or electron-gun evaporators, flexible, as programming of stepper motors allows for complex patterns, and capable of exact positioning of multiple materials in sub-10 nm vicinity over large areas (we usually use 1 cm² substrates). These methods permit the manufacturing of nanoantennas for nanoplasmonic hydrogen sensing [39, 40], and 3D plasmonic nanostructures [41]. Also, they have been used for the creation of nanodimer colour routers [33], metamaterials nanosandwiches [42], combining various feature sizes on one surface [43], and multielement antennas [44, 45].

In chapter 2, we introduce at first the optical properties of noble metals such as gold and silver, which are used as main materials for plasmonics. Using the Drude-model we can describe the dielectric function of noble metals. Subsequently, we calculate the particle plasmon resonance in metallic nanostructures using their dielectric function. At the end of this chapter, some basics on metamaterials and Fano resonances are introduced.

In chapter 3, the large-area manufacturing processes are explained in detail, which consist of mask preparation and subsequent tilted-angle-rotation evaporation, followed by a lift-off and cleaning procedure. At the end of this chapter, the setup used for optical characterization and numerical simulation techniques are described.

Afterwards different types of plasmonic nanostructures are investigated, including their optical properties and for different sensing applications. In chapter 4, we introduce antenna-assisted SEIRA measurement for detecting a monolayer of molecules using SRR antennas.

In chapter 5, asymmetric double split-ring resonators (ADSRs) are shown. During the variation of the asymmetric degree and the time-dependent in-situ

1 Introduction

annealing, the evolution of the Fano resonance for refractive index sensing in the near infrared is demonstrated.

Complex plasmonic oligomers are studied in chapter 6, including the fabrication details for the touching triangular oligomers and the optical properties for variant structure geometries. Self-induced Fano resonances are discussed for LSPR sensing.

In chapter 7, large-area low-cost hydrogen nanoplasmonic sensing are demonstrated using direct contact hybrid Au-Pd sandwich systems, which show more improved spectral signal and LSPR shifts as large as 30 nm.

In chapter 8, some advanced and improved large-area fabrication details are introduced, including 3D and multishape techniques. Even more flexible designs of plasmonic nanostructures are demonstrated, as well as the realization of the first large-area truly chiral C_3 -symmetric metamaterials.

2 Theoretical background

The interaction of metals with electromagnetic radiation results from the existence of free conduction electrons in the metal [46]. At optical frequencies, an incident electromagnetic wave can excite collective charge-density oscillations at the surface with definite resonance frequencies, which are called surface plasmons. The existence of plasmons is characteristic for the interaction of metallic nanostructures with light [47]. The accumulation of the individual nanostructure elements with nanoscale period are called metamaterials, if their characteristic period is substantially smaller than the light wavelength.

2.1 Optical properties of noble metals

2.1.1 Dielectric function of free electron metals

The optical properties of metals can be described by a complex dielectric function, which depends on the frequency of light [48]. In macroscopic electrodynamics the electromagnetic properties of the medium are mostly discussed in terms of the macroscopic polarization \vec{P} according to

$$\vec{D}(\omega) = \epsilon_0 \vec{E}(\omega) + \vec{P}(\omega), \quad (2.1)$$

where \vec{D} denotes the electric displacement, \vec{E} the electric field, and ϵ_0 the permittivity of vacuum. With the constitutive relation

$$\vec{D}(\omega) = \epsilon_0 \epsilon(\omega) \vec{E}(\omega), \quad (2.2)$$

where ϵ is the permittivity of metal, we have

$$\vec{D}(\omega) = \epsilon_0 \epsilon(\omega) \vec{E}(\omega) = \epsilon_0 \vec{E}(\omega) + \vec{P}(\omega). \quad (2.3)$$

The presence of an electric field leads to a displacement \vec{r} of an electron, which is associated with a dipole moment $\vec{\mu}$ according to $\vec{\mu} = e\vec{r}$. The cumulative effect of all individual dipole moments of all free electrons results in $\vec{P} = n\vec{\mu}$, where n is the number of electrons per unit volume. Otherwise, \vec{P} can be expressed as:

$$\vec{P}(\omega) = \epsilon_0 \chi_e(\omega) \vec{E}(\omega), \quad (2.4)$$

2 Theoretical background

where $\chi_e(\omega)$ is the electric susceptibility. From this we calculate the frequency dependent dielectric function of the metal:

$$\epsilon(\omega) = 1 + \chi_e(\omega). \quad (2.5)$$

By solving the equation of the Drude-Sommerfeld model, \vec{r} and therefore \vec{P} and χ_e can be calculated.

2.1.2 Drude-Sommerfeld theory

In the Drude-Sommerfeld theory the macroscopic response of the metal is determined by multiplying the effect of a single free electron to the external force by the number of electrons, and we consider only the effects of the free electrons [49]. The equation of motion for one electron driven by the field $\vec{E}_0 e^{-i\omega t}$ can be written as:

$$m_e \frac{\partial^2 \vec{r}}{\partial t^2} + m_e \Gamma \frac{\partial \vec{r}}{\partial t} = e \vec{E}_0 e^{-i\omega t}, \quad (2.6)$$

where m_e is the effective mass of the free electrons and e is the electron charge, and \vec{E}_0 and ω are the amplitude and frequency of the applied electric field. Γ denotes the damping constant, with $\Gamma = \frac{v_F}{l}$, where v_F is the Fermi velocity and l is the electron mean free path between scattering events. Solving Eq. 2.6 with the ansatz $\vec{r}(t) = \vec{r}_0 e^{-i\omega t}$ and using the results from chapter 2.1.1 yields:

$$\epsilon_{Drude}(\omega) = 1 - \frac{\omega_p^2}{\omega^2 + i\Gamma\omega} = 1 - \frac{\omega_p^2}{\omega^2 + \Gamma^2} + i \frac{\Gamma\omega_p^2}{\omega(\omega^2 + \Gamma^2)}. \quad (2.7)$$

Here $\omega_p = \sqrt{ne^2/(m_e\epsilon_0)}$ is the Drude plasma frequency. The real and imaginary part of the dielectric function for free electron metals can be simplified as:

$$Re(\epsilon_{Drude}) = 1 - \frac{\omega_p^2}{\omega^2 + \Gamma^2}, \quad (2.8)$$

$$Im(\epsilon_{Drude}) = \frac{\Gamma\omega_p^2}{\omega(\omega^2 + \Gamma^2)}. \quad (2.9)$$

As described in chapter 2.1.1, the dielectric function $\epsilon(\omega)$ is also expressed in terms of the susceptibility as $\epsilon(\omega) = 1 + \chi_e(\omega)$. For free electron metals in the Drude-Sommerfeld model, the susceptibility can be written as:

$$\chi_{Drude}(\omega) = -\frac{\omega_p^2}{\omega^2 + i\Gamma\omega}. \quad (2.10)$$

2 Theoretical background

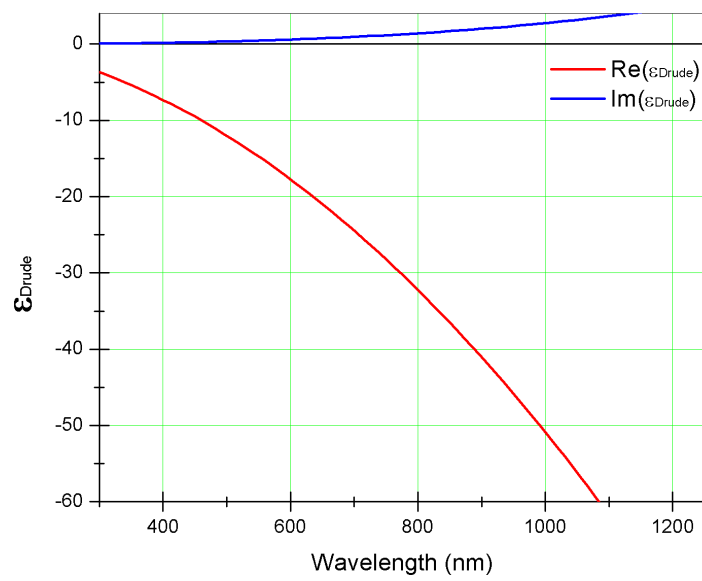


Figure 2.1: The real and imaginary part of the dielectric function for gold according to the Drude-Sommerfeld free-electron model ($\hbar\omega_p = 8.95$ eV, $\hbar\Gamma = 65.8$ meV).

2 Theoretical background

Using the free parameters $\hbar\omega_p = 8.95$ eV and $\hbar\Gamma = 65.8$ meV for gold [46], the real and imaginary part of the dielectric function for solid gold are plotted in Figure 2.1 as functions of wavelength. As shown in this diagram, the real part of the dielectric constant is negative, which gives rise to a strong imaginary part of the refractive index $n = \sqrt{\epsilon}$. This behavior leads to the result that light can penetrate a metal only to a very small extent. The imaginary part of ϵ describes the dissipation of energy in metal, due to the motion of electrons. The Drude-Sommerfeld model gives quite precise results in the infrared range. However, for wavelengths below 650 nm, interband transitions dominate the dielectric function, and the Drude-Sommerfeld model is no longer valid, which will be discussed in the next chapter.

2.1.3 Interband transitions

For noble metals the electrons in lower energy levels can also contribute to the dielectric function [48]. In the visible range we should consider the response of bound electrons as well, because higher-energy photons can excite the electrons of lower energy band into the conduction band. With the same method as for the free electrons, the equation of motion for a bound electron can be written as:

$$m \frac{\partial^2 \vec{r}}{\partial t^2} + m\gamma \frac{\partial \vec{r}}{\partial t} + \alpha \vec{r} = e \vec{E}_0 e^{-i\omega t}. \quad (2.11)$$

Here m is the effective mass of the bound electrons, γ is the radiative damping of the bound electrons, and α is the spring constant of the potential which keeps the electron in place. Using the same ansatz $\vec{r}(t) = \vec{r}_0 e^{-i\omega t}$ we can solve this equation and find the contribution of bound electrons to the dielectric function:

$$\epsilon_{Interband}(\omega) = 1 + \frac{\tilde{\omega}_p^2}{(\omega_0^2 - \omega^2) - i\gamma\omega}. \quad (2.12)$$

Here $\tilde{\omega}_p = \sqrt{\tilde{n}e^2/(m_e\epsilon_0)}$ is with \tilde{n} being the density of the bound electrons and $\omega_0 = \sqrt{\frac{\alpha}{m}}$. In this case, the susceptibility is denoted as:

$$\chi_{Interband}(\omega) = \frac{\tilde{\omega}_p^2}{(\omega_0^2 - \omega^2) - i\gamma\omega}. \quad (2.13)$$

We can also separate equation 2.12 into real and imaginary part:

$$Re(\epsilon_{Interband}) = 1 + \frac{\tilde{\omega}_p^2(\omega_0^2 - \omega^2)}{(\omega_0^2 - \omega^2)^2 + \gamma^2\omega^2}, \quad (2.14)$$

$$Im(\epsilon_{Interband}) = \frac{\gamma\tilde{\omega}_p^2\omega}{(\omega_0^2 - \omega^2)^2 + \gamma^2\omega^2}. \quad (2.15)$$

2 Theoretical background

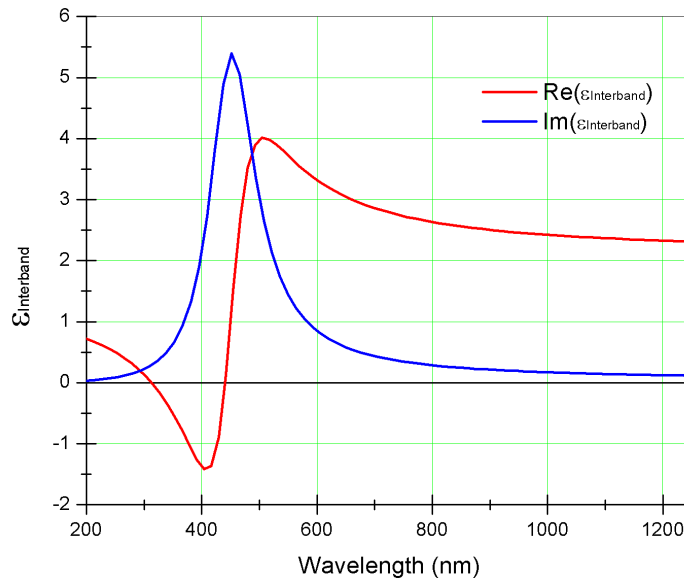


Figure 2.2: Contribution of bound electrons to the dielectric function of gold ($\hbar\tilde{\omega}_p = 2.96$ eV, $\hbar\gamma = 0.59$ eV and $\omega_0 = 2\pi c/\lambda$, with $\lambda = 450$ nm).

2 Theoretical background

These results are shown in Figure 2.2. For the imaginary part we observe clearly a resonance, and for the real part a dispersion-like behavior is observed.

In order to determine all optical properties of metals around the visible region, including optical absorption, we have to add the free-electron contribution and the contribution of a single interband transition.

$$\epsilon(\omega) = 1 + \chi_{Drude}(\omega) + \chi_{Interband}(\omega). \quad (2.16)$$

Figure 2.3 [46] shows the model of the dielectric function taking into account the contribution of free electrons and a single interband transition (Eq. 2.16), as well as the experimental values taken from the paper of Johnson and Christy for gold [50]. For wavelength above 650 nm the real and imaginary part of the dielectric function clearly follow the Drude-Sommerfeld theory. For wavelength below 650 nm the interband contribution to ϵ becomes dominant. Since only one interband transition is taken into account, the model curves still fail to reproduce the data below 500 nm. Here we must add up a defined constant offset $\epsilon_\infty = 6$, which accounts for all the other higher-energy interband transitions [50].

2.2 Particle plasmons in metallic nanostructures

In the discussion of the particle plasmons in metallic nanostructures, we use a quasi-static approximation and neglect the retardation, because the characteristic size of the structures is much smaller than the wavelength of light [51]. When a metal particle is placed in an electric field, surface polarization is induced as shown in Figure 2.4.

By solving the Laplace equation, we calculate the quasi-static near-fields and scattering cross-sections of the considered objects. The electric field of an oscillating dipole at the position $r\vec{n}$ is approximated with $kr \ll 1$ as:

$$\vec{E}(r\vec{n}, t) = \frac{1}{4\pi\epsilon_0} [3\vec{n}(\vec{n} \cdot \vec{\mu}) - \vec{\mu}] \frac{e^{i\omega t}}{r^3}, \quad (2.17)$$

with $\vec{\mu}$ denoting the dipole moment. We represent the electric field by a potential Φ as $\vec{E} = -\nabla\Phi$, which has to satisfy the Laplace equation:

$$\nabla^2\Phi = 0, \quad (2.18)$$

and the boundary conditions between adjacent materials. As an example we analyze the solution of the Laplace equation for a small metallic spherical particle with radius a . Here we express the Laplace equation in spherical coordinates (r, θ, φ) :

$$\frac{1}{r^2 \sin \theta} \left[\sin \theta \frac{\partial}{\partial r} \left(r^2 \frac{\partial}{\partial r} \right) + \frac{\partial}{\partial \theta} \left(\sin \theta \frac{\partial}{\partial \theta} \right) + \frac{1}{\sin \theta} \frac{\partial^2}{\partial \varphi^2} \right] \Phi(r, \theta, \varphi) = 0. \quad (2.19)$$

2 Theoretical background

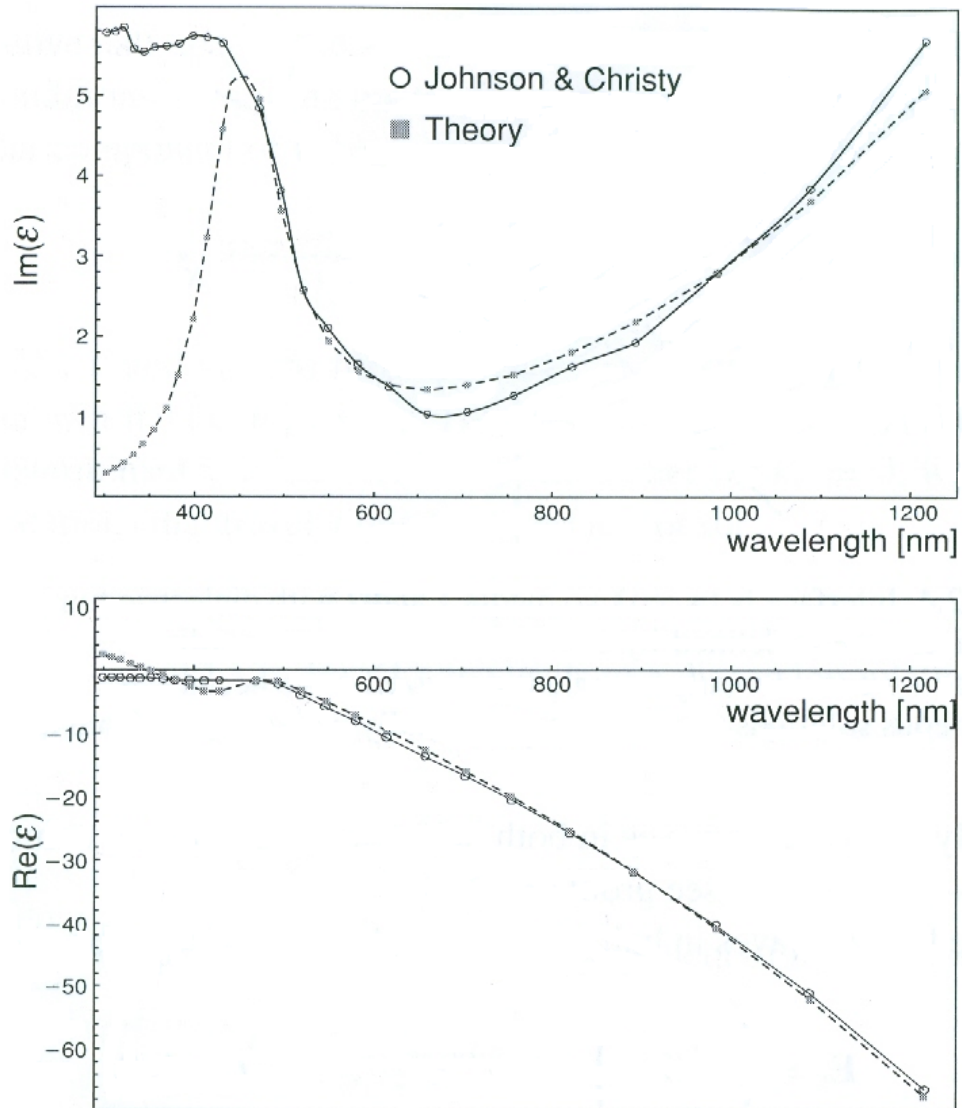


Figure 2.3: Dielectric function of gold. Open circles: Experimental values taken from [50]. Squares: Model of the dielectric function, taking into account the free-electron contribution and the contribution of a single interband transition [46].

2 Theoretical background

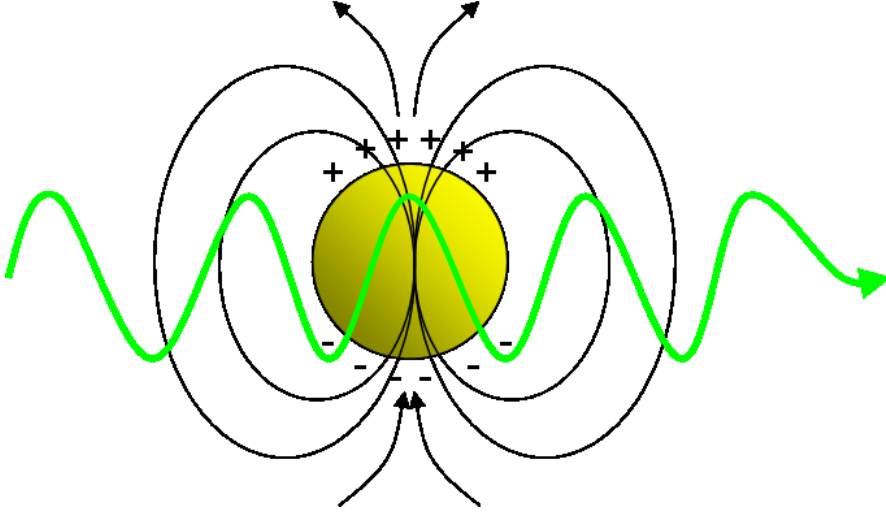


Figure 2.4: A dipolar surface plasmon excitation in a spherical particle by the electric field of the incident light.

Using the ansatz $\Phi(r, \theta, \varphi) = \sum_{l,m} b_{l,m} \cdot \Phi_{l,m}(r, \theta, \varphi)$ and considering the continuity of the tangential electric fields and the normal components of the electric displacements at the surface of the sphere,

$$\left[\frac{\partial \Phi_1}{\partial \theta} \right]_{r=a} = \left[\frac{\partial \Phi_2}{\partial \theta} \right]_{r=a}, \quad \epsilon_1 \left[\frac{\partial \Phi_1}{\partial r} \right]_{r=a} = \epsilon_2 \left[\frac{\partial \Phi_2}{\partial r} \right]_{r=a}, \quad (2.20)$$

the potential inside the sphere Φ_1 and outside the sphere Φ_2 can be calculated. Here ϵ_1 is the dielectric constant of metal, which is expressed as a function of frequency of the electric field, and ϵ_2 denotes the dielectric constant of the surrounding medium around the metallic sphere. The potential outside the sphere consists of the potential of the incoming and the scattered fields: $\Phi_2 = \Phi_{scatter} + \Phi_0$. Therefore the electric fields inside and outside the sphere are calculated as:

$$\Phi_1(r, \theta) = -\frac{3\epsilon_2}{\epsilon_1 + 2\epsilon_2} E_0 r \cos \theta, \quad (2.21)$$

$$\vec{E}_1 = E_0 \frac{3\epsilon_2}{\epsilon_1 + 2\epsilon_2} \vec{n}_x, \quad (2.22)$$

$$\Phi_2(r, \theta) = -E_0 r \cos \theta + \frac{\epsilon_1 - \epsilon_2}{\epsilon_1 + 2\epsilon_2} \frac{a^3 \cos \theta}{r^2} E_0. \quad (2.23)$$

$$\vec{E}_2 = E_0 \vec{n}_x + \frac{\epsilon_1 - \epsilon_2}{\epsilon_1 + 2\epsilon_2} \frac{a^3}{r^3} E_0 (2 \cos \theta \vec{n}_r + \sin \theta \vec{n}_\theta). \quad (2.24)$$

2 Theoretical background

We find that the scattered field (second term in Eq. 2.22) is identical to the electrostatic field of a dipole $\vec{\mu}$ located at the center of the sphere, which is induced by an external field \vec{E}_0 . With $\Phi = \frac{\vec{\mu} \cdot \vec{r}}{4\pi\epsilon_0\epsilon_2 r^3}$ and $\vec{\mu} = \epsilon_2\alpha(\omega)\vec{E}_0$, we calculate the polarizability α as

$$\alpha(\omega) = 4\pi\epsilon_0 a^3 \frac{\epsilon_1(\omega) - \epsilon_2}{\epsilon_1(\omega) + 2\epsilon_2}. \quad (2.25)$$

The scattering cross-section of the sphere is then expressed as

$$\sigma_{scatt} = \frac{k^4}{6\pi\epsilon_0^2} |\alpha(\omega)|^2 = \frac{8\pi}{3} k^4 a^6 \left| \frac{\epsilon_1(\omega) - \epsilon_2}{\epsilon_1(\omega) + 2\epsilon_2} \right|^2, \quad (2.26)$$

where k is the wavevector in the surrounding medium. The resonance condition for this equation is reached when the denominator is around zero:

$$\epsilon_1(\omega) + 2\epsilon_2 \approx 0. \quad (2.27)$$

When this condition is fulfilled, the cross-section of the spherical particle is at its maximum. Because of the sensitive dependence of the particle plasmon resonance on the dielectric constant of the surrounding, metallic nanostructures can be used as a sensing element, for example to detect biopolymers such as DNA or proteins [52].

2.3 Introduction of metamaterials

In 1967 has Victor Veselago postulated that it should be possible to achieve a negative index of refraction with negative permeability and negative permittivity for certain frequencies [53]:

$$n = -\sqrt{\epsilon\mu}. \quad (2.28)$$

There are no materials in nature which fulfill these two conditions. The problem is that in natural materials the basic electrical and magnetic resonances do not occur at the same frequency. The resonances, which have an electric polarization result, are at very high frequencies, for metals in the visible, and for semiconductors even in the THz and IR range. But, on the other hand, in magnetic systems the resonances occur in a much lower frequency regime.

In order to obtain negative permeability and permittivity at the same frequency, one needs to produce a new class of artificial materials, which are called metamaterials. Meta means in this context that the materials possess properties which are beyond the usual and customary situations [54]. To realize such an artificial material, a large number of single elements has to be arranged in a lattice. The incident radiation can not distinguish the accumulation of the individual

2 Theoretical background

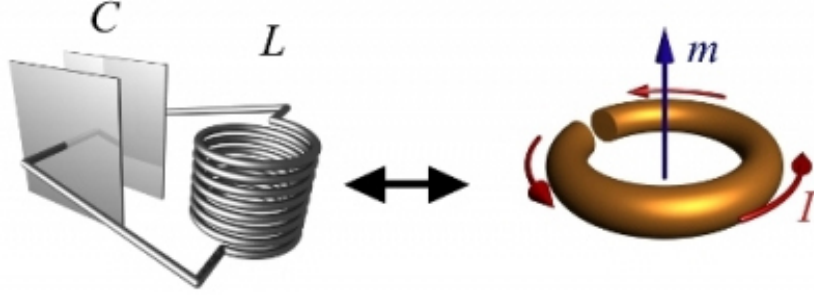


Figure 2.5: A conventional LC-circuit and schematic diagram of an SRR [57].

elements from a homogeneous material, as long as the size and spacing of the elements are much smaller than the wavelength of the incident light.

Metamaterials can be also represented by different classes [55]. These metamaterials, in which both permittivity and permeability are negative resulting in a negative index of refraction, can be referred to as double negative metamaterials or negative index metamaterials. With such metamaterials new interesting applications become possible, such as perfect lenses or optical cloaks [56]. The best known example of such metamaterials are the metallic split-ring resonators, which can be used for sensing as introduced in chapter 4 and 5.

In order to describe the resonance behavior of SRR structures, we use a simple quasi-static LC-circuit model. To enable magnetism at optical frequencies, magnetic dipoles are required, which can couple to the external field. Here, the magnetic dipole can be seen as a microscopic electric circuit current, which is induced by an incident electromagnetic field. Thus, we will model a ring structure as a single winding of an inductance loop. As shown in Figure 2.5, the gap of the SRR can be considered as a capacitance [57]. Both of them together constitute an LC-circuit. When the magnetic field of the incident light oscillates perpendicularly to the SRR plane, the LC oscillator with eigenfrequency $\omega_{LC} = 1/\sqrt{LC}$ can couple to the external electromagnetic field.

For different polarizations, i.e., E-field vector parallel or perpendicular to the gap of the SRR, there are different resonant frequencies. Figure 2.6a shows a fundamental plasmon mode of a SRR, which is excited by the light polarized parallel to the gap. At the ends of the ring an electric dipole is formed through charge displacement. This electric dipole oscillates with the corresponding resonant frequency over the entire ring, and the corresponding frequency is the lowest. Due to the current in the ring, a magnetic dipole moment perpendicular to the plane of

2 Theoretical background

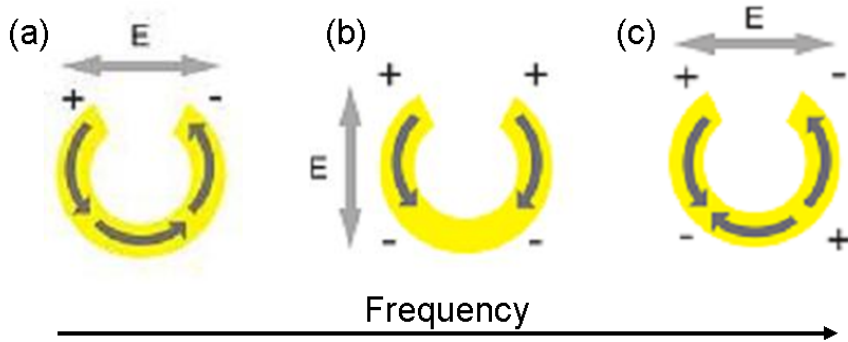


Figure 2.6: SRR resonances excited by the incident light with oscillating electric field parallel or perpendicular to the split of SRRs.

the ring is also generated, so this resonance also can be regarded as magnetic dipole resonance. Therefore, at this frequency range, both the electric and magnetic resonances are excited simultaneously, leading to a negative permittivity, as well as a negative permeability.

For light polarized perpendicular to the gap, there is a different charge distribution in the SRR (see Fig. 2.6b), and the magnetic resonance is completely suppressed. In this case, one can obtain two dipoles oscillating parallel to the E-field vector. Here, the charge oscillates over a shorter distance, therefore the resonance occurs at a higher frequency.

For the light polarized parallel to the gap, additionally higher order modes can occur, as shown in Fig. 2.6c, which oscillate over even shorter distances and hence have higher resonance frequencies.

If only permittivity is negative while permeability is positive, these metamaterials are called single negative metamaterials, for example some plasmonic nanostructures made of noble metals such as gold or silver. In the past few years, several different geometries were proposed, for example, spheres with a large dielectric constant [58], or a pair of small parallel metal wires [59]. In chapter 6 - 8 we will study some other complex plasmonic nanostructures.

2.4 Introduction of Fano resonances

Asymmetric resonances were first observed by Wood in 1902 [60], when white light illuminated metallic diffraction gratings. Ugo Fano derived theoretically in 1936 the resonant behavior. The Fano formula [61] was developed to characterize the asymmetric line shapes resulting from interference between a background and a resonant scattering process. The Fano resonance in plasmonic nanostructures,

2 Theoretical background

which is usually defined as the interference of a broad bright mode with a narrow dark mode, can be fitted and described well with the Fano formula [62]. As introduced in [63–65], a classical harmonic oscillator model was used as common approach in photonics.

In a classical system of two coupled oscillators (as shown in Figure 2.7a) with respective resonance frequency ω_1 and ω_2 , the motion can be described with the equations:

$$\ddot{x}_1 + \gamma_1 \dot{x}_1 + \omega_1^2 x_1 + g x_2 = f e^{i\omega t} \quad (2.29)$$

$$\ddot{x}_2 + \omega_2^2 x_2 + g x_1 = 0. \quad (2.30)$$

The energy loss of the oscillator 1 is modeled by the damping constant γ_1 , and the coupling between the two oscillators is defined using a constant g . $f e^{i\omega t}$ is considered as a harmonic external force driving on the oscillator 1. For the displacements x_1 and x_2 of the oscillators, a harmonic response is assumed with $x_1 = a e^{i\omega t}$ and $x_2 = c e^{i\omega t}$. Solving the equations 2.27 and 2.28, the amplitude of the spectral response of the oscillator 1 is given by:

$$a = \frac{\omega_2^2 - \omega^2}{(\omega_1^2 + i\gamma_1\omega - \omega^2)(\omega_2^2 - \omega^2) - g^2} f. \quad (2.31)$$

Around ω_2 , the two oscillators interfere destructively and constructively, depending on the exact spectral position below and above resonance, giving rise to an asymmetric resonance. As $\gamma_1 \ll \omega_1$, in a small frequency range around ω_2 , $\omega_1^2 + i\gamma_1\omega - \omega^2$ changes very slowly and therefore can be considered as constant with $C \equiv \omega_1^2 + i\gamma_1\omega - \omega^2$. Together with neglecting second-order contributions from γ_1 and γ_2 , one obtains from equation 2.29:

$$|a|^2 \frac{|C|^2}{|f|^2} = \frac{(\kappa + q)^2}{\kappa^2 + 1}, \quad (2.32)$$

which gives the classical equivalent of the Fano formula around the resonance frequency of oscillator 2, where $\kappa = (\omega^2 - \omega_2^2 - \omega_2\Delta)/\Gamma$ is the reduced frequency, $\Delta = [(\omega_2^2 - \omega_1^2)g^2]/(|C|^2 \omega_2)$ is the resonance shift, $\Gamma = \gamma_1 \omega_2 g^2 / |C|^2$ is the resonance width, and $q = (\omega_2^2 - \omega_1^2)/(\gamma_1 \omega_2)$ is the asymmetry parameter.

Recently, Benjamin Gallinet and Olivier J. F. Martin have improved the Fano formula using two harmonic oscillators with italic losses. As derived in [9], the equations of motion can be then written as:

$$\ddot{x}_1 + \gamma_1 \dot{x}_1 + \omega_1^2 x_1 + g x_2 = f e^{i\omega t} \quad (2.33)$$

$$\ddot{x}_2 + \gamma_2 \dot{x}_2 + \omega_2^2 x_2 + g x_1 = 0. \quad (2.34)$$

2 Theoretical background

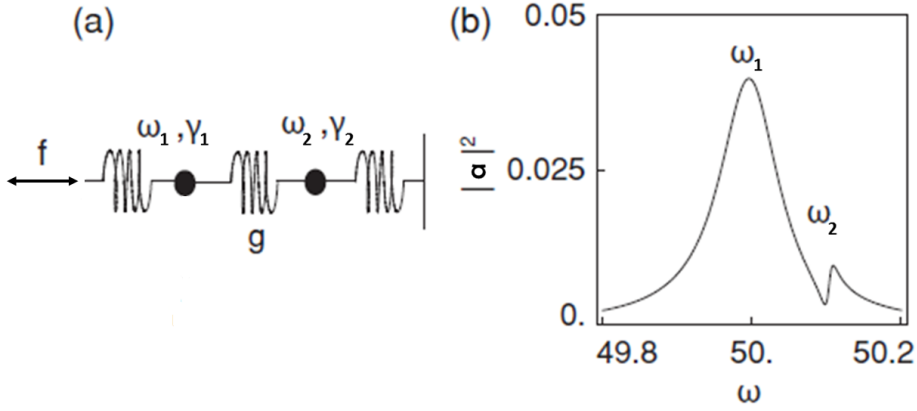


Figure 2.7: (a) Classical mechanical model of Fano resonances: two coupled oscillators of frequencies ω_1 and ω_2 , and damping γ_1 and γ_2 . The oscillator 1 is driven by an external force f , and the coupling strength is described with a constant g . (b) The square of the amplitude a^2 of the first oscillator as a function of the excitation frequency ω [9].

Oscillator 1 models the bright mode with a high damping γ_1 , representing radiative losses, whereas oscillator 2 models the mostly nonradiative dark mode with low damping γ_2 , representing intrinsic and possible radiation losses. Using the same ansatz and assumption as introduced before, one obtains the improved Fano formula [9]:

$$|a|^2 \frac{|C|^2}{|f|^2} = \frac{(\kappa + q)^2 + b}{\kappa^2 + 1}, \quad (2.35)$$

where $b = \gamma_2^2 |C|^4 / (\gamma_1^2 g^4)$ is the screening parameter. The square of the amplitude of the forced oscillator is plotted in Figure 2.7b as a function of the excitation frequency for $\omega_1 = 50.0$, $\omega_2 = 50.1$, $g = 2.0$, $\gamma_1 = 0.1$, and $\gamma_2 = 0.01$. This Fano formula fits the spectral response in plasmonic nanostructures more accurately. It is also suited for the description of interaction of plasmonic nanostructures with vibrational molecules.

3 Experimental methods

In this chapter, the used experimental techniques and numerical simulation methods are explained in detail. For the fabrication of large-area plasmonic nanostructures, we prepare first an evaporation mask using polystyrene (PS) nanospheres. Then we use tilted-angle-rotation thermal evaporation in high vacuum to fabricate different complex plasmonic nanostructures. In order to determine the optical response of the prepared structures, we measure the reflection or transmission spectra with Fourier transform infrared (FTIR) spectroscopy. For numerical simulations of the spectra we use the software CST Microwave Studio.

3.1 Large-area nanofabrications

For both large-area nanofabrication techniques, hole-mask and nanosphere lithography, an evaporation mask is required, which is prepared using PS spheres. For hole-mask colloidal lithography, we fabricate a thin layer of gold hole-mask above the substrate, whereas for nanosphere lithography we deposit a monolayer of hexagonal close-packed PS spheres on substrates and use it directly as a mask. The subsequent evaporation process is identical for both methods.

3.1.1 Hole-mask colloidal lithography

PMMA spin coating Before the hole-mask fabrication, all substrates are cleaned with acetone and isopropanol in an ultrasonic bath for about 5 minutes, respectively, and then dried with nitrogen gas. In addition, glass substrates are functionalized directly after the cleaning process with 20 μ l isobutyl(trimethoxy)silane (Sigma Aldrich) in 10 ml toluene solution for about 8 hours to improve adhesion of a polymer layer on them. Afterwards, a layer of poly(methylmethacrylate) (PMMA) is spin coated onto the substrate (see Figure 3.1a). For a homogeneous PMMA layer, which is very important for the following preparation process, the dropping of the PMMA solution onto the substrate should be stable and continuous, with 2 or 3 droplets for each one. Figure 3.2 shows the spin coated PMMA layer on Si substrates. From left to right are homogeneous and successfully spin coated sample, substrate with too little PMMA solution, dirty substrate with dust on it before spin coating, and dirty substrate with fat from

3 Experimental methods

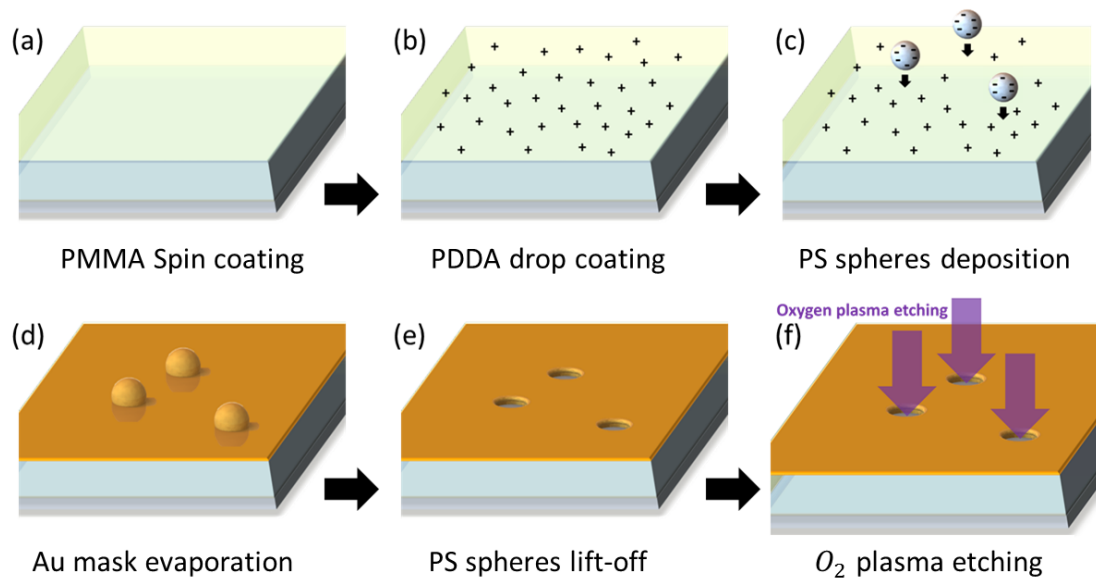


Figure 3.1: Hole-mask fabrication scheme. (a) Deposition of sacrificial PMMA layer. (b) Drop coating of positive charged PDDA solution. (c) Deposition of negative charged polystyrene spheres in a randomly distributed arrangement. (d) Evaporation of oxygen plasma resistant gold mask. (e) Removing polystyrene spheres with ultrasonic bath. (f) isotropic dry etching.

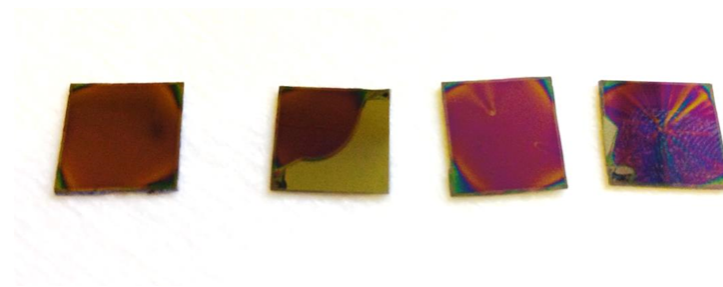


Figure 3.2: The spin coated PMMA layers on Si substrates.

3 Experimental methods

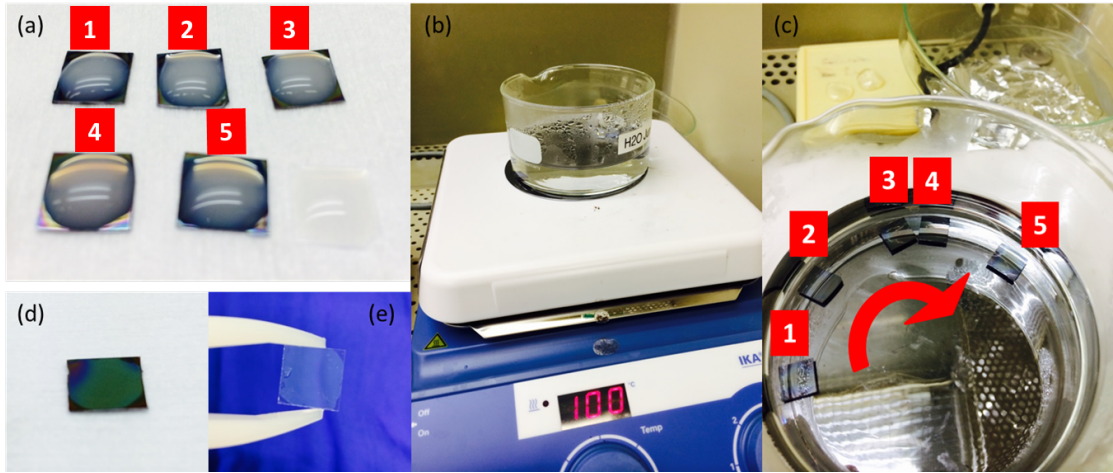


Figure 3.3: PS spheres deposition. (a) The droplets of PS spheres solution on PMMA layer. (b) Hot water bath at 100 °C on a hot plate. (c) Keep the same sample order in the hot water bath. (d) The successfully drop coated PS sphere layer on Si substrate and (e) glass substrate.

fingers, respectively. For many applications glass substrates are required, but due to the transparency of the polymer layer, as well as the glass substrate, it is quite difficult to tell the surface quality after spin coating. Therefore, more practice using Si substrates is necessary for the beginner. We use different PMMA solutions from Allresist company (AR-P 661.04 and AR-P 661.06) and rotation speed of about 4000 rpm to create 230 nm and 480 nm thick polymer layers. Varying the rotation speed enables us to tune the thickness of the PMMA layer within ± 50 nm. After spin coating, the sample is hard baked at 165 °C for 2 minutes to fix the PMMA layer on the substrates.

Deposition of PS spheres For the following deposition of PS spheres on the PMMA layer surface, we treat the sample in an oxygen plasma for about 18 seconds (Diener Pico, 0.5 mbar O₂, power level 50% of 200 W, HF power at 2.45 GHz) to decrease the hydrophobicity of the polymer film. Before drop coating of the PS spheres, which have negative electric surface charges, we should bring first a net positive charge to the polymer layer surface for a better adherence and arrangement. Here we use a water suspended poly(diallyldimethylammonium chloride) (PDDA) solution (Sigma Aldrich, 0.2 %). A droplet of PDDA is dropped onto the PMMA surface (see Figure 3.1b) and the sample is right away rinsed with deionized water and dried with a nitrogen stream. For the mask preparation we use water-suspended PS spheres from Polysciences with diameters of 119 nm or 220 nm for different structure sizes. Typically, for 119 nm (220 nm) PS spheres, a 230 nm (480 nm) thick PMMA layer provides the best results. The purchased PS solution

3 Experimental methods

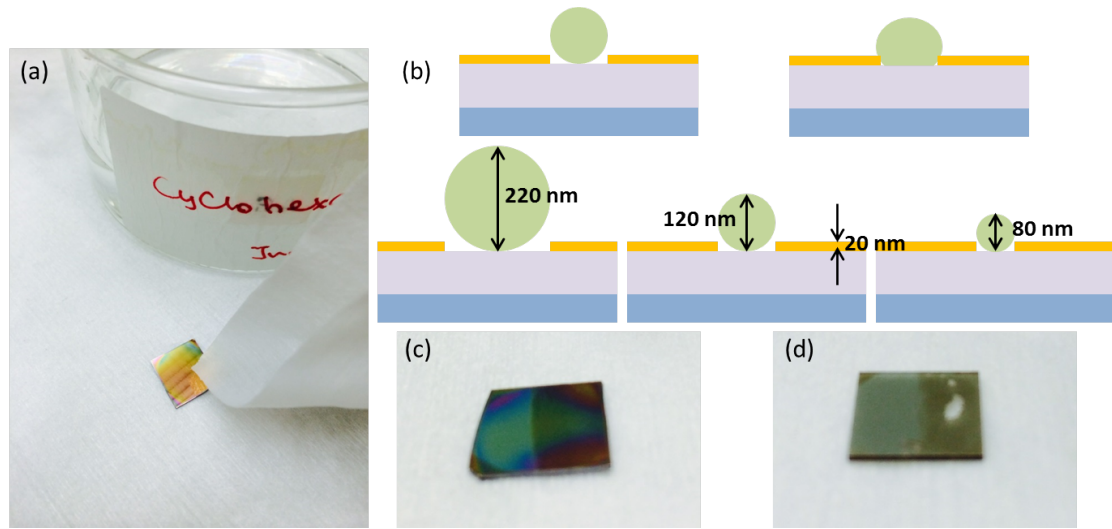


Figure 3.4: (a) Cleaning of the mask surface with tissue and cyclohexane. (b) Schematic deformation process of the PS spheres and the geometries of the masks with different PS sphere sizes. (c) The colour of the clean mask surface (right half side) and the mask still covered with PS spheres (left half side) on Si substrate and (d) glass substrate.

is diluted to 0.01 wt% and then ultrasonicated for about 20 min. Importantly, the water in the ultra sonic bath must be always cold for the PS spheres treatment. By varying the concentration of the PS sphere solution we can adjust the coverage of the later evaporated structures. The details will be discussed in chapter 7. After charging the PMMA layer with the PDDA solution, a droplet of the PS sphere solution (about $100 \mu\text{l}$) is dripped onto the sample (see Figures 3.1c and 3.3a). After 1 minute, it is rinsed away with deionized water and the sample is placed into a hot water bath, at about 100°C , for around 3 minutes to fix the PS spheres on the polymer film, as shown in Figure 3.3b. For mass fabrication one should always keep the same sample order for all processes (Fig. 3.3c), to ensure the same condition of every sample. After drying the sample with nitrogen, the PMMA layer is now covered with well separated and randomly arranged PS spheres. From the surface colour we can directly see the quality of the PS sphere layer. The more homogeneous colour, the better arranged colloidal film, as shown in Figures 3.3d and 3.3e.

Evaporation of Au mask and PS spheres lift-off Subsequently, a thin film consisting of 5 nm chromium (Cr) and 20 nm gold (Au) is evaporated on top of the sample (see Figure 3.1d), to function as an oxygen plasma resistant layer. The PS spheres must be removed directly after the evaporation process in cyclohexane solution in an ultrasonic bath (90 W, 20 minutes). The resulting hole-mask is

3 Experimental methods

shown in Figure 3.1e. The lift-off parameters depend on the diameter as well as the concentration of the PS spheres. For smaller size and higher concentrated PS spheres, the lift-off power can be higher (up to 110 W) and the time also relatively longer (25 - 30 min). As shown in Figure 3.4b, due to the PS spheres deformation during the gold film evaporation, the lift-off process is more difficult for smaller PS spheres, and it is nearly impossible for the PS spheres with diameter smaller than 80 nm. For mass fabrication, change of cyclohexane solution is necessary. For small PS spheres, one can also use a clean room tissue soaked in cyclohexane to clean the sample surface very carefully and without direct finger touching of the sample (see Figure 3.4a). From the surface colour one can tell if the sample is really clean, as shown in Figure 3.4c (Si substrate) and 3.4d (glass substrate), both with right half sides clean. The broken gold film surface in Figure 3.4d resulted from too long lift-off time in ultra sonic bath or too strong tissue cleaning.

Oxygen plasma etching Finally, we treat the sample again with oxygen plasma for an isotropic etching to create extended holes in the PMMA layer underneath the holes of the gold mask, as shown in Figure 3.1f (for 230 nm PMMA: 11.2 min, power level 100% of 200 W, 1.3 mbar O₂). For thicker PMMA (480 nm), the etching time should be extended to 13.5 min. This etching step is very crucial for a successful fabrication and depends strongly on the etching parameters, which may differ for different plasma etching machines. For smaller size of the mask holes, higher mask hole concentration on a sample and multiple samples per treatment, the etching power can be slightly higher (+50 W), or the etching time longer (+0.5 min). A good indication for successful etching is a suitable waviness of the sample afterwards, due to the removed PMMA underneath the mask holes. Additionally, scanning electron microscope (SEM) imaging is helpful to determine whether the PMMA layer has been etched all the way down and still enough PMMA posts remain to support the Au-mask (Figure 3.5). The unetched gold mask is very flat under the SEM (Fig. 3.5a), and after suitable oxygen plasma etching the mask surface shows the suitable waviness (Fig. 3.5b and 3.5c). The etching effect depends also on the hole-density of the mask. From the Figures 3.5d and 3.5e, one can determine if the mask is not enough etched or already too much etched, respectively. Figure 3.5f shows a gold mask with inhomogeneous hole-density, which results to different etching effects using the same parameters. If the lift-off process of the PS spheres is not complete, the plasma etching process is also not reproducible, due to the cover of the PS spheres on the mask holes (see Fig. 3.5g) or even when the PS spheres are removed from the hole but still remain on the mask (see Fig. 3.5h). Otherwise, an optical microscope can be also helpful to determine the etching results, which is more simple and convenient than SEM. Figures 3.6a, b, and c correspond the SEM images in Figures 3.5a, c, and e, respectively. With more experience, one can also distinguish the etching quality of

3 Experimental methods

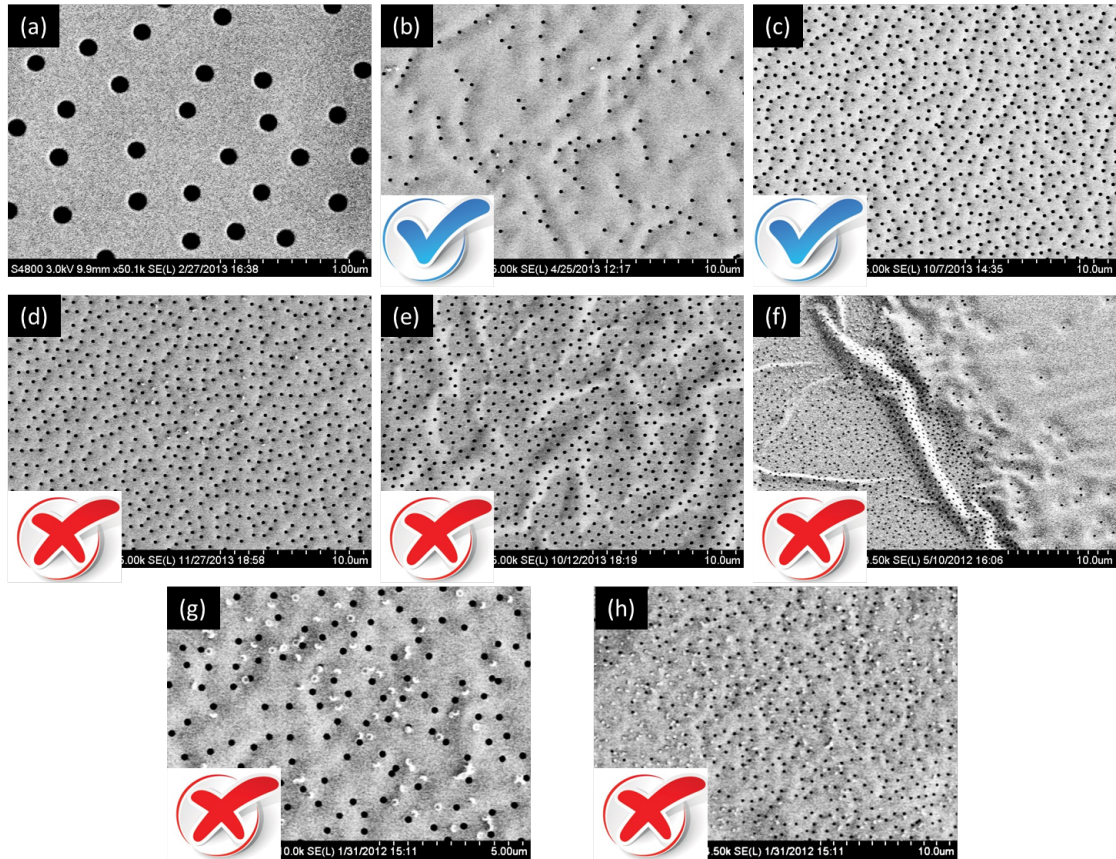


Figure 3.5: SEM imaging of the oxygen plasma etching results. (a) Hole-mask without etching. (b) Low concentrated hole-mask with successful etching. (c) High concentrated hole-mask with successful etching. (d) Not enough etched hole-mask. (e) Hole-mask with too much etching. (f) Etching result using a mask with inhomogeneous hole-distribution. (g) Mask with the PS spheres removed from the holes. (h) Mask with most of the PS spheres still in holes.

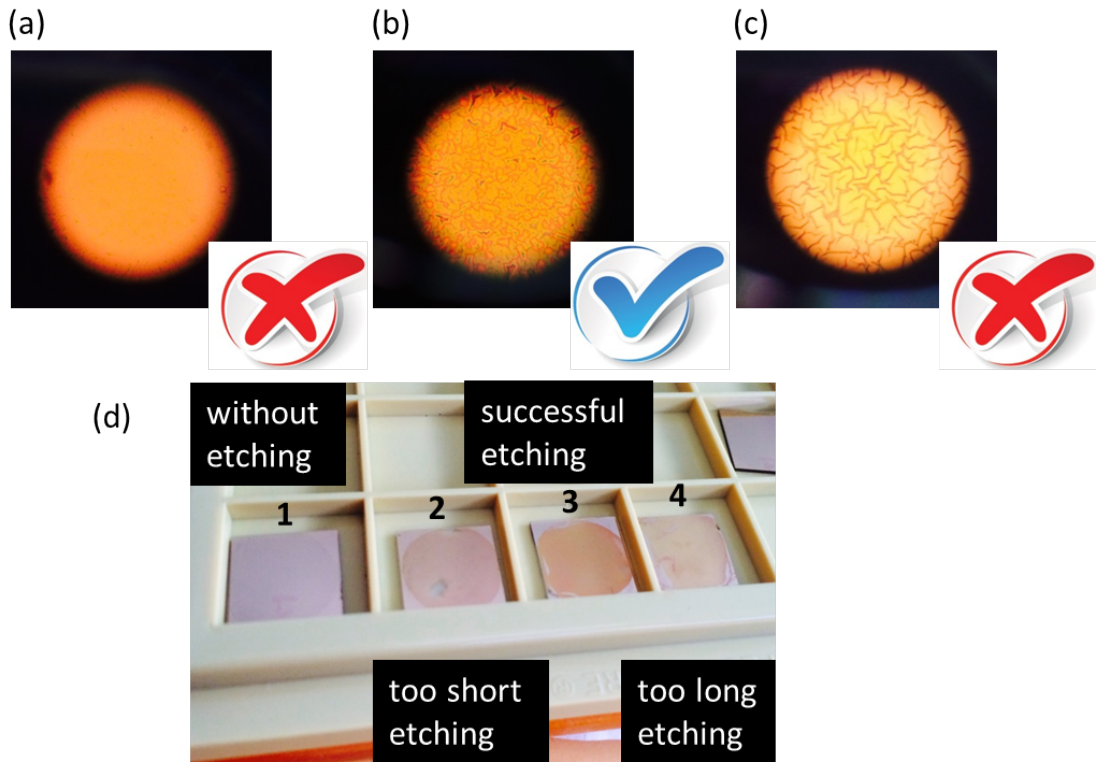


Figure 3.6: Optical microscope imaging of the oxygen plasma etching results. (a) Hole-mask without etching. (b) Hole-mask with successful etching. (c) Hole-mask with too much etching. (d) Determination of the plasma etching results from the gold mask surface colour.

the samples from the surface colour, as shown in Figure 3.6 d. From left to right is the unetched (1), not enough etched (2), successfully etched (3), and too long etched (4) hole-mask on glass substrate. If this step was successful, the samples are ready for the following tilted-angle evaporation.

3.1.2 Nanosphere lithography

Essential for nanolithography, we use a hexagonal close-packed monolayer of PS spheres directly as evaporation mask. In order to fabricate such a mask, we take about 1.5 ml of the 2.6% latex solution with the PS sphere diameter of 470 nm into a 2 ml plastic cuvette and centrifuge it for 30 minutes. After this process all of the latex particles are deposited on the bottom of the cuvette and most of the water is removed from this solution using a pipette. The concentrated latex particle solution (solution A) is placed in an ultrasonic bath with cool water for a

3 Experimental methods



Figure 3.7: The bent glass pipette.

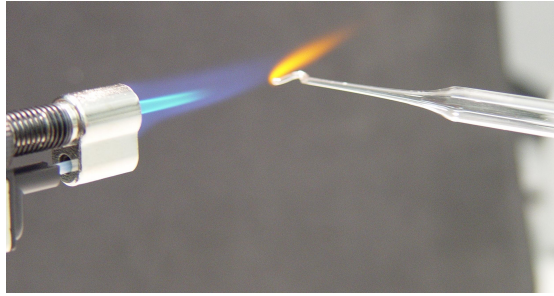


Figure 3.8: Preparation of a small tip of the pipette.

while.

In another plastic cuvette, we mix $100 \mu\text{l}$ ethanol and $6 \mu\text{l}$ 1% hexylamin in ethanol solution together as solution B and place it also in the ultrasonic bath for a while. Here, the hexylamin is used for adjusting the pH value of the solution and neutralizing the surface charge of the PS spheres, so that the PS particles can form a hexagonal close-packed monolayer. In the end, solution A is mixed with solution B and the finally prepared solution is placed in the ultrasonic bath for 20 minutes to mix it thoroughly.

For the preparation of the nanosphere monolayer, a bent glass pipette as shown in Fig. 3.7 is needed. The tip of the pipette must be drawn to very small size, as shown in Fig. 3.8, so that the prepared latex solution flows slowly enough out from it and the nanospheres can be arranged well as a monolayer. The finished pipette must be tested with ethanol. The velocity of the dropping solution is about 1 drop per second. The pipette is then filled with isopropanol and cleaned in the ultrasonic bath for a few minutes. Before using the pipette, it must be absolutely dried with nitrogen.

In addition to the pipette, we need a petri dish with diameter of about 20 cm, which is cleaned with isopropanol and then flushed with distilled water. Afterwards the petri dish is filled with distilled water and placed in a closed plastic box with ethanol atmosphere in it.

After that we draw about $100 \mu\text{l}$ of the finally mixed solution with the bent

3 Experimental methods

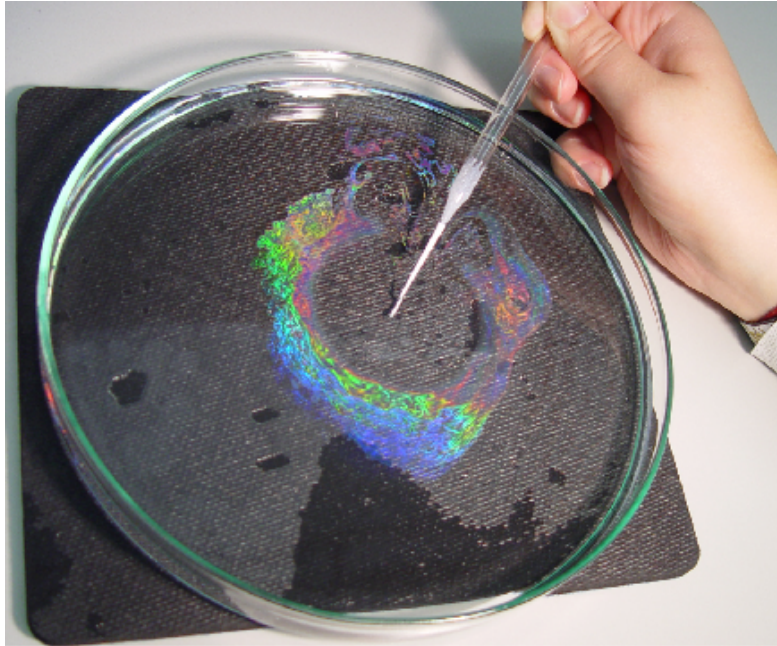


Figure 3.9: Mask preparation.

pipette and put it into the water in the petri dish. Due to the smaller density of ethanol than that of water, the solution flows slowly upwards and it floats on the water surface (see Fig. 3.9). As shown in figure 3.10, the amount of the solution can be distributed to cover almost the whole water surface with a monolayer of nanospheres, which shows clearly diffraction colours.

In the end, several $10\text{ mm} \times 10\text{ mm}$ glass substrates are cleaned with acetone and then isopropanol in the ultrasonic bath. The cleaned substrates should be carefully placed into the water and shifted with a wire to be under the monolayer. Finally the water is slowly pumped out of the petri dish with a siphon tube until the nanosphere monolayer is deposited on the glass substrates. Figure 3.11 shows the SEM image of the prepared hexagonal close-packed nanosphere monolayer on the substrates. After the drying process, the evaporation colloidal mask is annealed on a hot plate at $108\text{ }^\circ\text{C}$ for 60 s. As shown in Figure 3.12, with different annealing times we can control the form and the size of the apertures of the monolayer. This allows to tune the shape of different nanostructures precisely.

3.1.3 Tilted-angle-rotation evaporation

The evaporation process is performed in a high vacuum with a pressure of about 10^{-7} Torr using the evaporator Edwards E306 (Fig. 3.13). As shown in Figure

3 Experimental methods

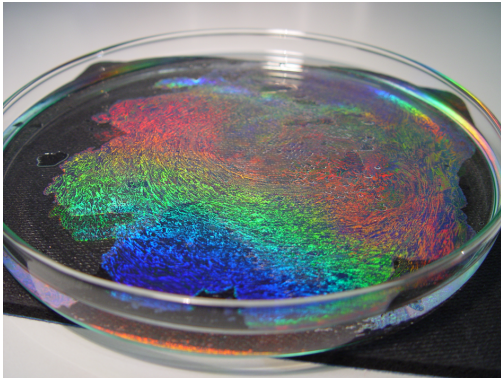


Figure 3.10: PS sphere monolayer on water surface.

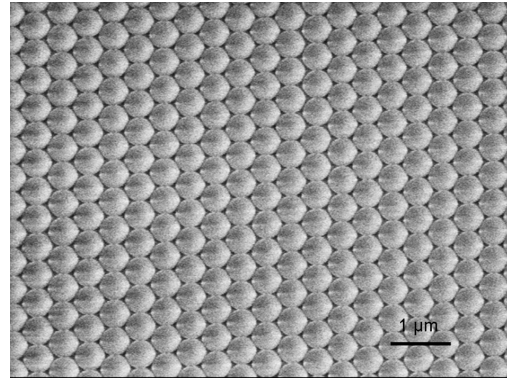


Figure 3.11: SEM image of nanosphere monolayer.

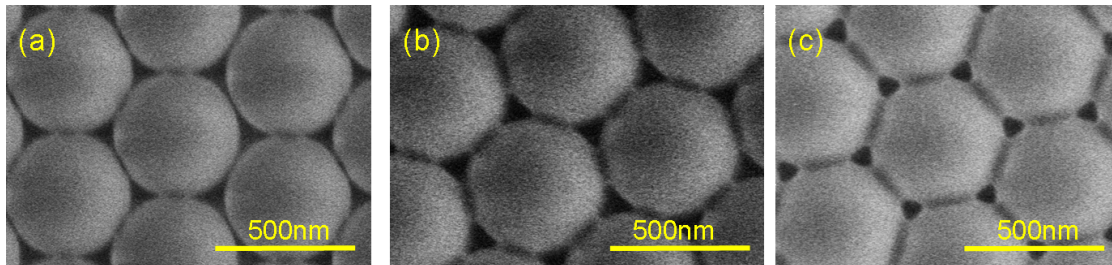


Figure 3.12: Annealing process: (a) Nanosphere monolayer without annealing. (b) Nanosphere monolayer annealed at 108 °C for 60 s. (c) Nanosphere monolayer annealed at 108 °C for 100 s.



Figure 3.13: The evaporator Edwards E306.

3 Experimental methods

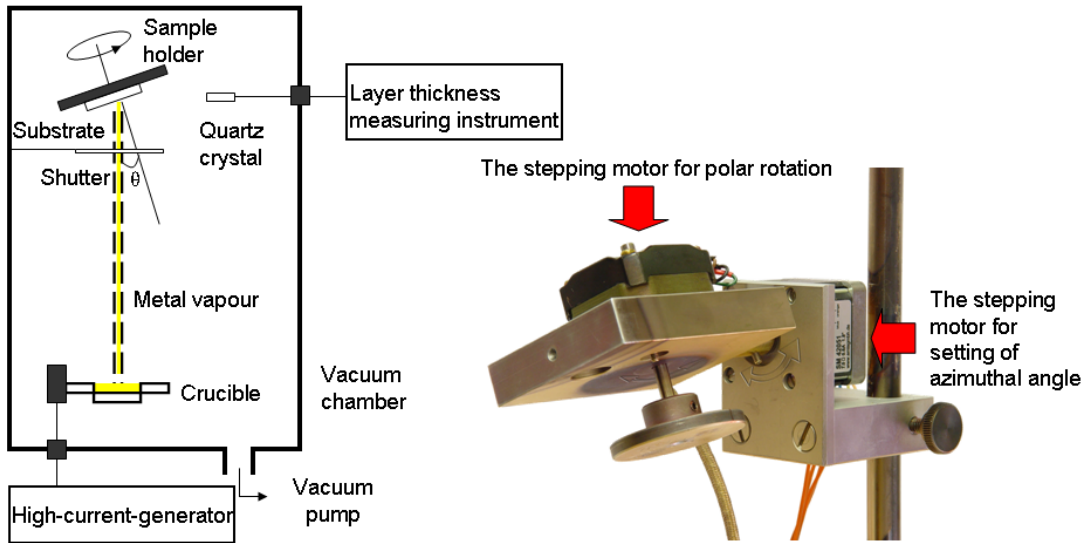


Figure 3.14: The evaporation setup (left) and the stepping motors (right).

3.14 (left), the substrate with evaporation mask is placed on a face-down sample holder tilted by an azimuthal angle θ , which can be changed by a stepping motor, as shown in Fig 3.14 (right). Using another stepping motor the sample holder can be rotated in polar plane. Both of the two motors are controlled by the SMCVieW software, which can accomplish continuous or noncontinuous rotation and set the value of the rotation velocity, as well as the evaporation angle. Material is evaporated from a crucible upwards onto the sample in a distance of about 25 cm. For precise control of the evaporation process, a shutter between crucible and sample is used, which can be opened manually outside the vacuum chamber. When the shutter is closed, we can change the settings of the two stepping motors or different material crucibles, so that some complex structures consisting of different elementary shapes, as well as different materials can be prepared. In order to excite the metal atom to escape from the metal surface, we must give it high enough energy with a high-current-generator, which is connected with the crucible. During the evaporation we use a layer thickness measuring instrument with a quartz crystal, to monitor the evaporation rate. As an adhesive medium a thin layer of chromium (Cr) is evaporated on top of the substrate. Then the main layer of gold or some other metal is evaporated.

During the evaporation process, as shown in Figure 3.15, the metal vapour beam passes through the apertures of the nanosphere monolayer (or the holes of the thin gold mask) and forms different structures on the substrate depending on the evaporation parameters. For example, with a constant evaporation angle θ and continuous rotation of the sample, a ring structure is formed. Otherwise limited

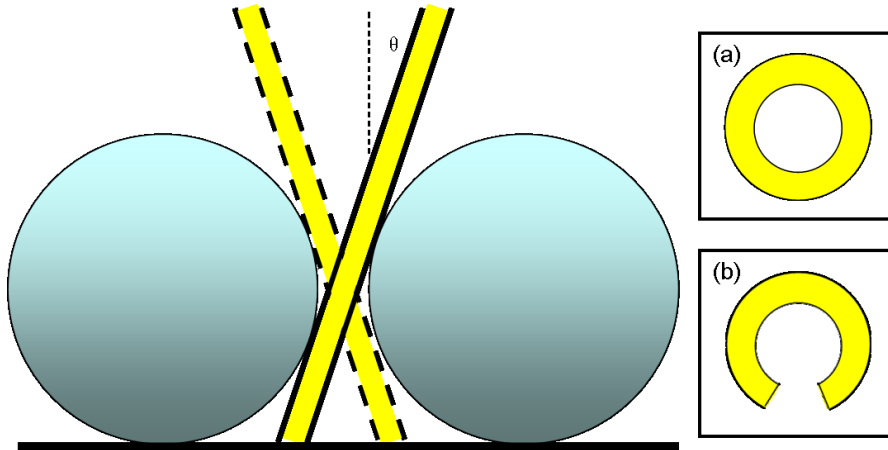


Figure 3.15: Basic geometry of metal evaporation. (a) Ring structure: evaporated with continuous rotation. (b) Split-ring structure: evaporated with limited rotation.

rotation, e.g., from 0° to 300° , results in a split-ring structure.

After the evaporation, the mask is removed with a scotch tape and then the sample with the rest of PS sphere monolayer mask is cleaned in N-Methyl-2-pyrrolidone (NMP) solution in an ultrasonic bath for a few seconds and followed by flushing with isopropanol. For the hole-mask lithography, we only use acetone to wash away the rest of PMMA. Further cleaning for precise measurement is required with oxygen plasma etching (250 W, 1 mbar, 10 to 15 min).

3.2 Optical measurements and numerical simulation techniques

For the optical characterization of the fabricated plasmonic nanostructures we use a commercial Fourier transform infrared (FTIR) spectrometer (Bruker Vertex-80), in which a Michelson-Interferometer is built. The basic set up of the Michelson-Interferometer is shown in Figure 3.16. A monochromatic light beam is divided by a semi-transparent mirror (half-silvered glass plate) into two beams of equal intensities by partial reflection and transmission. During the moving of the right side mirror, if the two paths of light differ by a whole number of wavelengths, there is constructive interference and a strong signal at the detector. By a whole number and a half of wavelengths, there is destructive interference and a weak signal. The resulting signal intensity, which is plotted as a function of the mirror

3 Experimental methods

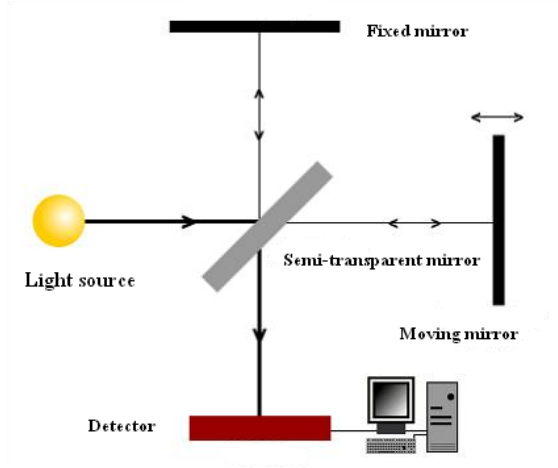


Figure 3.16: The Michelson-Interferometer [66].

position, provides a so-called characteristic interferogram:

$$I(x) = I_0 \cdot \cos^2(4\pi x/\lambda). \quad (3.1)$$

Here I_0 is the maximum intensity, λ is the wavelength and x is the right side mirror position. With a fourier transformation

$$I(\omega) = \frac{1}{\sqrt{2\pi}} \int_{-\infty}^{+\infty} I(x) e^{-i\omega x} dx, \quad (3.2)$$

the signal intensity as a function of the frequency is calculated from the information dependent on the mirror position.

With the FTIR spectrometer, transmission and reflection spectra can be measured for very small areas of the sample, such as $100 \mu\text{m}^2$ up to 5mm^2 . As light source we use a tungsten halogen lamp for the measurements from the visible to the infrared, namely in the wavelength range from 500nm to $5 \mu\text{m}$. With a thallium bromo-iodide polarizer we can obtain linearly polarized light. For different wavelength ranges, we need to use different beam splitters and detectors. From 500nm to $1.2 \mu\text{m}$, a calcium-fluoride (CaF_2) UV-VIS-NIR beam splitter and a silicon diode detector are used. For the wavelength regime from $1 \mu\text{m}$ to $5 \mu\text{m}$, we use a CaF_2 NIR beam splitter and a liquid-nitrogen-cooled mercury cadmium tellurium (MCT) detector. The measured spectra with different detectors can be combined.

In order to calculate the optical properties of the plasmonic nanostructures numerically, we use CST Microwave Studio, which is an all-purpose electromagnetic simulator based on the Finite Integration Technique (FIT). With this method, the

3 *Experimental methods*

Maxwell equations are numerically solved by defining a finite calculation domain, which can be split up into hexahedral, as well as into tetrahedral grids by creating a suitable mesh system. For the simulation we use a Finite-difference time-domain (FDTD) code. FDTD is a computational analysis technique to solve the microwave problems in electrodynamics. It can find approximate solutions to the time-dependent Maxwell's equations in partial differential form. Since it is a time-domain method, FDTD solutions can cover a wide frequency range with a single simulation run, and treat nonlinear material properties in a natural way. For all simulations, we use the permittivity of bulk gold, which is described by Drude model with plasma frequency $\omega_p = 1.37 \times 10^{16}$ Hz and the damping constant $\kappa = 1.2 \times 10^{14}$ Hz.

4 Antenna-assisted SEIRA substrates

This chapter is based on the publication: S. Cataldo, [J. Zhao](#), B. Frank, F. Neubrech, C. Zhang, P. V. Braun, and H. Giessen (The 1st and 2nd authors contributed equally to this work), *Hole-mask colloidal nanolithography for large-area low-cost metamaterials and antenna-enhanced SEIRA substrates*, ACS Nano **6**, 979 (2012).

Infrared spectroscopy is an important analytical tool for chemistry, biology, pharmacy, and medicine. Dipole- and Raman-active modes provide key information about structural and conformational properties of small molecular species as well as larger units, such as proteins or peptides. Unfortunately, the absorption and scattering cross sections of molecules in the infrared are relatively low, which requires large quantities for analysis. One way to overcome this problem is the use of surface enhanced methods, such as surface-enhanced Raman spectroscopy (SERS) and surface-enhanced infrared absorption (SEIRA) spectroscopy. In these cases, the local electric field is strongly enhanced by plasmonic effects at rough metal surfaces and hence the lower detection limit is reduced. Recently, resonantly enhanced SERS and SEIRA methods have been introduced [67–70], as well as the simultaneous SERS and SEIRA enhancement [71, 72] with picomolar sensitivity and a 20000-fold SEIRA enhancement in comparison to common infrared absorption techniques. The SEIRA sensitivity was even further increased to the attomolar level using specifically tailored resonant nanoantennas [4, 5]. In particular, the detection of a monomolecular layer of octadecanethiol (ODT) was demonstrated with a simple Fourier-transform microscope using light from a synchrotron. Metamaterial geometries are utilized for SEIRA [73–76], however on small-area samples fabricated by e-beam lithography. In order to bring these advances into biology and chemistry laboratories and allow for a plethora of applications, large-area low-cost fabrication is required. In this chapter we present an elegant solution to this problem by introducing a low-cost simple fabrication method for resonant nanoantenna SEIRA substrates with $\sim \text{cm}^2$ of defect-free areas, which allow for easy adjustment to the desired vibrational frequencies. We manufacture metallic split-ring-resonator (SRR) metamaterial nanoantennas using hole-mask colloidal nanolithography followed by tilted-angle

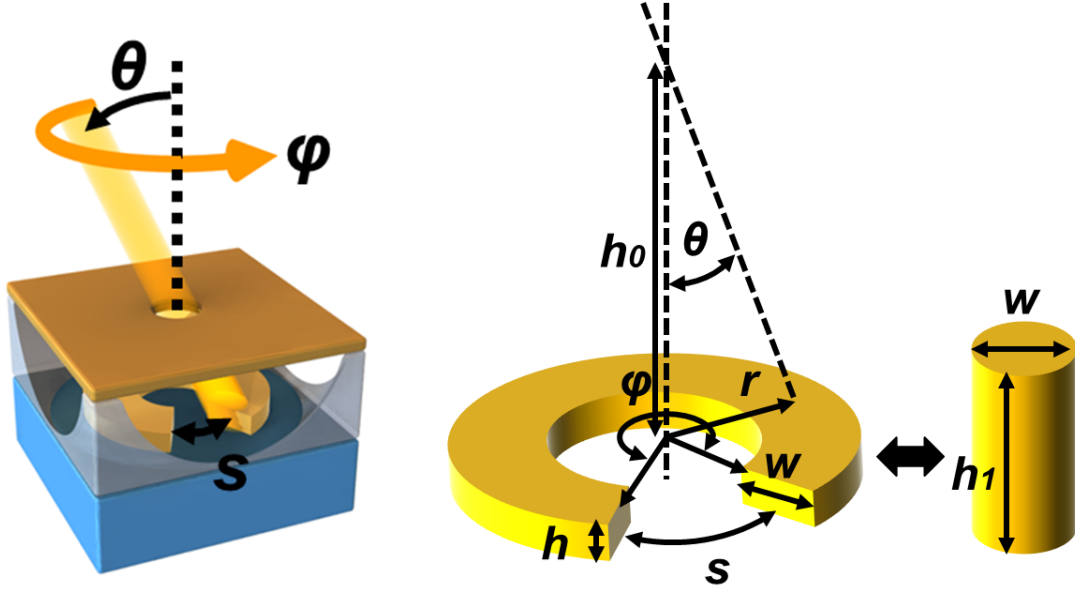


Figure 4.1: Schematic diagram for SRR evaporation and the derivation of the structure parameters.

metal evaporation. We produced several samples with different SRR geometries and hence a set of different resonance frequencies to demonstrate easy adjustability. SEIRA sensing down to the monolayer sensitivity was observed both for normal as well as deuterated (d-) ODT. At the same time, our manufacturing method represents an elegant way to produce large-area and low-cost SRR metamaterials with resonances in the near- and mid-infrared spectral range.

4.1 Fabrication of SRR antenna

A gold hole-mask on a 1 cm^2 silicon substrate, as introduced in chapter 3.1.1, is utilized for the fabrication of the SRR metamaterials, which serves as resonant nanoantenna SEIRA substrate. As shown in Figure 4.1, we evaporate first about 1 nm chromium as adhesion layer, and subsequently about 80 nm gold, using an azimuthal angle θ and a polar angle φ , which are controlled with two stepping motors. Combined with the PMMA thickness h_0 , we can determine the middle radius r and the gap size s of the ring:

$$r = h_0 \tan \theta, \quad (4.1)$$

$$s = 2\pi r \frac{360^\circ - \varphi}{360^\circ} = 2\pi h_0 \tan \theta \frac{360^\circ - \varphi}{360^\circ}. \quad (4.2)$$

4 Antenna-assisted SEIRA substrates

The width of the SRR w is determined by the mask-hole diameter, namely, the diameter of the used nanospheres (here 119 nm), as well as the tilted angle θ . The size of the structure, which is tilted evaporated, is slightly smaller than the PS spheres diameter. The evaporated gold thickness 80 nm is measured directly with the layer thickness monitor, which indicates the thickness of the evaporated metal layer without mask h_1 . In order to calculate the real structure thickness h , we use a geometrical model, as shown in Figure 4.1 right, which is a disk structure with diameter w and thickness h_1 using perpendicular evaporation. On the assumption that we evaporate the same material for the two structures, the volume of them should be the same:

$$V_{SRR} = V_{Disk}, \quad (4.3)$$

$$\left(\pi r_{out}^2 \cdot \frac{\varphi}{360^\circ} - \pi r_{in}^2 \cdot \frac{\varphi}{360^\circ}\right) \cdot h = \pi \left(\frac{w}{2}\right)^2 \cdot h_1. \quad (4.4)$$

Here r_{out} and r_{in} is the outer and inner radius of the ring structure, respectively, with

$$r_{out} - r_{in} = w, \quad (4.5)$$

$$\frac{r_{out} + r_{in}}{2} = r. \quad (4.6)$$

From the equation 4.1, 4.4, 4.5, and 4.6, we have

$$h = h_1 \frac{45^\circ w}{\varphi h_0 \tan \theta}. \quad (4.7)$$

The successful preparation of the metamaterial SRR nanoantennas is shown in Figure 4.2. The SEM images of large area (Figures 4.2a, c) demonstrate the low defect concentration of our method. Larger magnification (Figures 4.2b, d) shows the two different SRR geometry details, the low inhomogeneous broadening, as well as the sufficient spacing between neighboring elements. Both samples are fabricated using the mask prepared with 119 nm nanospheres, the PMMA layer with h_0 about 230 nm, and $\theta = 22.5^\circ$. For sample in Fig. 4.2b, the rotation angle φ during the evaporation is 180° , and for the sample in Fig. 4.2d 288° . Figure 4.2e shows an atomic force microscopy (AFM) image of the sample in Fig. 4.2b, and Figure 4.2f shows a height profile along a cross-section with the maximum structure height of about 23 nm.

Using this fabrication method, we can prepare nanostructures over even larger areas. The size of the sample is only limited by the fabricated homogeneous PMMA area using spin coating. The resolution depends only on the size of the used nanospheres and can easily go down to 50 nm metal linewidth and gap widths below 10 nm. The repeatability and reliability is extremely high, as inhomogeneous broadening factors are rather limited during our fabrication process.

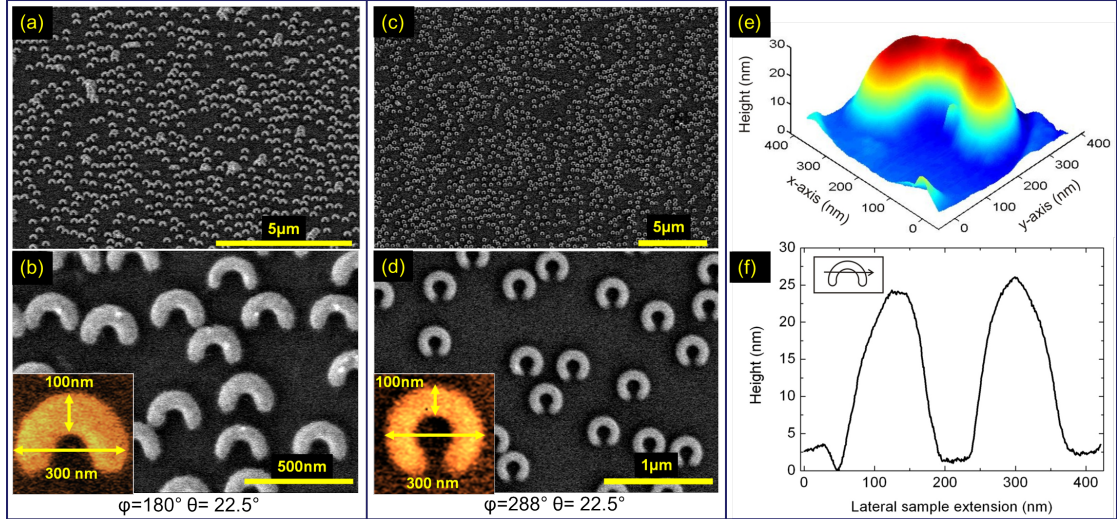


Figure 4.2: SEM images and AFM measurement of split-ring-resonators produced by hole-mask colloidal-lithography. (a), (c) SEM overview showing homogeneous, random coverage over large areas for two types of split-ring resonators. (b), (d) Split-ring resonators with 300 nm diameter and 100 nm ring width. The used azimuthal angle θ is 22.5° , and the polar angle range φ is $0^\circ - 180^\circ$ (b) and $0^\circ - 288^\circ$ (d), respectively. The split-rings are mostly well separated from each other. (e) Three dimensional AFM image of a single split-ring-resonator in (b). (f) Height profile of the measured split-ring-resonator along the cross-section line shown in the upper left corner. The top height is about 23 nm.

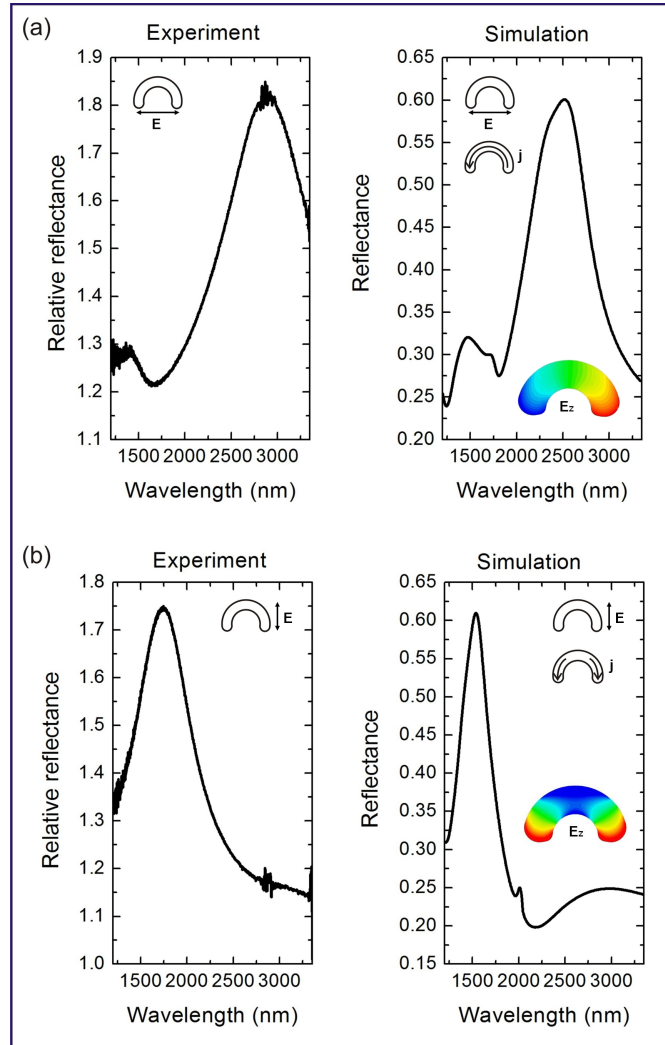


Figure 4.3: Experimental (FTIR) and numerically simulated (FDTD) reflectance spectra of the $\varphi = 180^\circ$ split-ring-resonators. The experimental spectra are normalized with respect to the bare Si substrate. We plot relative reflectance on the y-axis which is larger than one as the background reflectance of silicon is only about 25% and the reflectance of the gold structures on the substrate is significantly higher. The left column shows the experimental results for the incident electric field linearly polarized parallel to the gap (a) and orthogonal to the gap (b). The right column shows the simulated spectra for both polarizations and the current flow j (cartoon) as well as the color coded (red= positive value, blue=negative value, same scale for both plots) electric field E_z (component perpendicular to structure) at the respective resonances.

In order to obtain the required field enhancement for SEIRA, we match the wavelength of the fundamental plasmon mode of the split-ring-resonators with the vibrational resonance of the molecule of interest. We simulate the required geometry parameters using an FDTD code. The refractive index of silicon is assumed to be $n = 3.45$. The gap size, the inner and outer diameter, and the structure height are varied in order to adjust the desired resonance wavelength. The split-ring geometry allows for particularly easy tuning of the resonance wavelength by simply varying the gap opening angle. In comparison to linear antennas the resonance frequency of split-ring-resonators can be tuned without changing the area per split-ring-resonator. Optical characterization of the manufactured structures was carried out using FTIR spectrometer attached with an IR microscope. Optical spectra were obtained using an MCT-detector for normally incident light polarization along and perpendicular to the SRR gap in reflectance geometry. The bare silicon substrate serves as reference. We plot relative reflectance on the y-axis, which is larger than one as the background reflectance of silicon is only about 25%, and the reflectance of the gold structures on the substrate is significantly higher. Figure 4.3a compares experimental results with FDTD simulations for polarization along the gap, and Figure 4.3b for polarization perpendicular to the gap, which show good agreement. Different spectral linewidths arise probably from residual inhomogeneous broadening due to surface roughness, deviations of the gold dielectric function, and interaction of neighboring split-rings. The fundamental (Figure 4.3a) and second-order plasmon resonance (Figure 4.3b) are clearly identified.

4.2 Detection of ODT monolayer

To demonstrate the SEIRA activity, we covered the SRRs with one monolayer of ODT ($\text{SH}(\text{CH}_2)_{17}\text{CH}_3$) and d-ODT ($\text{SD}(\text{CD}_2)_{17}\text{CD}_3$), respectively. After cleaning the SSRs with O_2 plasma (30 s, 1 Torr, 250 W) in order to remove organic residuals, we immersed the gold SRR supported by a Si Wafer in a 100 μmolar solution of ODT (Sigma Aldrich) in ethanol for eight hours. SRR prepared on a different Si wafer covered with d-ODT (provided by the Physical Chemical Institute, University Heidelberg) were immersed in a 20 μmolar solution of d-ODT in ethanol for 24 h. During this time, a selective adsorption of ODT (d-ODT, respectively) on gold SRRs took place. Afterwards, the samples were rinsed with ethanol and dried using nitrogen flow to remove non-specifically bound ODT (d-ODT) molecules. As a result, samples with well defined surface coverage (no molecules on Si, one monolayer on gold SRRs) are obtained, which is the precondition for a quantitative analysis of the SEIRA signals.

We choose ODT as probe molecule, since its absorption characteristics on gold

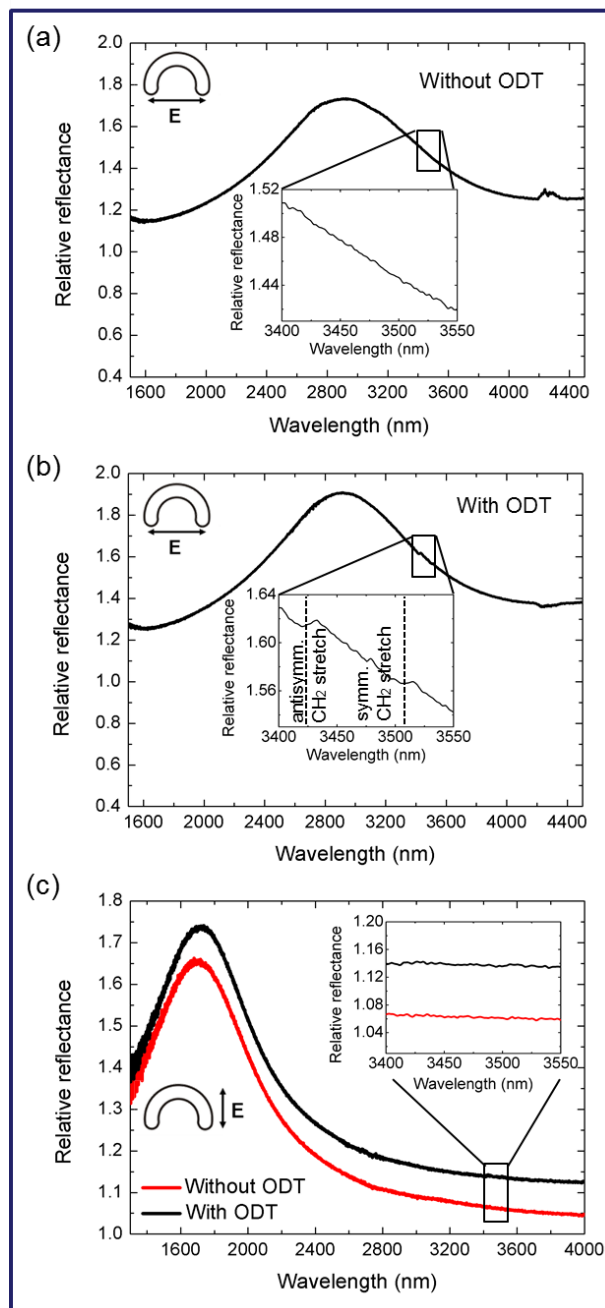


Figure 4.4: Utilization of split-ring resonators from Figures 4.2a and b as SEIRA substrate. We show relative reflectance spectra with bare Si reflectance as reference. (a) Without monolayer of ODT. Only the fundamental plasmon mode is visible for excitation along the gap. (b) With monolayer of ODT and light polarized along the gap, at 2924 cm^{-1} (3420 nm) and 2849 cm^{-1} (3510 nm), the antisymmetric and symmetric CH_2 -stretch modes of ODT are visible as modulation of the reflectance spectra. (c) With light polarized perpendicular to the gap, the higher order plasmon mode at 1670 nm is excited. Hence, no SEIRA enhancement of the ODT vibrational modes around $3400\text{--}3550\text{ nm}$ is visible.

is known from the preparation of self-assembled monolayers [77] and was recently applied to cover nanoantennas for SEIRA [4]. Due to the specific binding of sulfur to gold, multilayer adsorption as well as adsorption on surfaces other than gold is inhibited. Furthermore, ODT features strong IR vibrational bands mainly provided by its CH₂ groups, which are well suited for our SEIRA experiments with vibrational modes at 2855 cm⁻¹ ($\lambda = 3500$ nm) and 2927 cm⁻¹ ($\lambda = 3420$ nm). Inconveniently, CH₂ groups are also present in organic residues, which for example may originate from the PMMA used during the fabrication process. To exclude such an unwanted contribution to the enhanced ODT signals and to demonstrate the easy adjustability of the SRRs in SEIRA, we also carried out experiments with d-ODT with vibrational modes at 2089 cm⁻¹ ($\lambda = 4790$ nm) and 2195 cm⁻¹ ($\lambda = 4560$ nm) [78].

Reflection spectra of SRRs with a polar evaporation angle of 180° before and after deposition of ODT are shown in Figure 4.4a and 4.4b, for IR radiation polarized parallel to the gap. In addition to the fundamental SRR resonance, CH₂ vibrations at 2855 cm⁻¹ ($\lambda = 3500$ nm) and 2929 cm⁻¹ ($\lambda = 3410$ nm) (see inset) are observed after deposition of ODT. Since no CH₂ vibrations are visible in the spectrum before ODT adsorption, we conclude that the appearance of the molecular vibrations originates from the resonantly enhanced near fields of the SRR excitation. This result also shows that no organic residues containing CH₂ are remaining on the SRRs and therefore proves the success of O₂ cleaning. Measurements in perpendicular polarization show no enhanced signals after ODT deposition (Figure 4.4c), which proves that our ODT concentration is below the detection limit of standard IR spectroscopy. The signals are only resonantly enhanced if ω_{ODT} roughly matches the far field resonance frequency ω_{res} . As known from theoretical studies [79, 80], the maximum near-field enhancement is expected at values slightly larger than $\omega_{ODT}/\omega_{res} = 1$. Thus, the observed ODT signal can be further maximized by optimizing the SRR resonance with respect to the vibrational bands.

4.3 Detection of d-ODT monolayer

A better match is achieved for SRRs with a polar evaporation angle $\varphi = 288^\circ$ covered with d-ODT, as shown in Figure 4.5. We define the polarization along the gap as 0°. Figure 4.5a shows the reflectance spectra of the SRRs before the deposition of d-ODT for different polarizations. Choosing incident light polarization from 0 to 90°, one can select different metamaterial antenna resonance positions. In particular, a polarization of 45° exhibits three resonances throughout the near IR range. Therefore, our material is perfectly suitable for multi-line resonantly enhanced SEIRA, as recently proposed [8, 10]. Modifying the SRR

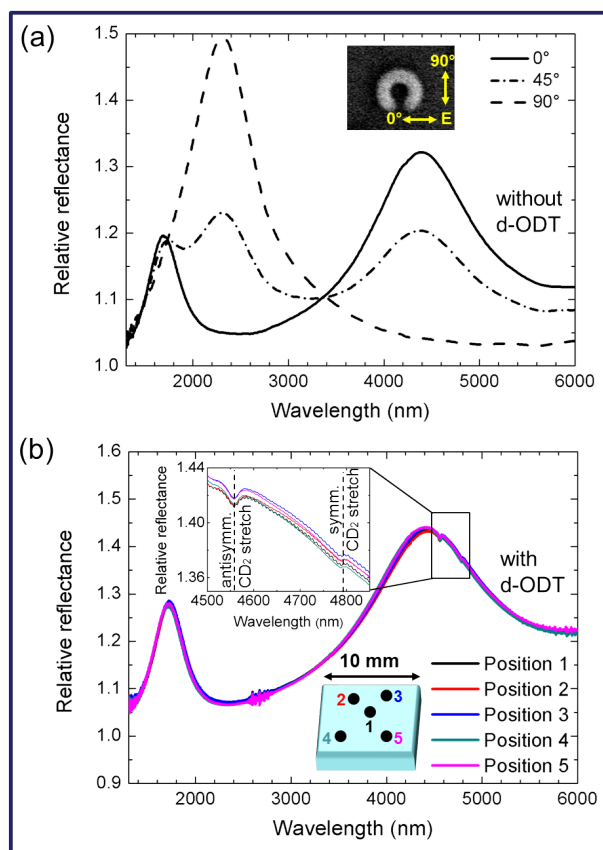


Figure 4.5: Utilization of split-ring-resonators from Figure 2c and 2d as SEIRA substrate. We used the SRR fundamental plasmon mode around $4.4 \mu\text{m}$. (a) Spectra of structures before d-ODT deposition with linearly polarized light at angles 0° , 45° , and 90° with respect to the gap, which is illustrated in the inset. Different split-ring resonances at around 1700 nm, 2400 nm, and 4400 nm can be excited. (b) Spectra of the structures after d-ODT deposition using linearly polarized light parallel to the gap. The different spectra are measured at different positions of the sample, which is illustrated in the cartoon in the lower right corner. All the spectra show the same plasmon excitation and the same d-ODT signal. This is a further proof for the homogeneity of the sample. The spectra in the upper left corner show the two strongest modes of d-ODT: antisymmetric CD_2 -stretch at 2193 cm^{-1} (4559 nm) and symmetric CD_2 -stretch at 2086 cm^{-1} (4793 nm).

geometry to an elliptical shape, with suitably adjusted evaporation angles, would give us even the freedom to independently tune the parallel versus the perpendicular resonances with respect to the gap. Figure 4.5b shows the reflectance spectra after the deposition of d-ODT for the polarization 0° . Here, the symmetric CD_2 vibration is at 2089 cm^{-1} ($\lambda = 4790\text{ nm}$), and the antisymmetric CD_2 vibration at 2195 cm^{-1} ($\lambda = 4560\text{ nm}$) nearly coincides with the fundamental SRR resonance. To verify the homogeneous distribution of SRRs and the low defect concentration on our sample, we carried out laterally resolved IR spectroscopy measurements in addition to the aforementioned SEM analysis. A circular aperture, with diameter of about $100\text{ }\mu\text{m}$, allows us to record relative reflectance spectra at different sample positions with separation distances in the mm range. As depicted in Figure 4.5b, the plasmonic response of the SRRs as well as the enhanced d-ODT signal is nearly identical for different positions on the sample. This fact confirms the extremely homogeneous large-area fabrication of SRR antennas using hole-mask colloidal nanolithography.

To perform a quantitative analysis, we compared the enhanced signal strength to the estimated reflectance of a monolayer ODT (d-ODT) signal on a bare silicon wafer. Since the ODT (d-ODT) signal in such a configuration is below the noise level, we estimated a signal from infrared reflection absorption spectroscopy (IRRAS) of one monolayer ODT (d-ODT) on a gold wafer. Using Fresnel equations for a three-layer system, as present in previous IRRAS studies [81], we obtained signal strengths of about 0.0039% (antisymmetric CH_2) and 0.0016% (symmetric CH_2) for one monolayer ODT on silicon. For d-ODT, we obtain 0.0026% (antisymmetric CD_2) and 0.002% (symmetric CD_2). To estimate enhancement factors, we need to consider the relative fractions of the illuminated spot area effectively covered with molecules. While in IRRAS measurements the whole gold film is covered by ODT, only a small part of the illumination spot in SEIRA measurements is covered by molecules due to the selective adsorption on the gold SRRs. Further, due to the distribution of the electromagnetic near-field around the SRRs, the enhanced molecular signal mainly originates from the ends of the SRRs. Considering both effects, we estimate enhancement factors in our case up to 8000 for ODT covered SRRs and up to 20000 for d-ODT covered SRRs.

Compared to SEIRA measurements using linear antennas [4, 82], lower enhancement factors using our SRRs are observed, which may be due to different crystalline quality as a result of different fabrication processes. Additionally, the surface roughness is expected to affect the SEIRA signal enhancement. This does not mean that a perfectly smooth surface yields the highest enhancement as for example known from SERS measurements. Also carbon deposited during SEM imaging, which is only partially removed by O_2 ashing, may suppress ODT (d-ODT) adsorption. Also, a major factor for lower SEIRA enhancement is the high

4 Antenna-assisted SEIRA substrates

refractive index of the silicon substrate. This effect can be understood in analogy to propagating surface plasmons at metal-dielectric interfaces, where a larger portion of the electric field is squeezed into the metal for materials with higher dielectric constants [83]. This effect reduces the field that can interact with the ODT on top. CaF_2 substrates will allow for enhancement factors as large as 500000 [5].

5 Asymmetric double SRRs for Fano resonant sensing

This chapter is based on the publication: [J. Zhao](#), C. Zhang, P. V. Braun, and H. Giessen, *Large-area low-cost plasmonic nanostructures in the near infrared region for Fano resonant sensing*, *Adv. Mater.* **24**, 247 (2012).

Complex metallic nanostructures are able to support bright as well as dark optical modes [84]. When designed, with the appropriate geometry and symmetry, metallic nanostructures have the potential to exhibit narrow Fano resonances due to destructive interference of the different modes [62, 85–88]. These Fano resonances can provide enhanced sensitivity and figure of merit (FOM) of localized plasmon sensors [9, 89], which easily reach, or even exceed, the best known LSPR sensors in single plasmonic particles [90–92]. This is due to the fact that the complex geometry and the many degrees of design freedom allow for tailoring the resonant near-fields in a very small volume. Additionally, the spectrally narrow Fano resonances provide steep spectral features, which shift strongly upon refractive index change of the surrounding material, and hence, the local field. Therefore, measuring transmission and reflection intensity gives a strong response upon change of the environment.

One suitable geometry to generate sharp resonances is the asymmetric double split-ring resonator (ADSRR), where two crescent shaped nanoparticles with different lengths are placed facing each other. In this structure, two gaps are present, and these are placed at angles other than 180° [7, 93]. Examples for sensors based on such ADSRRs include biosensors in the GHz and THz region [94], as well as sensors in the mid-infrared [8, 76]. However, the large scale application of Fano sensors has been hampered by two issues: one is the ability to utilize low-cost visible or near-infrared lasers as light sources, and the other are pathways to mass-fabricate Fano sensors over cm^2 areas at low cost.

In this chapter, we demonstrate how to overcome these two major obstacles, which would pave the road towards wide utilization of this cutting-edge technique. To the best of our knowledge, this work represents the first large-area low-cost plasmonic Fano sensing LSPR structure. We fabricate gold ADSRRs by hole-mask colloidal nanolithography and vary the degree of asymmetry to study the evolution of the Fano resonance. Thermal annealing [95] is utilized to improve

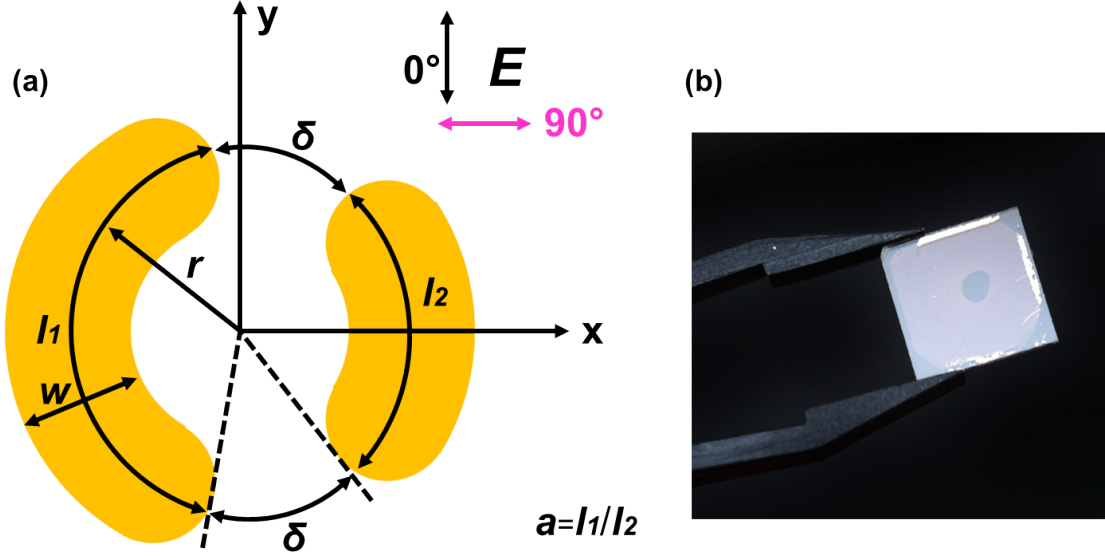


Figure 5.1: (a) Schematic diagram of planar asymmetric double split-ring resonators, with gap size δ , width of the ring w , radius of the ring r , and arc lengths l_1 and l_2 . The degree of asymmetry is defined as $a = l_1/l_2$. All measurements are taken with normally incident light with different polarizations with 0° polarization parallel to the y-axis. (b) Photograph of one of the samples, size 1 cm^2 . The sample is fully covered with asymmetric double split-ring resonators, except for a little hole near the center.

the modulation depth of the Fano resonance or to turn off the coupling. In particular, we carry out time-dependent in-situ studies of the plasmonic spectra during heating. Refractive index sensing with different liquids on our low-cost substrate around the Fano resonance in the near infrared is demonstrated.

5.1 Optical properties of asymmetric double SRRs

Figure 5.1a shows the schematic diagram of the fabricated ADSRRs with gap angle δ , width of the ring w , radius of the ring r , and arc angles l_1 and l_2 . We use a constant r in the experiment, and the gap size δ , as well as the arc lengths l_1 , l_2 are given as angles for easy reproducibility. Both arcs are aligned along the y-axis. The degree of asymmetry is defined as $a = l_1/l_2$. Normally incident light with different polarizations, with the y-axis defined as 0° is used in all measurements. Figure

5 Asymmetric double SRRs for Fano resonant sensing

5.1b is a photograph of one of our 1 cm² samples, which is covered completely and homogeneously with the plasmonic nanostructures, except for the small area near the center, which was caused due to a problem with our spin coater, but can be used as a reference position for the measurement.

ADSRRs with different geometrical parameters and their optical properties are shown in Figure 5.2. SEM images of large-area ADSRR samples A to D (Figure 5.2a) demonstrate the low defect concentration. Higher magnification micrographs (Figure 5.2a inset) show the geometric details of the ADSRR, the low size and shape variation, as well as the sufficient spacing between neighboring elements (i.e., no dominant near-field interaction in the few 10 nm range). The cobweb-like structures and the nanoparticle in the center of the ADSRRs in the insets arise from residual PMMA that was not removed by oxygen plasma etching and the subsequent lift-off process. This residual PMMA does not affect the optical properties of the structures very much, except for a small red shift due to its refractive index. It can be removed by additional oxygen plasma cleaning, as shown in Figure 5.3. The gap size δ is 30° (~ 45 nm), while l_1 is increased and l_2 is decreased from sample A to D. Therefore, the asymmetry parameter a also increases. The same way as the split-rings in chapter 4, the width of the double rings w depends on the hole-size of the mask, and is slightly smaller due to the tilted evaporation angle θ . For all samples, we use the same hole-mask, which is prepared using PS spheres with diameter of 119 nm, and a constant θ (22.5°). The radius of the double rings is also given by

$$r = h_0 \tan \theta, \quad (5.1)$$

where h_0 is the PMMA thickness, which is about 230 nm in this experiment. The gap angle δ is determined by:

$$\delta = (360^\circ - l_1 - l_2)/2. \quad (5.2)$$

The obtained structure heights h_1 and h_2 are calculated using the same geometrical model in chapter 4:

$$h_{1,2} = h \cdot \frac{45^\circ \cdot w}{l_{1,2} \cdot h_0 \cdot \tan \theta}. \quad (5.3)$$

Here h is the total evaporated gold thickness, which is displayed on the layer thickness monitor.

Optical characterization of structures was carried out using a FTIR spectrometer with normally incident light with polarization 0° (black), 45° (blue), and 90° (pink), with 0° parallel to the arcs. The required geometry parameters are simulated using a FDTD code, as shown in Figure 5.2c. The refractive index of glass is assumed to be 1.5. The used SRR structure in simulation is rectangular, with semicircular shapes on the two ends. The simulation agrees very well with our experiments.

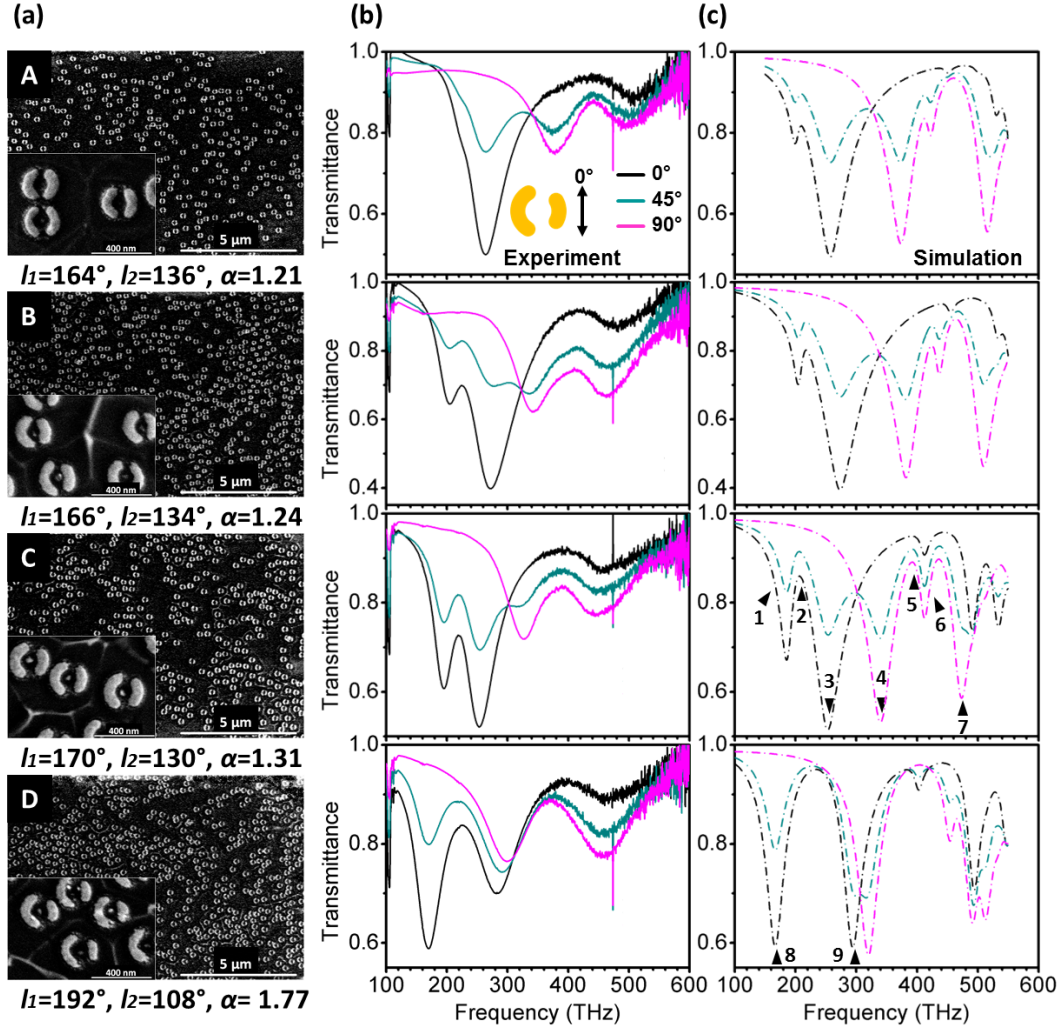


Figure 5.2: (a) SEM images of samples A, B, C and D with constant gap size $\delta = 30^\circ$ (~ 45 nm) and varying arc lengths l_1 and l_2 . The asymmetry parameter α increases from A to D. The gold thickness of all samples is about 15 nm. The cobweb-like structures and the nanoparticle in the center of the asymmetric double split-ring resonators in the insets of the images arise from residual PMMA that was not removed by oxygen plasma etching and the subsequent lift-off process. (b) Transmittance spectra of samples A-D, measured after 15 min annealing at 150 $^\circ\text{C}$ using normally incident light with different polarization. 0 $^\circ$ polarization is parallel to the arcs. (c) Numerically simulated (FDTD) transmittance spectra. The field distribution of the numbered plasmon resonances is shown in Figure 5.4.

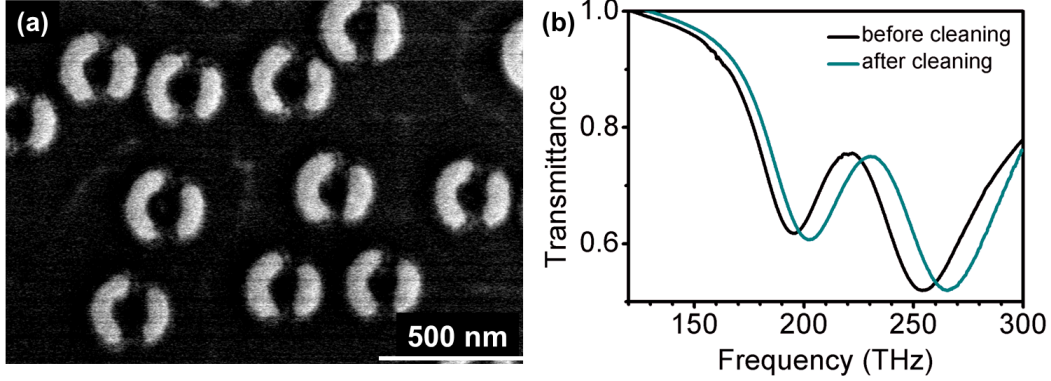


Figure 5.3: (a) SEM images of sample C after 10 min oxygen plasma cleaning. (b) The transmittance spectra of sample C at polarization angle 0° before and after cleaning.

For 0° polarization, we observe an asymmetric Fano resonance at around 220 THz, due to the coupling of a subradiant dark mode with a superradiant bright mode. This coupling becomes stronger with increasing asymmetry parameter a . In the spectrum of sample C, the Fano resonance becomes very sharp and deep. As the asymmetry parameter increases more, the subradiant hybridized mode changes from dark to bright. In sample D, the Fano resonance disappears, and only hybridization and dipole-dipole coupling is observable. For 90° polarization, we observe a weak Fano resonance at around 410 THz in simulation, which also becomes stronger with increasing a , and disappears for too high degree of asymmetry a in sample D. Due to the weak signal near to the limit of near infrared range of the light source in FTIR spectrometer, this Fano resonance for 90° polarization is not visible in experimental results. We only observe an asymmetric broadening of the resonance at around 400 THz in the spectra for 90° polarization of sample B and C. For 45° polarization, all plasmon modes for 0° and 90° polarization are excited simultaneously. To confirm these assessments, we calculate the electric field distribution for all the numbered spectral positions and respective polarizations of Figure 5.2.

Figure 5.4 displays these electric field distributions for the samples C and D. Image 1 and 3 show a superradiant hybridized dipole mode (depicted by black arrows) in sample C at 0° polarization. The two parts of the SRR oscillate in phase. Image 2 shows a subradiant hybridized dark mode, which is located at the Fano peak. Dark means here that the antisymmetric mode distribution does not couple well to the incident light field. The two SRRs oscillate out of phase. Image 4 and 6 shows the superradiant coupled 2^{nd} -order SRR modes of sample C at 90°

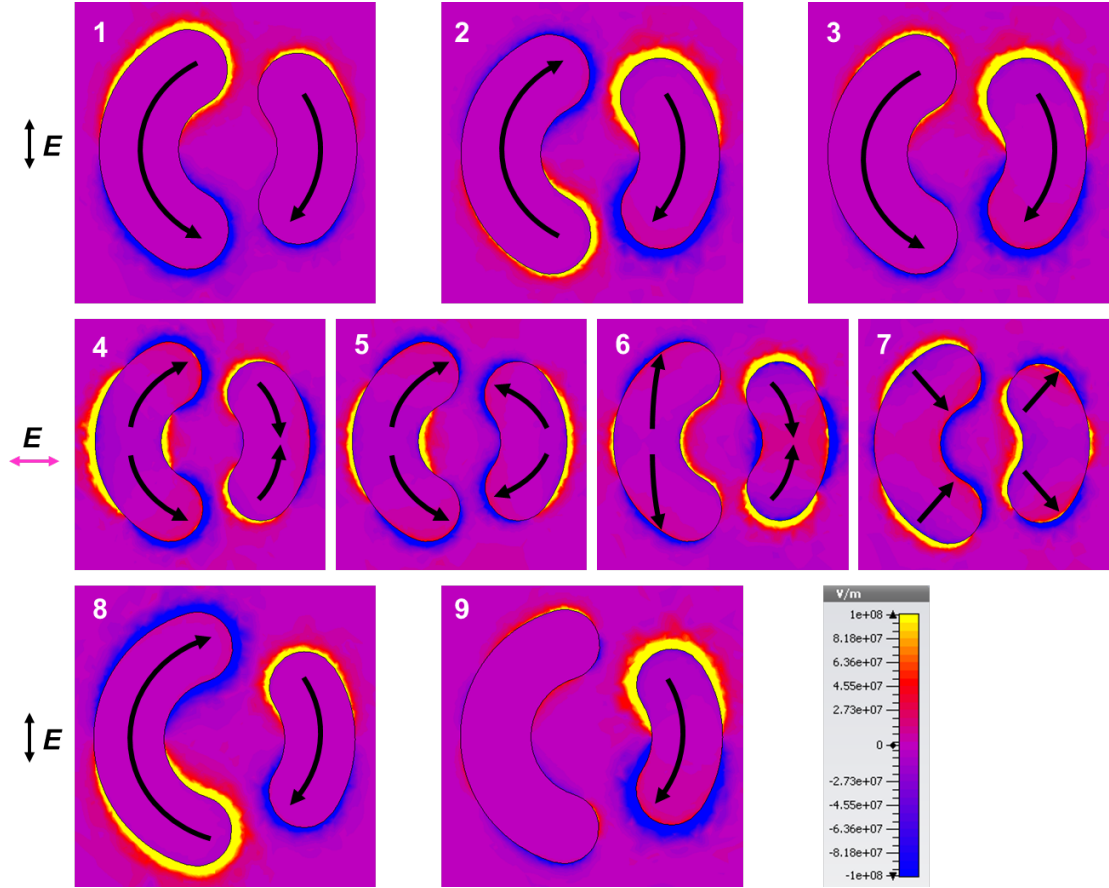


Figure 5.4: The simulated electric field E_z at $z = 15$ nm (component perpendicular to structure) with color code (yellow = positive value, blue = negative value) at the respective resonances in Figure 5.2c with corresponding incident light polarization. Images 1 – 3 show the plasmon modes (represented by black arrows) in sample C at 0° polarization. A subradiant hybridized dark mode is observable at the Fano peak. Images 4 – 7 show the plasmon modes in sample C at 90° polarization. In sample D the Fano resonance disappears due to high asymmetric parameter. Only a bright subradiant hybridized mode (image 8) and a fundamental SRR mode from the shorter arc (image 9) are excited.

polarization, and image 5 shows the dark hybridized subradiant mode. For sample C at 90° polarization, we observe a relatively strong plasmon mode at 480 THz. This mode is a hybridized dipole mode perpendicular to the arcs due to the large width w of the SRRs. This mode can be also excited by 0° polarization, with much smaller modulation depth. For sample D at 0° polarization, the Fano resonance disappears because of the too large asymmetry parameter a . We only observe a subradiant hybridized bright mode 8 at the transmittance dip, which is excited directly from the incident light, due to a relatively large residual aggregate dipole moment in the structure. In mode 9, only the right SRR is excited.

From the experiment and simulation results, we find that the modulation depth of the Fano resonance depends on the degree of asymmetry a . The Fano resonance appears first with broken symmetry and becomes stronger with increasing a . The structure geometry changes also a lot, while we increase the asymmetry parameter a . The difference of the arc lengths l_1 and l_2 becomes larger, which influences the position of the plasmon modes of the two individual SRRs and reduces the coupling strength. Therefore, to achieve a pronounced Fano resonance, we should use the optimum asymmetry parameter a , as well as suitable geometry parameters l_1 and l_2 .

5.2 In-situ annealing

In order to improve the modulation depth of the Fano resonances, we introduce an additional controllable process, namely time-dependent annealing of our samples at various temperatures and simultaneous measurement of their optical behavior by in-situ spectroscopy. A different approach, such as electropolishing of plasmonic structures, was investigated recently by other groups [96, 97]. During the annealing, the gold coalesces due to high surface tension [98]. If the sample is annealed too long, especially for very thin films, for example about 15 nm, as used in our experiment, the structure can be destroyed, and the desired optical properties are not observed.

Annealing is performed using a small hot plate on the sample holder in the FTIR spectrometer and adjusting the temperature accordingly. Hence, only reflectance measurements are possible. A spectrum is recorded every minute, until no changes are observed. In Figure 5.5a, no Fano resonance in the reflectance spectrum of sample C at room temperature (black curve) is observed, and the surface of the structures in the upper inset is rather rough. As the temperature increases to 150°C , a rather unpronounced Fano dip appears in the reflectance spectrum (red curve). With longer annealing at 150°C , the modulation depth of the Fano resonance becomes even larger, and all the resonances shift blue, because the arc lengths become shorter by about 10° during annealing. After 15 minutes, the Fano

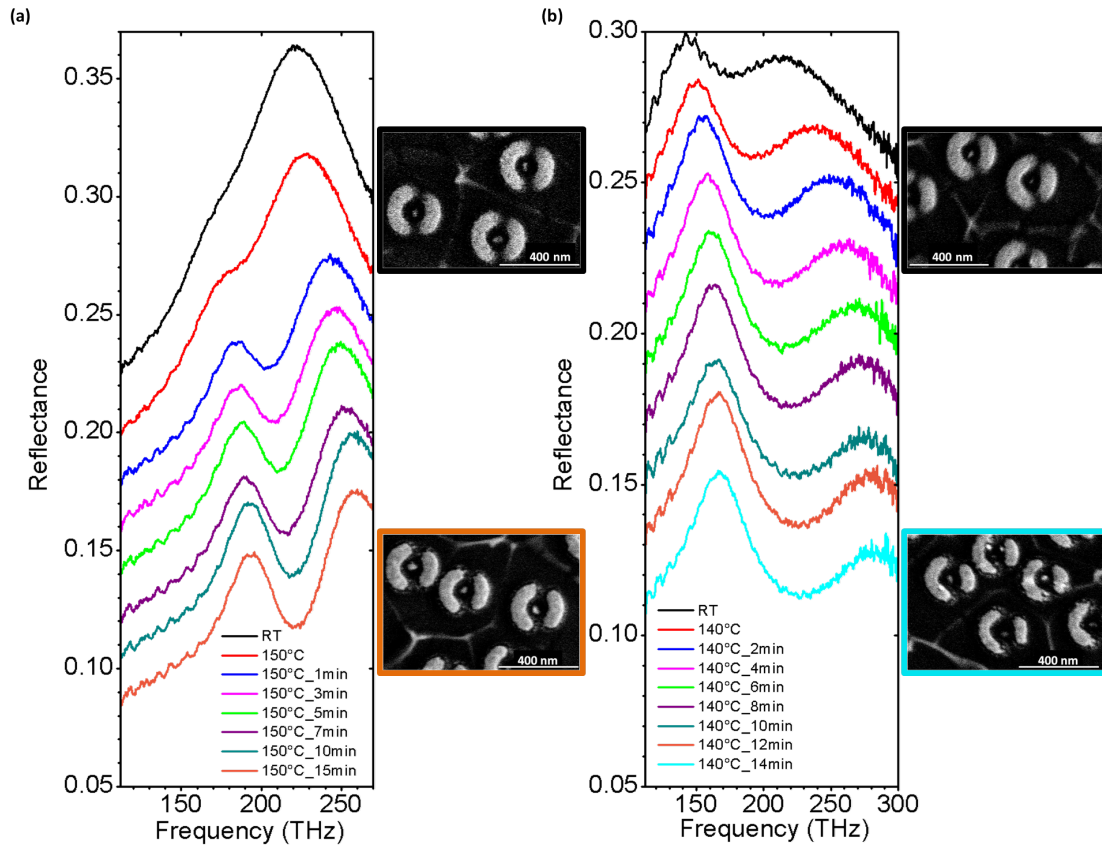


Figure 5.5: In-situ annealing of asymmetric double split-ring resonators. (a) The measured reflectance spectra of sample C, while it is annealed at 150 °C for 15 min. (b) The measured reflectance spectra of sample D, while it is annealed at 140 °C for 14 min. The upper insets show the SEM images of the structures before annealing. The lower insets show the structures after annealing.

resonance becomes very sharp and deep (orange curve), and the structure surface is also much smoother, as shown in the lower inset.

Figure 5.5b shows the in-situ annealing of sample D. At room temperature, only a rather unpronounced Fano resonance is visible in the spectrum, which does exist due to the relatively small gaps before annealing and sufficient coupling. However, because of the high degree of asymmetry, the residual dipole moment in the subradiant mode is relatively large, and this mode is not really dark. During the annealing, the gap size becomes larger by about 10° (~ 15 nm), which reduces the coupling strength. Hence, the Fano resonance disappears quickly, and we only observe a bright hybridized mode at lower energy and a fundamental dipole mode of the right SRR at higher energy.

With the additional in-situ annealing process, the optical quality of our samples can be generally improved, as well as the coupling in the plasmonic elements can be controlled to some extent.

5.3 Fano resonance for LSPR sensing

Localized surface plasmon resonance (LSPR) is the excitation of collective oscillations of electrons in the metallic nanoparticles. LSPR is very sensitive to changes of the surrounding dielectric medium [99], because the electromagnetic field can be strongly enhanced near the metal surface [46]. Because of this property, the resonance can be utilized for sensing application [6].

In order to characterize the efficiency of a LSPR sensor, we use the figure of merit (FOM), which is defined as the energy shift of the plasmon resonance per refractive index unit (RIU) of the surrounding medium divided by the width of the resonance [100]:

$$FOM = \frac{\Delta\lambda(nm)}{\Delta n(RIU) \cdot FWHM(nm)}. \quad (5.4)$$

Therefore, it is important for LSPR-sensing applications to use nanostructures with narrow plasmon resonances. The line width of plasmonic resonance is determined by both intrinsic and radiative damping [101]. In order to reduce the intrinsic damping, we could tune the plasmonic resonance to the wavelength range away from the onset of interband transitions, which is proportional to the imaginary part of the dielectric function (see Fig. 2.3). The radiative damping depends on the total dipole moment of the plasmonic resonance. In complex nanostructures, the total dipole moment depends on the relative phase of the dipole plasmon modes of the individual parts. If the dipoles of the individual nanoparticles oscillate out of phase, the radiative damping will be drastically reduced.

5 Asymmetric double SRRs for Fano resonant sensing

Plasmonic Fano sensors have shown tremendous potential for LSPR sensing due to their large field enhancement as well as their extremely small mode volume, which can reach atto- or zeptoliters [8]. They also show very high sensitivity around the Fano resonance [9]. In order to evaluate the suitability of our low-cost Fano structures for refractive index sensing, we use sample C, which shows the best modulation depth, and measure its transmittance spectra upon exposure to ethanol ($n = 1.354$), butanol ($n = 1.387$) and glycerin ($n = 1.460$), with refractive indices at 1500 nm (Figure 5.6a). We observe the expected redshift of all spectral features. Figure 5.6b shows the simulated transmittance spectra, which agree very well with the experiments.

Here, the resonance shift per refractive index unit for the Fano peak is around 460 nm/RIU in experiment and 560 nm/RIU in simulation. The full width at half-maximum (FWHM) is defined as the distance between the antipeak on the short wavelength side and the peak [102], which is around 170 nm in measurement and 196 nm in simulation, and the corresponding FOM is around 2.7 and 2.9, respectively. The dip in the transmittance spectra at longer wavelength is even more sensitive than the Fano peak, giving a sensitivity of 520 nm/RIU in experiment and 605 nm/RIU in simulation. The FWHM of this dip is around 180 nm in measurement and 125 nm in simulation, and the resulting FOMs are 2.9 and 4.8, respectively. Previous single particle LSPR sensors such as gold nanostars have reached sensitivities up to 665 nm/RIU and FOMs of 5.4 [90, 92]. The best electron beam lithographic structures exhibited FOMs up to 5.7 [103]. Regarding our minimal fabrication effort, our sensitivities and FOMs are suitable for mass productions and could be easily improved in the future by using thicker structures, different geometries, and variation of evaporation conditions.

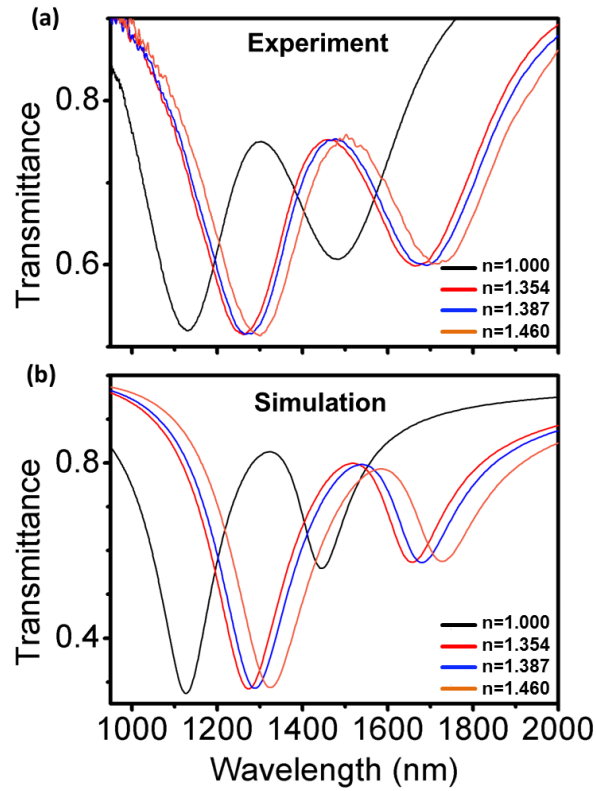


Figure 5.6: Fano resonance in sample C used for LSPR sensing application. (a) Transmittance spectra measured by FTIR for different surrounding media. Air, $n = 1.000$ (black); ethanol, $n = 1.354$ (red); butanol, $n = 1.387$ (blue); glycerin, $n = 1.460$ (orange). (b) Simulated transmittance spectra.

6 Complex plasmonic oligomers

This chapter is based on the publication: [J. Zhao](#), B. Frank, S. Burger, and H. Giessen, *Large-area high-quality plasmonic oligomers fabricated by angle-controlled colloidal nanolithography*, ACS Nano **5**, 9009 (2011)

Plasmonic oligomers have gained a tremendous amount of attention over the last few years. Self-assembled clusters [104], as well as lithographic structures [84, 105–109] opened up the avenue to plasmonic spectra with well modulated features. In particular, coupling of bright and dark resonances leads to destructive interference of the optical fields and hence to the formation of Fano resonances [110–112]. These resonances have been recognized to exhibit giant potential for localized particle plasmon sensing [113]. Applications of refractive index liquids sensing [103, 114] as well as in gas sensing [115], have been demonstrated.

So far, more widespread applications have been hampered by the necessity to use rather complex and hence expensive electron-beam lithography. Only structures with gaps below 20 nm showed considerably modulated Fano resonances. This fact limits typical fabrication sizes of samples in conventional electron-beam lithography systems to about $100 \times 100 \mu\text{m}^2$. Samples with larger areas suffer enormously from inhomogeneities, causing the resonances to shift and hence decreasing their modulation depth.

Here, we introduce an elegant solution to this problem. We utilize another large-area nanofabrication technique: nanosphere lithography to fabricate $10 \times 10 \text{ mm}^2$ high-quality plasmonic oligomers with reproducibly small gaps and desired well-defined structural gapless shapes. The manufactured oligomers show high-quality fundamental as well as higher-order plasmon resonances with Fano transmittance peaks present. We analyze the measured and simulated spectra of plasmonic dimers, trimers, and quadrumers, and assign the different modes. We find self-induced coupling [116, 117] between fundamental dipolar modes and higher-order modes within the same structure, which leads to Fano resonances. This occurs in particular for the case when the plasmonic elements that constitute the oligomer touch each other. For this situation, we examine how structural symmetry breaking allows for tuning the modes and the shapes of the Fano resonances. Finally, we demonstrate that a large-area refractive index sensor with a theoretical figure of merit exceeding 15 can be realized in our structures.

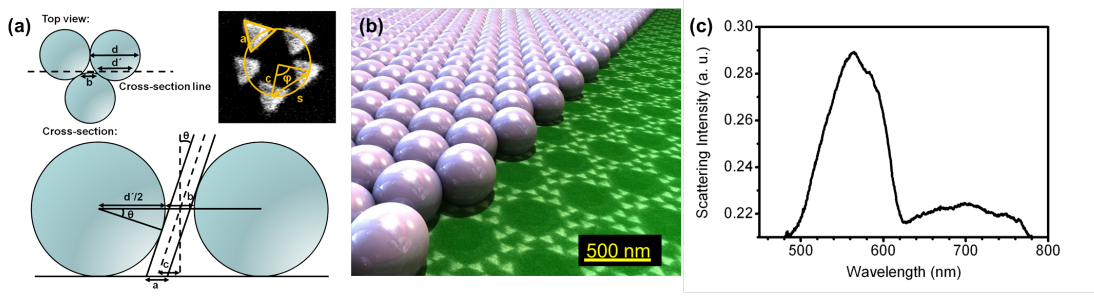


Figure 6.1: Fabrication of oligomers with triangular building blocks. (a) Simplified geometrical model for symmetric pentamer fabrication. Upper left: top view. Bottom: side view at cross section line as indicated in top view. Upper right: geometrical parameters. (b) Artistic view of our fabrication scheme, using a real SEM image of symmetric pentamers. (c) Dark field scattering spectrum of the plasmonic pentamers as shown in b.

6.1 Fabrication details for touching triangular oligomers

For the fabrication of large-area triangular plasmonic oligomers, we use nanosphere lithography as introduced in chapter 3.1.2 and 3.1.3. An annealed (60 s) monolayer of hexagonally close-packed PS nanospheres (500 nm diameter) is used as an evaporation mask. During the evaporation process, the metal vapor beam passes through the apertures of the PS monolayer and creates different structures on the glass substrate depending on the evaporation parameters, as shown in Figure 6.1a. In order to fabricate triangular oligomers, which are arranged on the perimeter of a ring, we set a constant evaporation angle θ . After the evaporation of gold for preparing the first triangle, we rotate the sample by angle $\Delta\varphi$ using the stepping motor when the shutter is nclosed, and then open the shutter to prepare the next triangle and so on. The apertures become smaller while more material is evaporated. In order to fabricate all the triangles in the same size, first only about 10 nm gold is evaporated on each element. Then we rotate the sample back to evaporate another 5 nm gold, also on each triangle, and so on. Less evaporated material and multiple evaporation runs for each element is crucial to achieve the same size of all triangles. In the case of symmetric pentamers with fine gaps, as shown in the top right inset, the length of the triangular element a depends on the diameter of nanospheres d and the size of apertures b , namely the annealing time t , as well as the evaporation angle θ . The aperture size b decreases with longer annealing time. The diameter of the nanosphere cross section is $d' = d - b$ and the

triangle base length is given by:

$$a = b(t) + d' \cdot \left(1 - \frac{1}{\cos \theta}\right) = d - \frac{1}{\cos \theta} \cdot (d - b(t)). \quad (6.1)$$

The distance s between the centers of two triangles also depends on the rotated polar angle $\Delta\varphi$ as:

$$s = 2c \cdot \sin\left(\frac{\varphi}{2}\right). \quad (6.2)$$

Here, c is the distance of one triangle element from the center of the circle in the inset. With $c = d/2 \cdot \tan \theta$, we obtain for the distance s between two elements:

$$s = d \cdot \tan \theta \cdot \sin \frac{\varphi}{2}. \quad (6.3)$$

Figure 6.1b gives an artistic impression of the fabrication process for the symmetric pentamers with gaps. After the lift-off process, multiple triangular elements can be obtained under each aperture of the nanosphere mask, which is different from the well-known vertically evaporated Fischer-patterns [35]. Actually, the structures are periodic over the whole $10 \times 10 \text{ mm}^2$ glass substrate, but contain as well some dislocation defects because of cracks of the mask.

Figure 6.1c shows the dark field scattering spectrum of the triangular plasmonic pentamer, taken with a $70\times$ NA 0.6 microscope objective, a halogen-lamp white light illumination system, and a 25-cm spectrometer. The scattering spectrum was calibrated to the white light lamp spectrum using a rough scattering piece of glass. A broad plasmon resonance is at about 700 nm, and another higher order hybridized mode is obtained at about 560 nm, which is much stronger and sharper. Using different fabrication settings, we can control the geometry parameters very precisely. For example, shorter annealing time will result in larger triangles, and smaller tilted angles θ will result in smaller distances inbetween. Therefore, we can tune the dielectric gaps in oligomers on a nanometer distance scale, even until they vanish. In the following, we are going to analyze the fabricated touching oligomers and discuss their optical properties.

6.2 Optical properties of different oligomers

In Figure 6.2 we show the results of our fabricated gold touching oligomers with different numbers of triangular elements, which are arranged as SRRs. Figure 6.2a shows the SEM images of touching dimers, trimers, and quadrumers, with the used evaporation parameters. We measured the transmittance spectra (Figure 6.2b) of the samples at normal incidence using a FTIR spectrometer with different electric field polarizations. We define 0° polarization parallel to the inter-particle axis between first and last triangle of the oligomers. Figure

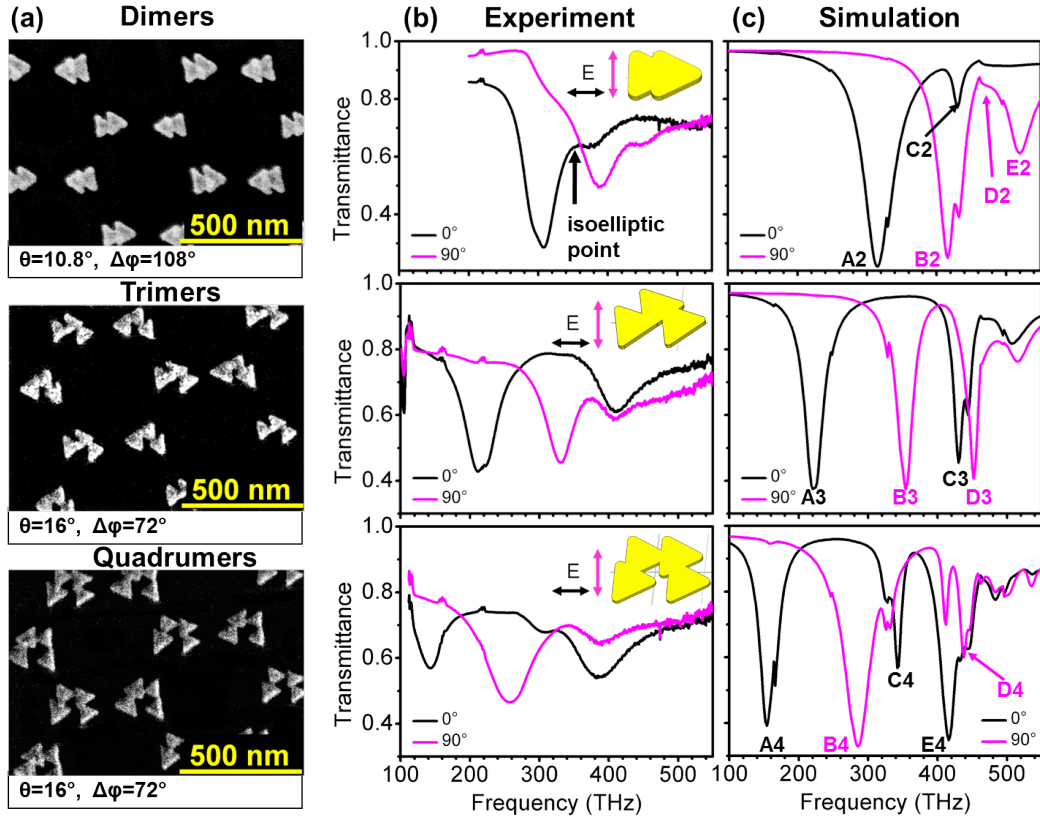


Figure 6.2: Experimental and simulation results using 500 nm nanospheres and a mask annealing time of 75 sec. (a) SEM images of the touching triangular dimers, trimers and quadrumers, which are evaporated with the tilted angles θ and rotation angles and $\Delta\phi$. (b) Experimental transmittance spectra for different polarizations measured with FTIR spectroscopy. (c) Corresponding simulation results (using a finite element model).

6 Complex plasmonic oligomers

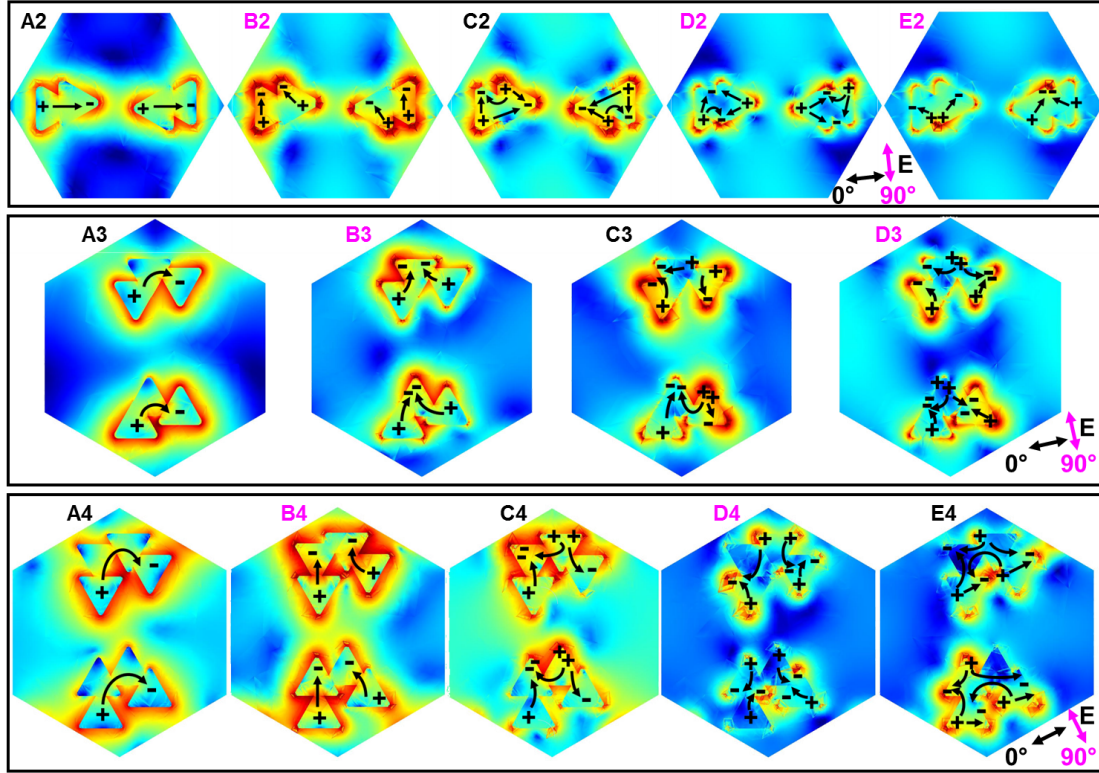


Figure 6.3: Simulated electric field intensity and current distributions for plasmon modes of touching triangular dimers, trimers, and quadrumers. Black (red) labels refer to 0° (90°) polarization. All the images show the XY cross-sections through the simulated field distributions in a unit-cell, at $z = 7.5$ nm above the substrate, through the centers of the oligomers. The pseudo-color images display the natural logarithm of the electric field intensity $\log(E^2)$, normalized to the intensity of the incoming plane wave. The color scale spans a range from -4 (blue) to $+8$ (red). The arrows show the current distributions for each mode. In particular, field plots A3 and A4 demonstrate the analogy of the collective plasmonic oligomer modes to the fundamental mode of a split-ring resonator.

6 Complex plasmonic oligomers

6.2c shows the simulated transmittance spectra obtained with a time-harmonic finite-element solver (FEM code, JCMsuite, Zuse Institute Berlin), which agree with our experiments, taking the inhomogeneous broadening of the experimental spectra into account. The inhomogeneous broadening stems from the fact that the apertures between the polystyrene spheres even after annealing do not all have exactly the same diameters. In the SEM images in Figure 6.2a, we observe two groups of oligomers with differently oriented triangular elements, which are arranged in an approximately mirror symmetric fashion. The reason for this is the opposite orientation of neighboring apertures in our hexagonally close-packed nanosphere monolayer. The difference of the geometry of the two groups of oligomers does not influence the optical spectra very much, except for a slight frequency difference between the resonances of the two different structures in a unit cell, which may lead to a broadening of the resonances in the experimental spectra. In our simulations, we also use a hexagonal unit cell with two groups of triangles with opposite orientations and with feature sizes as in the experiment and as measured by SEM. Bloch-periodic boundary conditions are applied which account for the coupling between oligomers within the 2D array. In the measured and in the simulated spectra we observe at low frequencies fundamental and at higher frequencies higher-order plasmon modes. Pronounced isoelliptical points, where the spectra show the same transmittance value for all polarizations, are observed. These points allow for separation of the fundamental plasmon resonances for the parallel and perpendicular polarization, or between neighbouring higher-order plasmon modes. In order to study the higher-order modes, we examine the electric field intensity and the current distributions of the oligomers at all resonance positions, as shown in Figure 6.3.

For dimers, we observe the fundamental dipolar modes A2 and B2 for both polarizations, with an isoelliptical point separating them. A quadrupolar mode C2 is also observed for 0° polarization as a dip in the transmittance spectrum, which is directly excited by the normally incident light, allowed due to the asymmetric structural geometry with sharp edges. This mode is spectrally located near the dipolar resonance B2 for orthogonal polarization. Additionally, a Fano-type transmittance peak D2 with asymmetric profile appears for 90° polarization, due to the interference of the bright dipolar mode B2 with a dark quadrupolar mode within the same dimer structure. Here, we find the quadrupolar mode in dimers to change from bright to dark when the polarization is rotated from 0° to 90° .

In trimers, due to the SRR-like structure shape, a dipolar mode, namely the 1st-order SRR mode (A3), as well as a 2nd-order (B3), a 3rd-order (C3) and a 4th-order (D3) SRR mode are observable, which are excited either with 0° or 90° polarization, respectively, and separated by pronounced isoelliptical points. With more triangular elements, the structure shape displays a more SRR-like character.

This holds true as well for its optical properties. The D4 mode is usually dark in normal SRR geometry, however, becomes allowed in our case because of the symmetry breaking due to the sharp triangles.

In quadrumers, all SRR modes A4 to D4 are separated by 3 isoelliptical points and excited either with 0° or 90° polarization, respectively. In the same range as the 4th-order SRR mode D4, a hexapolar nanodisk mode E4 is situated, which is excited by polarization 0° . Here, we find that the higher-order nanodisk mode and the higher-order SRR mode can be excited simultaneously, due to the complex nonsymmetric structure geometry.

From the experiment and simulation results, we find that higher-order plasmon modes in our touching triangular oligomers can be directly excited by the normally incident light due to the asymmetric structure geometry. The isoelliptical points in the spectra are very useful to identify the polarization-dependent plasmon modes in our touching oligomers. We can therefore distinguish the bright higher-order modes and the Fano resonance. Additionally, we can observe the higher-order nanodisk modes and the higher-order SRR modes simultaneously in the same structure.

6.3 Self-induced Fano resonance

In some structures with a lower degree of asymmetry, such as dimers, the higher-order plasmon mode can be also dark for a certain polarization. The dark mode couples then with a bright dipolar mode within the same structure, and in the same spectral range, resulting in a "self-induced" Fano resonance. A similar situation was found by Nordlander et al. in substrate-induced Fano resonances in Ag nanocubes [116], as well as in a single metallic nanodisk with a missing wedge-shaped slice [117]. In some hybridized plasmonic structures with different individual elements, such as nanoparticle aggregates [1, 102, 103, 107, 118], nonconcentric ring/disk cavities [70, 114, 119], or stacked nanostructures [87], similar effects occurred. However, in these structures, strong coupling between the resonances of individual elements requires small dielectric gaps of just a few nanometers in planar structures or 3D arrangement, which rely on complicated fabrication techniques.

In order to study the modulation depth and hence the strength of higher-order plasmon modes and the associated Fano resonances, which arise due to "self-induced" coupling effects, we simulate transmittance spectra for dimers with the same triangle length $a = 140$ nm and thickness $h = 17$ nm as the fabricated sample shown in Figure 6.2a at normal incidence, using the frequency-domain solver CST Microwave Studio. In this case we use a rectangular unit cell and a single group of triangles.

First, we align the two triangles with their inter-particle axis along the x-axis and one of their edges pointing into x-direction. We define s as the distance

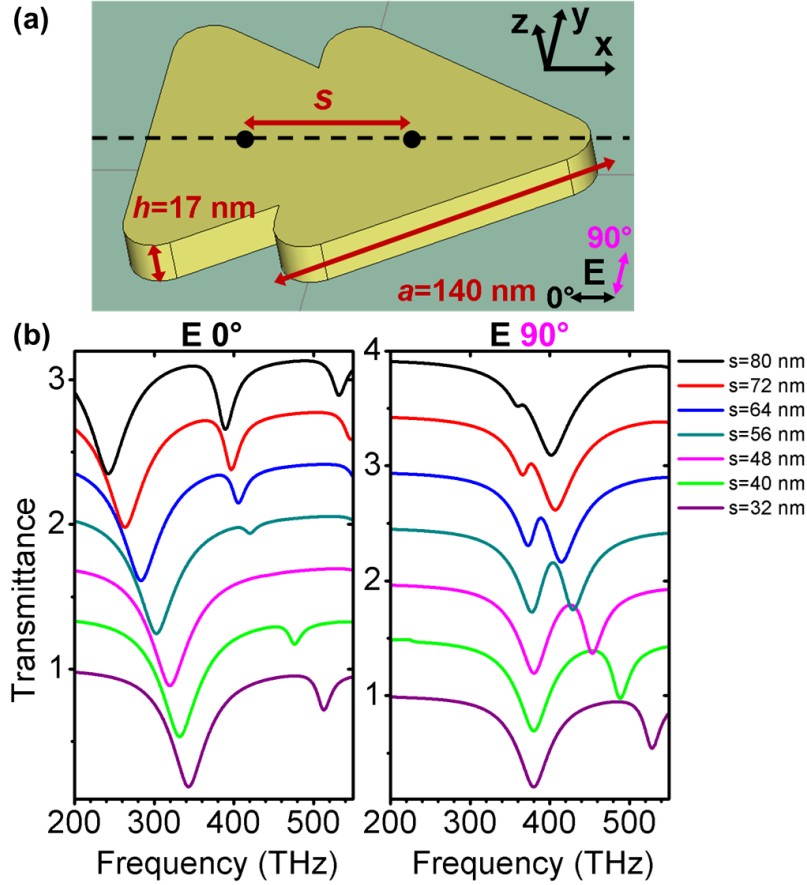


Figure 6.4: (a) Schematic dimer structure used for simulation with length of the triangle $a = 140$ nm, thickness $h = 17$ nm, and distance of two triangles s . The polarization of the used normal incident light 0° is along the x axis. (b) Simulated transmittance spectra for different distances s with polarization 0° (left) and 90° (right), using CST Microwave Studio.

6 Complex plasmonic oligomers

between the centers of the two triangles. Polarization 0° is along the x-axis, as depicted in Figure 6.4a. Figure 6.4b shows the simulated transmittance spectra for different distances s . For 0° polarization, the fundamental dipolar mode shifts from 250 THz to 340 THz and the bright quadrupolar mode shifts from 410 THz to about 510 THz with decreasing s . Additionally, the resonance depth of the quadrupolar mode becomes smaller at first and then larger again. For $s = 48$ nm, the quadrupolar mode disappears completely in the spectrum, which indicates that the residual dipole moment of the structure is extremely small, and this mode becomes dark. For 90° polarization, we observe a very weak dipole-dipole-coupling for large values of distance s (black curve) because of the large residual dipole moment of the quadrupolar mode. With decreasing distance s , the quadrupolar mode becomes dark, resulting in a stronger Fano resonance. Also, because of the smaller distance and the same triangle length, the quadrupolar mode shifts blue, whereas the dipolar mode for 90° polarization remains almost at the same position, which results in a more symmetric shape of the Fano resonance. When s is smaller than 56 nm, the Fano resonance becomes asymmetric again, as the quadrupolar mode shifts even more towards the blue with decreasing s . The shape of the Fano resonance changes also, because the quadrupolar mode becomes bright again with decreasing s and couples directly to the incident light.

Keeping a constant distance $s = 56$ nm, we now rotate both of the two triangles around their centers and simulate the transmittance spectra for different angle α , for both 0° and 90° polarization, as shown in Figure 6.5. For $\alpha = 0^\circ$, we observe one bright quadrupolar mode q1 at about 410 THz for 0° polarization. In case of 90° polarization, we observe coupling of a dark quadrupolar mode Q1 with the bright dipolar mode, leading to a Fano resonance that is visible as transmittance peak at about 380 THz. In the next step, we lift the degeneracy of the quadrupolar mode by breaking the symmetrical arrangement of the two triangles by rotation of the two triangles 5° around their centers. At 0° polarization, we observe two weak bright quadrupolar resonances q1 and q2 at 410 THz and 380 THz. For 90° polarization, the removal of the degeneracy leads to a double Fano resonance by interaction of the two dark quadrupolar modes Q1 and Q2 at about 380 THz and 410 THz with the bright dipole. Afterwards, we evaluate the evolution to even more rotation $\alpha = 10^\circ$. For 0° polarization, we observe only one bright quadrupolar mode q2. For 90° polarization, the Fano resonance due to the quadrupolar mode Q1 also disappears, while the Fano resonance due to Q2 becomes stronger. With increasing rotation angle α , the two triangles tend to be arranged in a more symmetric fashion with a new symmetry axis. Upon further increased angles $\alpha = 20^\circ$ and 30° , the bright quadrupolar mode q2 for 0° polarization shifts red. The line shape of the Fano resonance Q2 for 90° polarization becomes very similar to that at small distance s in Figure 6.4 b, because the quadrupolar mode Q2 also

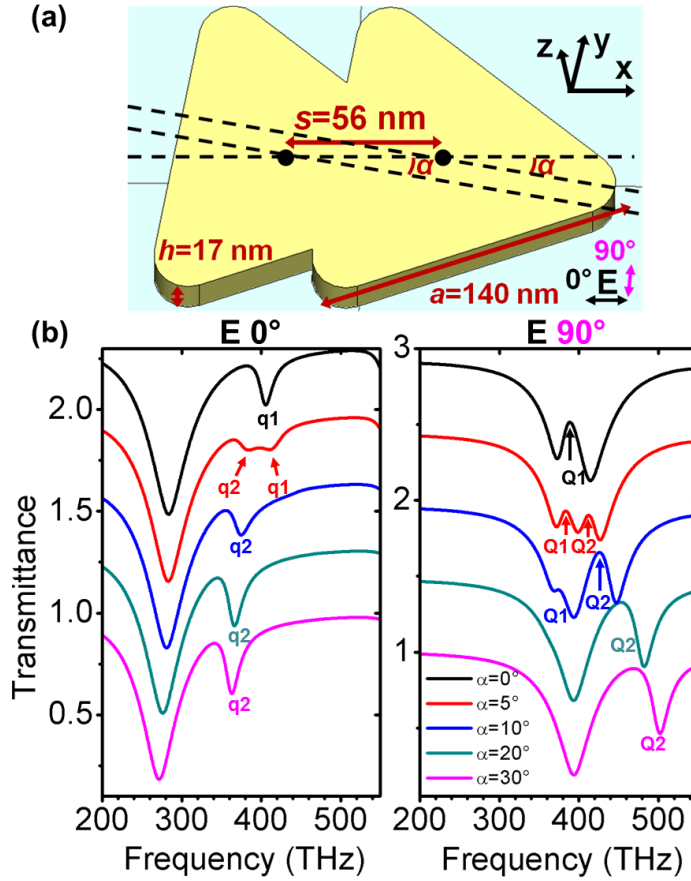


Figure 6.5: (a) Schematic dimer structure used for simulation with length of the triangle $a = 140$ nm, thickness $h = 17$ nm, distance of two triangles $s = 56$ nm, and rotated angle α around the centers of the triangles. The polarization of the used normal incident light 0° is along the x axis. (b) Simulated transmittance spectra for different angle α with polarization of 0° (left) and 90° (right), using CST Microwave Studio.

becomes bright with larger α and couples directly to the normally incident light.

From these simulations we infer that the brightness of higher-order plasmon modes in our gapless oligomers depends very strongly on the exact structure geometry. Due to the complex and asymmetric structural shape, most of the characteristic higher-order modes contain some residual dipole moments. Therefore, to determine whether a higher-order mode is dark or bright, depends on its dipole moment being small or large. In order to achieve well-modulated Fano resonances, we should design our touching oligomers with suitable structural asymmetry. The structural geometry should be tuned such that the higher-order mode in this structure is dark, and it should be situated in the same spectral range as the dipolar mode. The number of triangle elements, overlap area, and arrangement of the triangles play the key roles. The self-induced coupling of the bright dipolar and higher-order dark modes in the same structure with well-tuned structural asymmetry can be achieved more easily with our simple fabrication technique.

6.4 Self-induced Fano resonance for LSPR sensing

Due to the localized electric fields and the narrow line shapes, Fano resonances are ideal candidates for LSPR sensors, as introduced in chapter 5.3. In order to test the sensitivity of the Fano resonance in our dimers upon refractive index changes, we analyzed structures with the same symmetric arrangement as in Figure 6.4a to ensure the darkness of the quadrupolar mode. We used thicker structures with larger size, which are more sensitive to the surrounding medium. Figure 6.6 shows the simulated transmittance spectra of symmetrically arranged touching dimers, with 200 nm triangle length and 40 nm thickness, for different surrounding media with thickness of about 100 nm. The refractive indices are 1.33 (black) and 1.34 (red), respectively.

The Fano resonance shift per refractive index unit $\Delta\lambda/\Delta n$ is around 530 nm/RIU in our spectra. The FWHM of the Fano resonance is about 30 nm, and the corresponding FOM of dimers would be around 17. If we use the definition of Peter Nordlander [102], who considers the distance between the antipeak on the short wavelength side and the peak as the FWHM, in our case, this value would be 21 nm. The corresponding FOM of dimers would then be around 24, which shows that our dimer structure can provide an excellent sensing platform.

6 Complex plasmonic oligomers

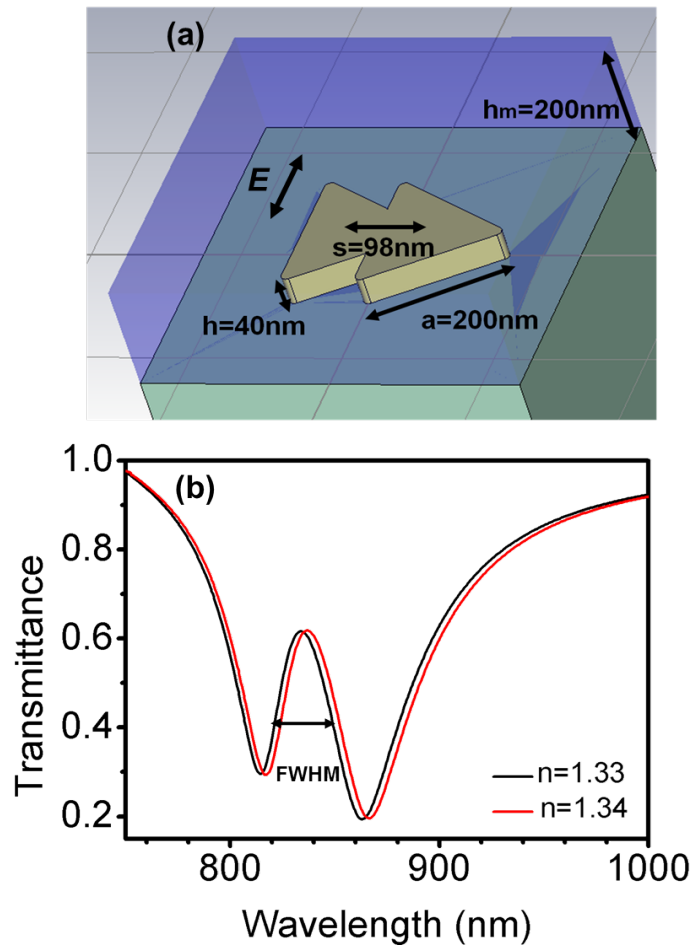


Figure 6.6: Fano resonances in dimers used for LSPR sensing applications. (a) Schematic diagram of the dimer structures in different dielectric surrounding media. (b) Simulated transmittance spectra for different surrounding media. The refractive indices are 1.33 (black) and 1.34 (red). The FWHM of the Fano peak is 30 nm.

7 Direct contact Au-Pd sandwiches for hydrogen sensing

The highly sensitive detection of hydrogen is important in many industrial processes, and becomes a major safety concern with the fast development of fuel cell technology. The concentration of hydrogen gas mixed with air exceeding 4% leads to the high risk of explosion. Palladium (Pd), one of the most catalytically active transition metals, is usually used as the detection element, due to its thermodynamically suitable and fully reversible hydride formation characters [120]. The electrical and dielectric properties of Pd, which change on hydrogen exposure, can be used for both electrical and optical hydrogen sensing. Recently, Pd-based optical hydrogen sensors have attracted significant attention [39, 121–123], which utilize localized surface plasmon resonances (LSPRs) of metallic nanostructures. As introduced in chapter 5.3, LSPRs are associated with collective oscillations of free electrons, which can generate large field confinement in an extremely small volume, and very sensitive to changes of the refractive index of the surrounding medium. The LSPR of the Pd nanoparticle is used to demonstrate the metal-hydride formation qualitatively and quantitatively. Nevertheless, the LSPRs of Pd possess very broad resonance features, which is a large obstacle for precise detection of hydrogen gas. Very recently, indirect optical sensing for hydrogen was introduced [10, 40, 124–126] using bimetallic nanoantenna system, consisting of Au and Pd, which shows a much better plasmon resonance than that of the pure Pd system. In this chapter, we introduce the Pd-hydride formation process in simple Pd nanodisks, as well as in the heterometallic systems. Furthermore, we demonstrate direct contact Au-Pd sandwiches for easily prepared, low-cost, and large-area hydrogen sensors.

7.1 Introduction of Pd-based hydrogen sensing

Using simple Pd nanodisks, hydrogen storage through metal-hydride formation has been studied in ref. [39]. Figure 7.1a shows the hydrogen uptake process in the Pd lattice. First, the hydrogen gas is dissociatively adsorbed at the surface of the Pd structures, followed by diffusion of hydrogen atoms into the lattice. The atomic hydrogen is then localized on the interstitial sites of the host metal lattice, which

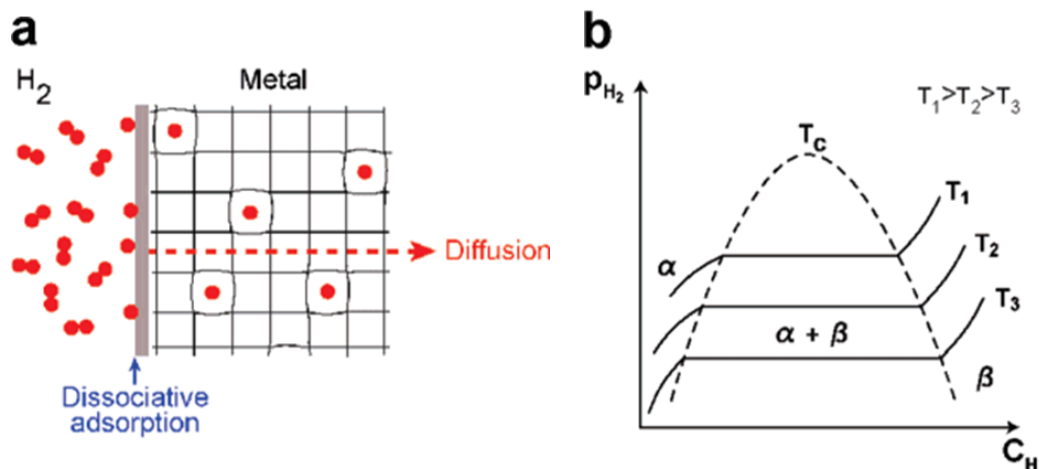


Figure 7.1: (a) Hydrogen uptake in Pd lattice and (b) hydrogen pressure-composition isotherms for the thermodynamic aspects of metal-hydride formation [39].

leads to an expansion of the lattice in the hydrided metal system.

The plasmonic response of the Pd nanostructures constructs isotherms by systematically recording optical extinction spectra for increasing and decreasing H_2 pressures, as shown in Figure 7.1b. The pressure-composition ($p-C$) isotherms are presented using the extinction coefficient at LSPR maximum, E_{max} , and the LSPR peak position, λ_{max} , as functions of H_2 pressure, which resembles the typical pressure-concentration isotherms for Pd-H system [127]. At low H_2 pressure, both E_{max} and λ_{max} change very small, as some hydrogen is dissolved in a solid solution by the host metal, which is called α -phase. With further increasing pressure, the nucleation occurs due to the interactions between the dissolved hydrogen atoms, and the hydride (β) phase grows. In the $\alpha + \beta$ -phase coexistence region, both E_{max} and λ_{max} change drastically and show a plateau for a nearly constant hydrogen pressure. The width of the plateau determines the amount of H_2 that can be stored reversibly with very little pressure variation. Upon further increase of the H_2 pressure, the changes of E_{max} and λ_{max} are again very small, yielding large H_2 pressure changes, as expected for the pure β phase. The two-phase coexistence region is strongly temperature dependent, and ends at a critical point T_c . Above T_c the transition from the α -phase to the β -phase is continuous.

Figure 7.2a shows the SEM image of the fabricated array of Pd nanodisks with the diameter of 300 nm and the thickness of 20 nm, using hole-mask colloidal lithography [39]. The extinction spectra of this sample are measured using different H_2 pressures and shown in Figure 7.2b. The LSPR peak position shifts red and the

7 Direct contact Au-Pd sandwiches for hydrogen sensing

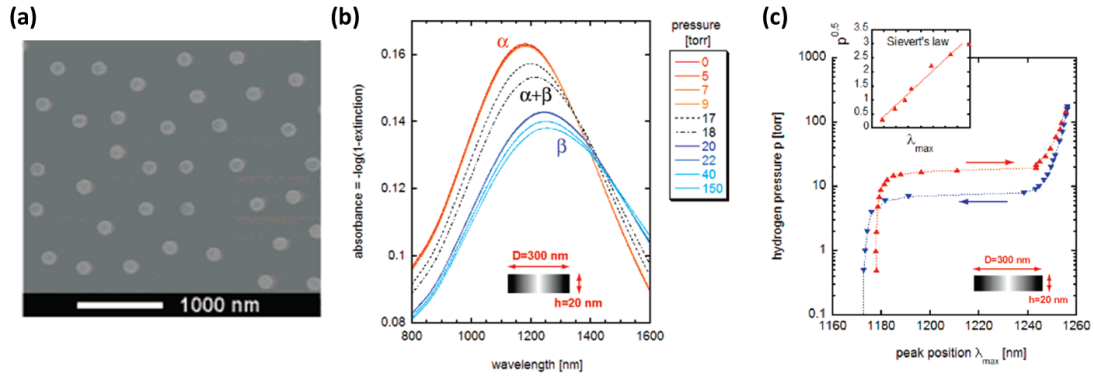


Figure 7.2: (a) SEM image of an array of Pd nanodisks fabricated with hole-mask colloidal lithography with the diameter $D = 300$ nm and the thickness $h = 20$ nm. (b) The measured extinction spectra of the sample in the low H_2 pressure (α -phase) range (red and orange solid lines), around plateau pressure (black dotted and dashed lines), and in the high H_2 pressures (β -phase) range (blue and turquoise solid lines). (c) $P - \lambda_{max}$ isotherms for hydrogen uptake and release in the Pd nanodisks at room temperature [39].

total cross section decreases with increasing H_2 pressures, as the system changes from α -phase (red and orange solid lines) to β -phase (blue and turquoise solid lines). The measured LSPR peak positions in Figure 7.2b are displayed as a function of the hydrogen pressure and shown in Figure 7.2c. The $p - \lambda_{max}$ isotherms for hydrogen uptake (red curve) and release (blue curve) in the Pd nanodisks show an obvious plateau at about 18 Torr, which agrees with the measured values for thin Pd films, as reported in the literature [128]. The maximal shift of the LSPR peak is about 80 nm.

7.2 Introduction of indirect Pd-based optical hydrogen sensing

As the plasmon resonance of pure Pd nanostructures possess very broad profiles, which results from interband transitions in the whole visible region, indirect optical hydrogen sensing system, consisting of Au as fine plasmonic material and Pd, were introduced. Figure 7.3 shows the study of hydride formation of single stacked Au/SiO₂/Pd nanocones fabricated with hole-mask colloidal lithography [129]. The base diameter of the gold disk is about 105 nm, and the thickness about 40 nm. A 15 nm high Pd nanodisk with diameter of about 75 nm is stacked above the gold

7 Direct contact Au-Pd sandwiches for hydrogen sensing

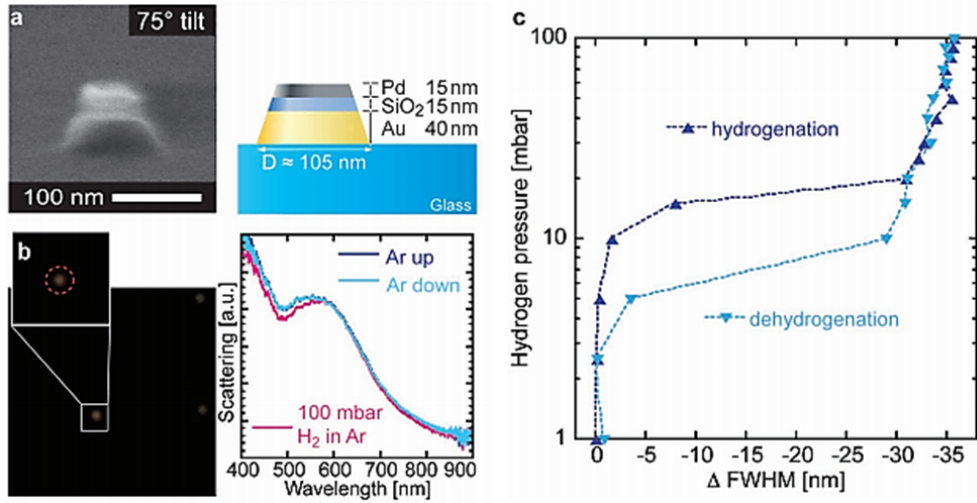


Figure 7.3: Hydride formation in single Au/SiO₂/Pd nanoparticle as indirect optical hydrogen sensor. (a) The tilt environmental scanning electron microscope image (left) and a schematic depiction (right) of the indirect nanoplasmonic sensing, consisting of 40 nm high Au and 15 nm high Pd, with a 15 nm thick SiO₂ spacer layer. (b) Dark-field scattering image of the single Au/SiO₂/Pd nanocone (left) and the measured spectra (right) to subsequent exposure to 100% Ar, 10% H₂ in Ar, and then 100% Ar again. (c) Corresponding optical $P - \Delta FWHM$ isotherms at 23 °C [129].

disk with a 15 nm thick SiO₂ spacer layer inbetween. The 75° tilt environmental scanning electron microscope image (left) and a schematic depiction (right) of the single bimetallic nanoparticle are shown in Figure 7.3a. This sample was measured using dark-field scattering (DFS) spectroscopy. The DFS microscopy image (left) and the spectral response (right) from subsequent exposure to 100% Ar, 10% H₂ in Ar, and then 100% Ar again are shown in Figure 7.3b. The LSPR peak in the scattering spectra shows very clear and reversible shift, which is induced by the transformation of the Pd particle into PdH_x, and the resulted significant changes of the dielectric properties. The change in the FWHM of the LSPR peak of the system as a function of hydrogen pressure at 23 °C is shown in Figure 7.3c. The hydrogenation (blue curve), as well as dehydrogenation (light blue curve) process is clearly visible in the optical isotherm, and distinct α -, $\alpha + \beta$ -, and β -phase regions are shown as discussed earlier.

Another example of the indirect nanoplasmonic sensing for hydrogen is resonant antenna-enhanced single-particle sensor in the visible region, consisting of a Pd nanoparticle near to a Au triangle antenna with a dielectric gap in nanometer size,

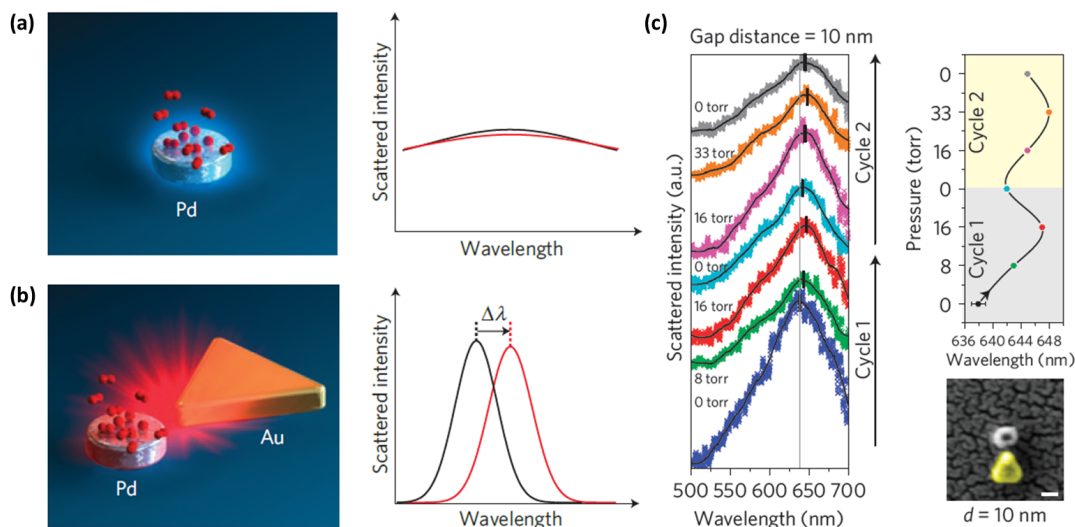


Figure 7.4: Schematic representation of antenna-enhanced single-particle hydrogen sensor and optical scattering measurements. (a) Hydrogen sensing with a single pure palladium nanoparticle, which scatters weakly and shows damped broad spectra. (b) Hydrogen sensing using a single palladium-gold triangle antenna, which scatters much more strongly. Hydride formation of the system results in a resonance shift ($\Delta\lambda$). (c) Optical scattering measurements of the single palladium-gold triangle antenna on hydrogen exposure [10].

as shown in Figure 7.4b [10]. The LSPR in this system is much better modulated and more easily to read out for the hydride formation process than that in a pure Pd nanoparticle (Figure 7.4a). The optical scattering measurement of a single Pd-Au triangle antenna, with the side length of Au triangle of about 110 nm, the diameter of Pd disk of about 60 nm, and the gap size of about 10 nm, is shown in Figure 7.3c. The thickness of Au and Pd particle is about 40 nm and 60 nm, respectively. The hydrogen pressure for the measurement is raised from 0 torr to higher pressures and back to 0 torr again. Two cycles are shown in the left spectra. The LSPR peak positions for the two cycles are extracted from the spectra to highlight the red shift in dependence on the hydrogen concentration (Figure 7.4c right), which shows a maximal value of about 10 nm. The hydrogen absorption in the palladium particle is indirectly detected by monitoring the Au antenna resonance, by the changes of the dielectric function in the hydride formation process.

7.3 Direct contact Au-Pd sandwiches for hydrogen sensing

So far, the study of the hydrogen sensing has focused on plasmonic nanostructures with geometries where the constituent materials are coupled laterally. In contrast to such laterally coupled systems, which often require precisely control of fabrication approaches for nanosize gaps, sensing devices where gold and palladium in the system show direct contact can be fabricated in a single lithographic step, enabling straightforward high-throughput processing. Here, we demonstrate a novel hydrogen sensing scheme, which incorporates simple hybrid plasmonic nanostructures, consisting of stacked gold and palladium nanodisks without a spacer layer in between, as shown in Figure 7.5. Using this direct contact design, the plasmonic character of palladium can directly take part in the hydride formation process with a large change of the dielectric data. The plasmonic response of the whole system, with the gold present, is much more sensitive than that of the pure Pd system, resulting in an obvious and more observable spectral shift upon hydrogen exposure. Particularly, we study the influence of stacking order and geometry to find an optimal arrangement for a hydrogen sensor device numerically and experimentally. Our samples yield large absorption and scattering signals and large-area sample sizes of about 1 cm^2 , fabricated by low-cost hole-mask colloidal lithography.

The SEM images and the simulated, as well as the measured spectra of four different nanosandwich structures consisting of Au and Pd are shown in Figure 7.6. The corresponding schematic view of each structure design is depicted in the inset of the SEM image in the left column. All the Au and Pd disks have the same geometries, with the diameter of about 150 nm and the thickness of about 20 nm. Due to the hole clogging effect during evaporation, the disk on the top layer shows a slightly smaller diameter. The cobweb-like structures in the SEM images arise from the residual PMMA from the fabrication process, which has nearly no influence to the optical properties of the structures, except a small red shift of the spectral peak.

We use finite element method (FEM) for the single particle scattering simulations of the four systems (as shown in the center column of Figure 7.6) with tabulated Pd (blue curve) and PdH (red curve) data [130]. The LSPRs for the four systems show a red shift and broadening using PdH dielectric data compared to using Pd data. The Au-Pd-Au sandwich structure shows a well modulated plasmon resonance, but a quite small shift of about 16 nm (Figure 7.6e), as this designed system consists of more Au material. However, the contact surface of the Pd disk to the hydrogen gas is reduced due to the covering of the Au disks in both top and bottom layers. The Pd-Au and the Pd-Au-Pd structures show very

7 Direct contact Au-Pd sandwiches for hydrogen sensing

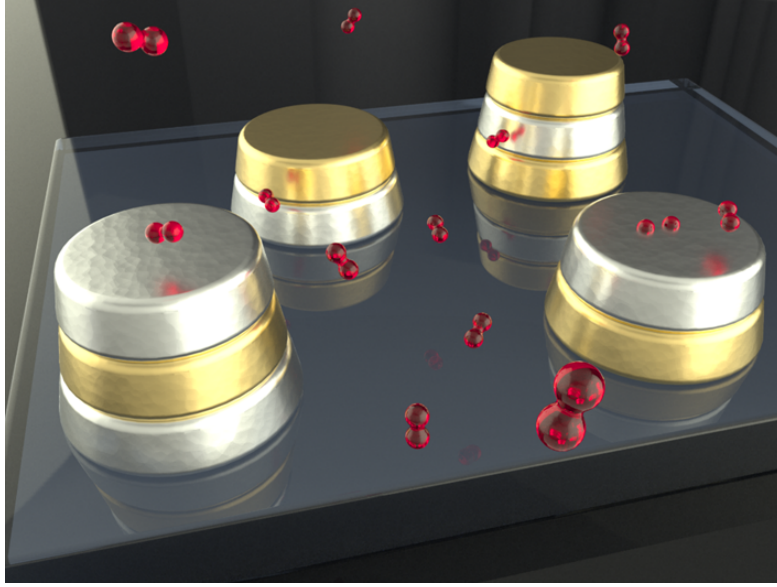


Figure 7.5: Schematic view of four different investigated direct contact Au-Pd nanosandwich systems.

broad plasmon resonances and large spectral shifts, as the LSPR responses of both systems are mainly from the bottom Pd disks, which are directly deposited on the glass substrates, and the change of the dielectric function from Pd to PdH affects more to the plasmonic properties of the whole systems. The resonance shift of the Pd-Au-Pd sandwiches (Figure 7.6k) is about 10 nm larger than that of the Pd-Au structure (Figure 7.6h), due to higher Pd content in the three-layer structures.

The ensemble extinction spectra of four fabricated direct contact nanosandwich structures over large area are shown in the right column of Figure 7.6, which are measured using a white light transmission spectroscopy system, with pure nitrogen atmosphere (blue curve), as well as 4 vol.% hydrogen in nitrogen gas (red curve). The experimental results of the first two sandwich systems (Figures 7.6c and f) agree very well with the simulations both in the FWHM and the position of the resonance. The red shift, as well as the broadening of the LSPR upon hydrogen exposure tallies with the calculated results. The direct contact two-layer Au-Pd nanosystem (with the Au disk in the bottom layer) shows an experimental resonance shift of about 30 nm, which is much larger than the values in recent work of indirect optical hydrogen sensing [10]. However, for the two systems with Pd as bottom disks (Figures 7.6i and l), the experimental results show relatively large differences to the simulations. Firstly, the measured spectra shift more blue than the calculations, which could be from the fabrication or material defects, for example, from the clogging effect. The nanodisks on the top layer might be

7 Direct contact Au-Pd sandwiches for hydrogen sensing

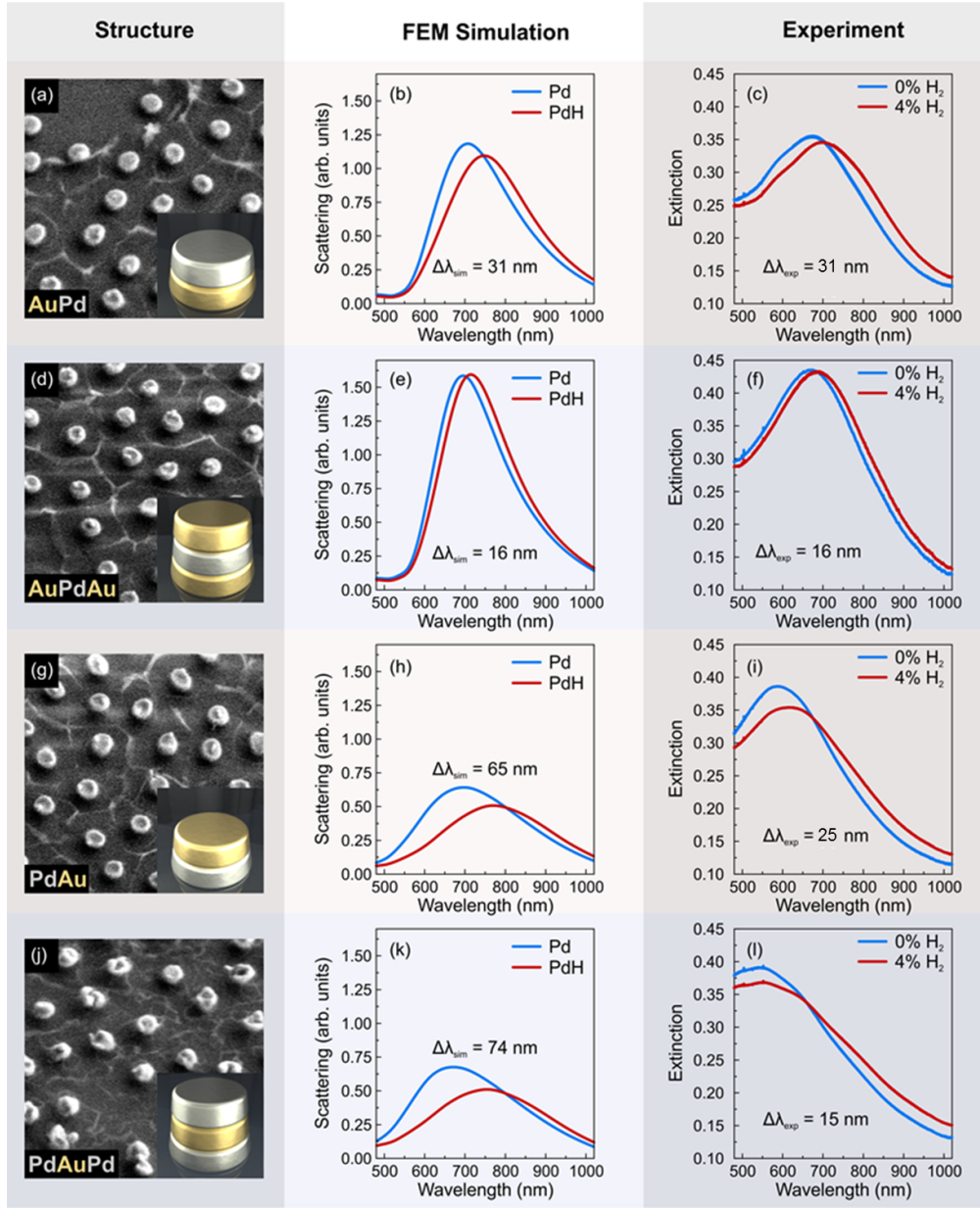


Figure 7.6: Simulated and measured spectra of the nanosandwich structures with and without hydrogen. (a) SEM image of the two-layer Au-Pd system. (b) Single particle scattering FEM simulations of the Au-Pd system using tabulated Pd (blue) and PdH (red) data. (c) Extinction measurements of the fabricated Au-Pd system without (blue) and using 4 vol.% (red) hydrogen in nitrogen. (d)–(l) Simulation and measurement data for the other three sandwich systems.

7 Direct contact Au-Pd sandwiches for hydrogen sensing

significantly smaller than expected, but it is difficult to confirm this, as one can not distinguish Au and Pd materials in the SEM measurements. The other big difference between the experimental and simulation results is the spectral shift upon hydrogen exposure. Theoretically, the nanosandwich systems with Pd disks in the bottom layer show stronger spectral shifts when exposed to hydrogen, since for the glass substrate, which has a higher refractive index than air, a concentration of electric energy is formed close to the Pd-glass interface. Another reason is that Pd has a higher intrinsic damping than Au, which leads to higher Ohmic losses in the material. Therefore, there is always higher current density in Pd than Au structures with the same surrounding medium. The experiments only produce very small shift upon hydrogen exposure for the two systems, which is attributed to the measurement system. The used white-light setup is designed for recording spectra in the wavelength range 500 – 1000 nm and hence the resonances here are already at the edge of our measurement region with more noisy data. Most certainly not the full maxima but rather a cut flank is recorded. This is supported by the fact that the calculated peak amplitude and broadening are well reproduced in experiment, as we use larger nanosandwich systems with the diameter of about 220 nm, which show red shifted resonances localized in the suitable recording range of the setup. The large Pd-Au-Pd sandwiches (220 nm) exhibit a maximal red shift upon hydrogen exposure of about 45 nm, whereas Au-Pd system with diameter of 220 nm only shows about 30 nm (not shown here).

In the context of industrial hydrogen sensing, detector geometries with a large optical change upon hydrogen exposure are only useful if that change happens on a reasonable timescale. Therefore, to evaluate the performance of a plasmonic geometry for hydrogen sensing applications, it is not only important to look at the final optical response for hydrogen concentrations, but also to study the temporal behavior of the device. Figure 7.7 shows the hydrogen loading and unloading dynamics for various concentrations in all four direct contact Au-Pd systems. In the experiments, ensemble extinction spectra are recorded every 5 seconds, while the samples are exposed to sequences of hydrogen in nitrogen gas at a constant gas flow-rate of 1 l/min. The sequence starts with 200 s of 0.5 vol.% H₂ in N₂, then for 200 s pure N₂, after that 200 s of 1 vol.% H₂ in N₂ and so on, until a maximum H₂ concentration of 5 vol.% is reached. We calculate the center of mass of the measured extinction spectra and plot the centroid shift as a function of real time. This calculation method offers a very robust and reliable way of detecting even very small resonance shift independent of the peak shape and noise in the spectral data [131].

Figure 7.7a shows that the two-layer Au-Pd system, with gold disks in the bottom layer, gives experimentally not only the strongest shift of about 30 nm, but also the fastest loading behavior with about 50 s to reach the maximum response

7 Direct contact Au-Pd sandwiches for hydrogen sensing

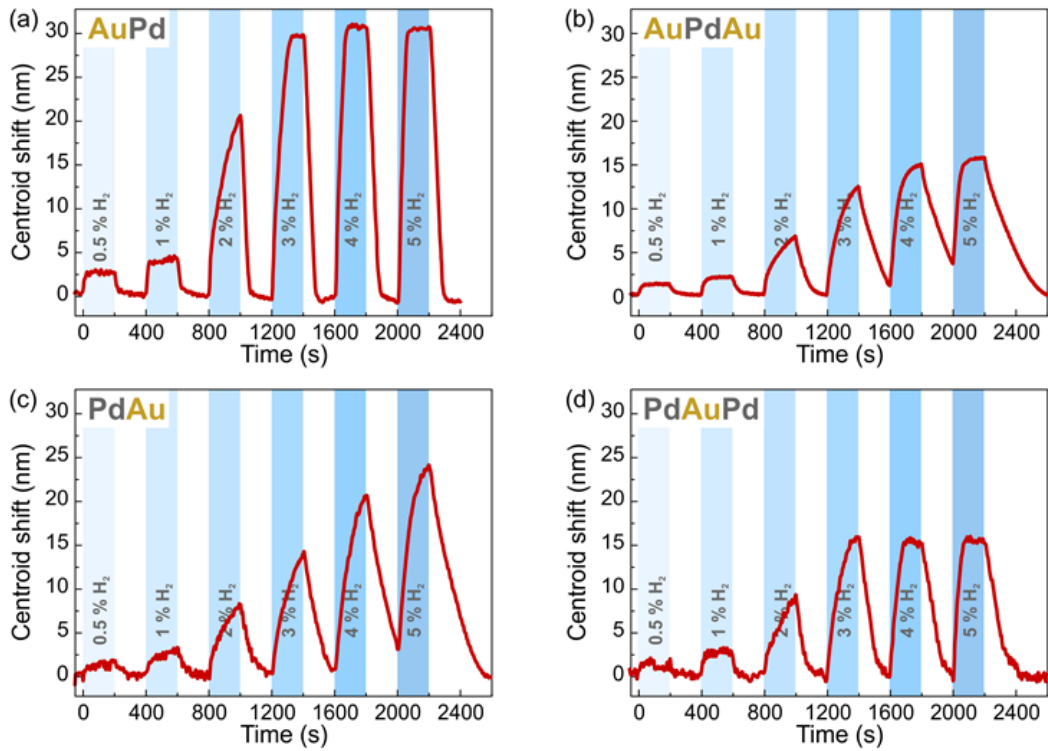


Figure 7.7: Time traces of the centroid wavelength shifts upon a representative sequence of hydrogen gas exposure, from 0.5 – 5 vol.% hydrogen in nitrogen for (a) the Au-Pd system, (b) the Au-Pd-Au system, (c) the Pd-Au system and (d) the Pd-Au-Pd system. All four systems show a distinct and reversible reaction to the different hydrogen concentrations.

7 Direct contact Au-Pd sandwiches for hydrogen sensing

to H₂, as well as the fastest unloading time of about 100 s. Regarding the loading times, only the three-layer Pd-Au-Pd structure (Figure 7.7d), with palladium disks in the bottom layer, is comparable with a loading time of about 70 s at 5 vol.% H₂ and an unloading time of about 120 s. For the other two geometries with a gold disk covering the whole system, the unloading times are above 200s for both cases and the loading time is about 100 s for the Au-Pd-Au system (Figure 7.7b) and above 200 s for the Pd-Au case (Figure 7.7c). The strongly increased reaction times in these two geometries result from the reduced contact surface of Pd disks to the hydrogen gas. Upon the hydrogen exposure, only the sidewalls of the Pd disks provide the needed catalytic surface for splitting and adsorbing the hydrogen gas. For the unloading process, all hydrogen ions have to desorb through the bottleneck of the sidewalls. Otherwise, the Au-Pd-Au sandwich reacts slightly faster than the Pd-Au system, due to clogging effect in the fabrication process, which leads to a relative smaller size of the Au disk in the third layer of Au-Pd-Au system than that of the Au disk in the second layer of the Pd-Au system. Since all samples are manufactured using the same materials under the same conditions and measured directly after fabrication, the strong differences of the temporal behavior cannot be attributed to material differences or sample degradation [132].

Examining all four time-traces one can see that no matter how fast the sensor reacts, the maximum centroid shift is only concentration-depend up to about 3 vol.% H₂ in N₂. For higher concentrations, only the reaction time changes. Additionally, the centroid shift shows a strong jump at about 2 vol.% H₂, and the maximum centroid shift per hydrogen concentration rises suddenly from 5 nm to above 10 nm, whereas below 2 vol.% H₂, the maximum centroid shift is almost linearly dependent on the hydrogen concentration. This behavior is typical for palladium nanostructures and related to the so-called α - to β -phase transition, as introduced in chapter 7.1.

From the time-dynamic measurements of the four direct contact Au-Pd systems, we can conclude that not only optical response of one nanoplasmonic hydrogen sensor, but also the relative "free surface area" of Pd structure in the sensor system is important for a highly effective detection of H₂ gas.

8 Advanced 3D and multishape hole-mask colloidal lithography

This chapter is based on the publications: [J. Zhao](#), S. Jaber, P. Mulvaney, P. V. Braun, and H. Giessen, *Repetitive hole-mask colloidal lithography for the fabrication of large-area low-cost plasmonic multi-shape single-layer metasurfaces*, Adv. Opt. Mater. in press (2014), and [J. Zhao](#), B. Frank, F. Neubrech, C. Zhang, P. V. Braun, and H. Giessen, *Hole-mask colloidal nanolithography combined with tilted-angle-rotation evaporation: A versatile method for fabrication of low-cost and large-area complex plasmonic nanostructures and metamaterials*, Beilstein J. Nanotechnol. **5**, 577 (2014).

With the development of optical research, nanostructuring for tailored optical functionality is required, using more complex nanostructures. We have improved our large-area fabrication: hole-mask colloidal lithography to realize three-dimensional (3D) structures with stacking technique, or multishape structures on the same metasurface. In this chapter, we will introduce the advanced fabrication details and study the optical functionality of the fabricated samples for possible applications. In the end, we also combine the 3D and multishape fabrication together for large-area C_3 symmetric 3D SRRs as chiral metamaterials.

8.1 3D fabrication

For 3D fabrication, we use stacking technique with a dielectric spacer layer between two metallic structure layers. The simplest examples are shown in Figure 8.1, which are vertically evaporated using hole-mask with the hole size 220 nm. Figure 8.1a shows two-layer gold disks, with gold thickness 20 nm and spacer layer magnesium fluoride (MgF_2) 70 nm. Due to the clogging effect of the hole-mask, a vertical tapering is clearly visible and leads to a strongly decreasing disk diameter for thick structure geometry, i.e., >100 nm. The first evaporated disk structures have a diameter about 220 nm, which is the same as the mask-hole size, and the second evaporated disk structures show only about 160 nm diameter. The more materials we evaporate, the smaller upper structures become. As shown in Figure 8.1b, the gold disks on the top layer have only about 100 nm diameter, due to the evaporation of one more MgF_2 spacer layer with thickness of 70 nm.

The optical transmission spectrum of the two-layer gold disks is taken with perpendicularly incident nonpolarized light and shows two resonances at about 760 nm and 1020 nm, which depict the superradiant hybridized mode and the subradiant hybridized mode, with the electron in the two layer disks oscillating in and out of phase, respectively. The spectrum of the three-layer gold disks also shows mainly two plasmon resonances with slightly red shift when compared to the two-layer sample, at about 790 nm and 1030 nm, which might be from more dielectric materials in the whole systems, namely one more 70 nm thick spacer layer, or from a weak coupling of the small disk on the top layer. Due to the big difference of the disk sizes, the coupling of the smallest disk with the others is extremely weak. In the spectrum it shows mainly a fundamental dipole mode, which is present only as a shoulder at about 680 nm. At a large spacer thickness of 70 nm, strong phase retardation effects are already present, and one needs to consider far-field coupling effects [133].

Figure 8.2 shows two complex 3D structures fabricated with hole-mask lithography combined with tilted-angle-rotation evaporation. Figure 8.2a shows right-handed 3D gold SRRs with a ring radius $r = 125$ nm, a ring width $w = 60$ nm, and a gold thickness h of about 10 nm. For the fabrication, we use 230 nm thick PMMA layer and a hole-mask with the hole-diameter of 119 nm. First we evaporate MgF₂ disks, with a thickness of about 30 nm, using a constant tilt angle of 22.5°. Afterwards, we change the material crucible in the vacuum chamber and directly evaporate normal gold SRRs using the same hole-mask and the same tilted angle. With the polar angle controllable motor during the evaporation, one side of the gold SRR is exactly deposited on the MgF₂ disk. Due to the clogging effect of the hole-mask, the fabricated disks are not perfectly shaped cylinders, but rather more circular truncated cones. Thus, one side of the gold SRRs has a small vertical slope to form a 3D geometry.

This sample is measured using FTIR spectroscopy with linearly polarized light. We define that 0° polarization is along the SRR gaps. The first- and third-order SRR modes are clearly observed at about 70 THz and 180 THz and the second-order mode at around 130 THz is also visible for 0° polarization (black curve), which differs from the planar SRR and results from the 3D structuring. For 90° polarization (pink curve), the second-order SRR mode is well modulated and clearly observed, meanwhile, the first-order mode is also presented as a shoulder. For 45° polarization, we always observe the three SRR modes simultaneously, both for planar or 3D SRRs.

In Figure 8.2b, an other complex 3D oligomer structure is shown, which consist of three gold disks in the first arranging in an L-shaped pattern, followed by a spacer and one more disk above the disk 1. For the fabrication of this sample, we use 220 nm diameter PS spheres and 480 nm PMMA. The azimuthal tilted angle

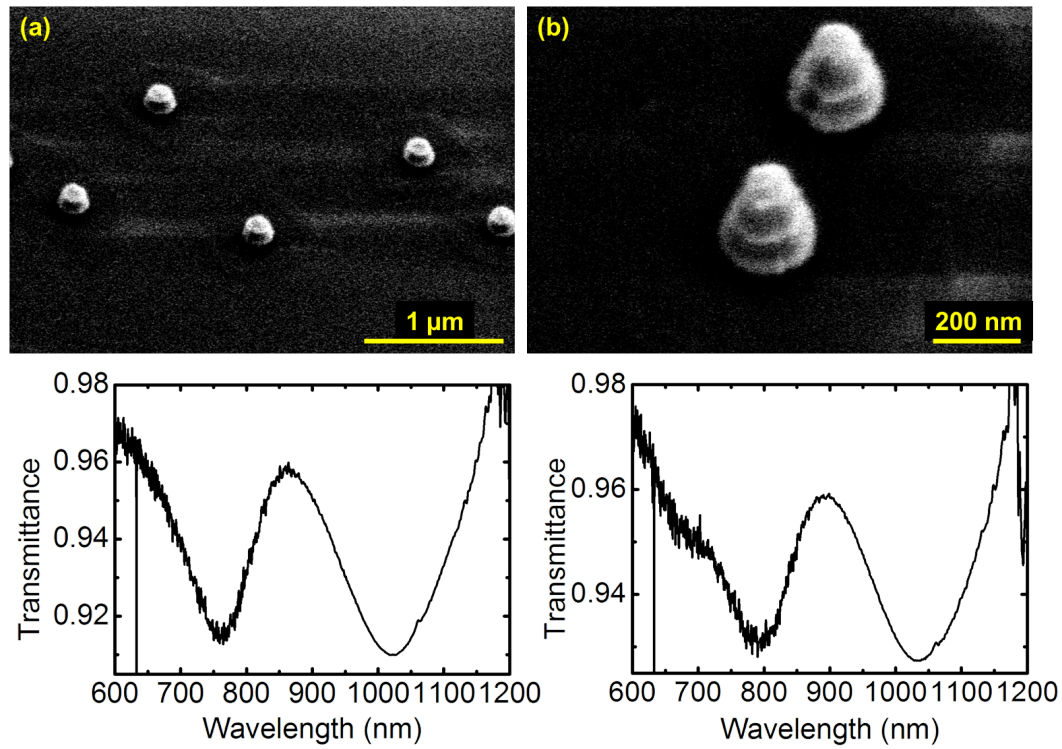


Figure 8.1: Simple 3D structures fabricated with hole-mask colloidal lithography. (a) two-layer stacked gold disks. (b) three-layer stacked gold disks. The gold thickness is 20 nm for both samples, and the spacer layer is MgF_2 with 70 nm thickness. The measured transmittance spectra are shown in the bottom row. The small modulation depth of the resonances is from the low density of the structures, which can be tuned very flexibly using different PS concentration in the mask preparation process.

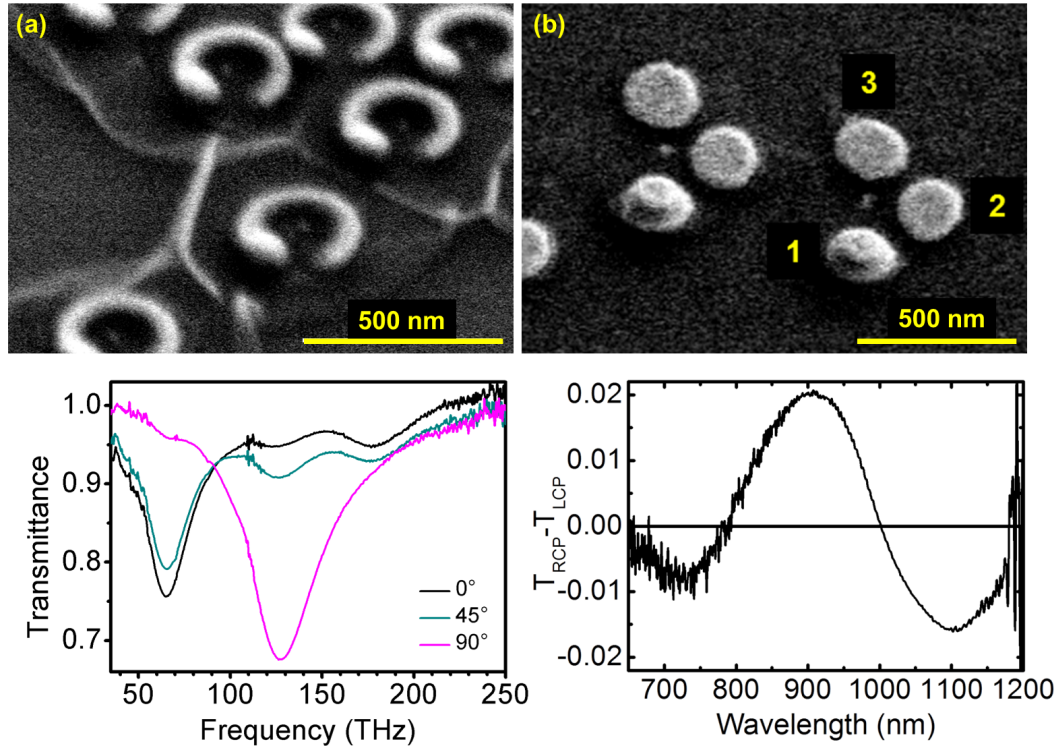


Figure 8.2: Complex 3D structures fabricated with hole-mask colloidal lithography and tilted evaporation. (a) 3D gold SRRs with the ring radius $r = 125$ nm, the ring width $w = 60$ nm, and the gold thickness h about 10 nm, and the thickness difference of the two sides of SRR about $\Delta h = 30$ nm. The transmittance spectra of this sample are measured with linearly polarized light with 0° (black curve, parallel to the gaps), 45° (blue curve), and 90° (pink curve) polarizations. (b) 3D oligomers with three gold disks on the bottom layer and another one on top of the first bottom disk using MgF_2 as spacer layer. The diameter of the bottom disks is about 200 nm and the top one is about 120 nm. This sample is measured with circularly polarized light, and the circular dichroism $T_{RCP} - T_{LCP}$ is shown.

θ for the evaporation is about 21° . All the gold disks have a thickness of 20 nm and we use MgF_2 as spacer between the stacked two gold disks with a thickness of about 35 nm. The upper layer gold disks (diameter of about 120 nm) are slightly smaller than those in the bottom layer (diameter of about 200 nm), due to the clogging effect.

In order to study the chiral optical properties of this pattern, we introduce at first circular dichroism (CD) [134–136]. CD is defined as the difference in absorbance for right- and left-handed circularly polarized (RCP and LCP) light. Our experimental-setup only allows reflectance and transmittance measurement for circularly polarized light in a very small frequency range. Within this spectral region, the differences between absorbance and extinction (1 - transmittance) indicate no significant deviations [137]. Therefore, we calculate the transmittance difference (ΔT) between RCP- and LCP-light to determine the chiral properties of our sample, and plot it in Figure 8.2b bottom. Due to the same orientation of all structures, exhibiting no C_3 or C_4 symmetry of the arrangement, elliptic birefringence arises from the biaxiality of our sample. Therefore, the contributions of polarization conversion will be expected to the measured $\Delta T_{RCP-LCP}$ spectra. According to this, we use the calculation introduced in references [2, 19] to obtain the real chiral response:

$$\Delta T = 0.5 \times (\Delta T_{RCP-LCP}^{top} - \Delta T_{RCP-LCP}^{bottom}). \quad (8.1)$$

We measure the transmittance difference $\Delta T_{RCP-LCP}$ of our sample with both top and bottom illumination, and assume that the mean value determines correct CD ΔT -values. The spectrum shows clearly nonzero values, signifying strong plasmonic chiral response. The details about the relationship between the sign of the CD spectra and the handedness of the related modes are discussed in [41, 138]. Such structures might be very useful in the future for the generation of local chiral fields for sensing.

8.2 Repetitive hole-mask colloidal lithography

Using our normal large-area methods, such as nanosphere lithography and hole-mask colloidal lithography, only a single shaped element can be deposited, which can be repeated either regularly or in a random fashion. To combine more different elements for the realization of low-cost multi-functional nano-optical devices over square centimeter areas, we need to be able to create a wide variety of nanostructures mixed and deposited on the same substrate with maximum flexibility, both in terms of choice of motif and choice of materials. Particularly, all elements should be placed on a single metasurface, which is on the top surface of one sample, to obtain desired plasmonic resonances in the visible and

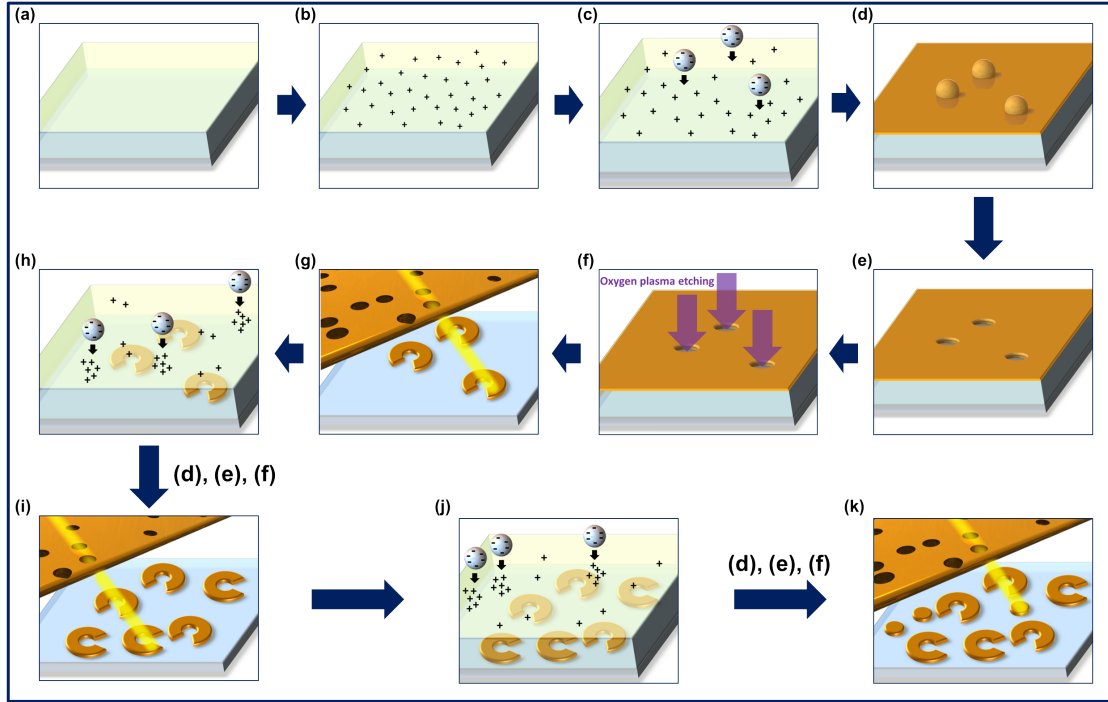


Figure 8.3: Fabrication scheme of repetitive hole-mask colloidal lithography. (a) Spin coating of PMMA onto a substrate. (b) Drop-casting of positively charged PDDA solution onto the PMMA film. (c) Deposition of negatively charged PS spheres onto the PMMA film. (d) Evaporation of a thin layer of gold as an etching mask onto the PS spheres. (e) Removal of the PS spheres. (f) Oxygen plasma etching. (g) Tilted-angle-rotation evaporation of the first set of gold nanostructures (in this case SRRs) using the prepared gold hole-mask created by the first layer of PS spheres. (h) Deposition of a second layer of PS spheres onto a second PMMA film, which is spin coated onto the previous sample and covered with PDDA, then repeating processes (d), (e), and (f). (i) Evaporation of a second set of gold nanostructures (in this case 90° rotated SRRs) using the second hole-mask prepared on the same substrate. (j) Deposition of a third layer of PS spheres onto a third PMMA film, then repeating of processes (d), (e), and (f) again. (k) Evaporation of a third set of gold nanostructures (in this case plasmonic disks) using a third hole-mask on the same substrate layer. This method can in principle be repeated, until a high density of structures is reached.

simultaneously in the infrared, and to warrant interaction with other materials. This is specifically important for SEIRA or SERS. In order to fabricate truly chiral plasmonic substrates, two conditions need to be fulfilled, namely the individual nanostructures need to exhibit chirality of a certain handedness, and the orientation of the individual chiral nanostructures needs to have C_3 - or C_4 -symmetry, on a single surface.

Here we use multiple repetitions of low-cost and high resolution hole-mask colloidal lithography to fabricate large-area high-density complex plasmonic nanostructures with variable shapes, which are mixed well and arranged on one single metasurface, for realization of real multi-functional optical devices. This method is not a simple repetition of the normal hole-mask colloidal lithography, which was used for our previous work, but an obvious advance and perfection of this fabrication technique, as one must take care of more details and parameters for successful fabrication of multi-shape metasurfaces. For example, by controlling the mask-hole density as well as the evaporation parameter, the concentration of each set of structures can be tuned, to avoid overlapping and clustering, and the structure size of each element can be controlled precisely, respectively. This advanced fabrication method allows for the integration of different shapes and even different materials into one nanostructured composite.

The repetitive hole-mask fabrication process is depicted in Figure 8.3. We use conventional fabrication technique, as introduced in chapter 3, to create the first set of structures. The mask preparation includes spin coating of a PMMA layer (Figure 8.3a), drop casting of positive charged polyelectrolyte solution PDDA (Figure 8.3b), followed by drop casting of negatively charged PS spheres (Figure 8.3c), evaporation of a 20 nm gold film as an etching mask (Figure 8.3d), lift-off of the PS spheres (Figure 8.3e), and finally oxygen plasma etching (Figure 8.3f). Afterwards, we use tilted-angle-rotation evaporation with the prepared hole-mask to create the first set of SRRs (Figure 8.3g). The second set of structures is formed by repeating the same hole-mask preparation process on the sample coated with the first set of gold structures. A slight waviness of the second PMMA layer arises from modulation by the first set of structures. Hence, the distribution of the positive charge from the PDDA solution is strongly influenced. More positive charge accumulates on the regions where there are no metallic structures under the PMMA film (Figure 8.3h). The PS spheres of the second repetition, which define the positions of the mask-holes, prefer to settle on these metal-free regions through electrostatic interactions. Utilizing the second gold hole-mask, another set of nanostructures with a different geometry to the first set can be evaporated over empty regions of the substrate (Figure 8.3i). By optimizing the density of the PS spheres, and by choosing an appropriate design for the nanostructures being deposited, the two different structures can be well

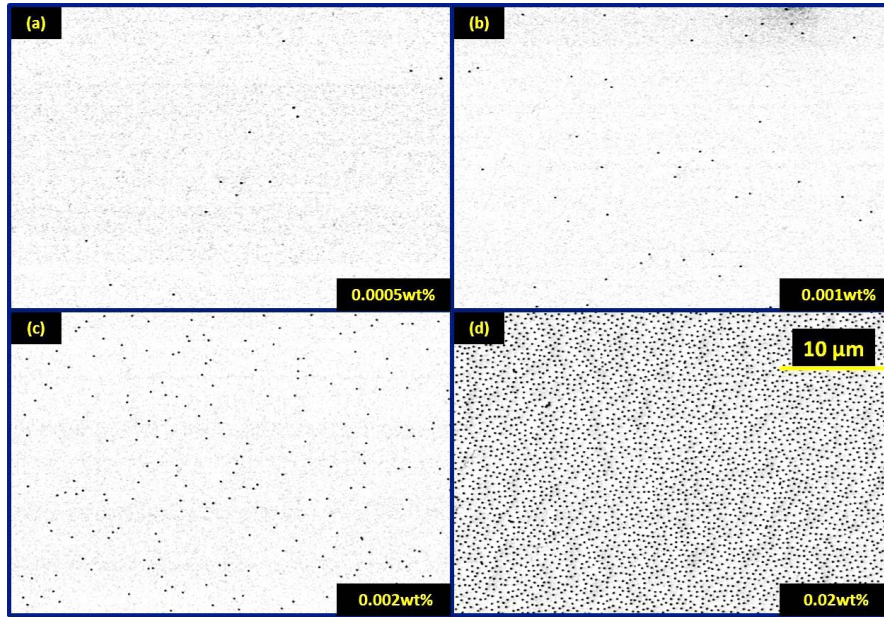


Figure 8.4: SEM images of gold hole-masks with prepared different PS sphere concentrations (shown in the lower-right corners). The PDDA concentration is 0.05 wt% for (a) and (b), 0.1 wt% for (c), and 0.2 wt% for (d). The hole-density of the mask is about $0.01 \mu\text{m}^{-2}$ (a), $0.04 \mu\text{m}^{-2}$ (b), $0.18 \mu\text{m}^{-2}$ (c), and $3.2 \mu\text{m}^{-2}$ (d). The wavy structures in d are observed once sufficient oxygen plasma etching has taken place. 119 nm diameter PS nanospheres are used in all samples.

separated laterally. By controlling the concentration of PS spheres deposited for each repetition, multishape samples with up to 3 different types of nano-motifs incorporated into the final material are formed, as shown in Figure 8.3j and 8.3k. Of course, as the number of different shapes increases, the fabrication becomes more difficult and the overall optical quality of the sample slightly decreases.

8.2.1 Control of the mask-hole densities

The most important parameter for repetitive hole-mask fabrication is the density of deposited PS spheres used in each fabrication cycle. To enable a larger number of different structures on the same substrate, the concentration of the PS sphere solution should be low to avoid clustering after deposition. The concentration of the PDDA solution should also be appropriate to the PS solution concentration due to electrostatic interactions. Figure 8.4 shows SEM images of the hole-masks for varying hole-densities. The PS solution concentrations are indicated in the lower-

right corners. The values here are typical for the 119 nm diameter PS spheres (Polysciences, Inc.); other PS sphere sizes require different parameters. For a low density of mask-holes, as shown in Figures 8.4a and 8.4b, 0.0005 wt% and 0.001 wt% of the PS solution was used, respectively. The PDDA solution in both cases has a concentration of 0.05 wt%. The mask in Figure 8.4a possesses an extremely low particle density, which allows investigation of single nanostructures via dark field microscopy. The hole density is about $0.01 \mu\text{m}^{-2}$ for Figure 8.4a and $0.04 \mu\text{m}^{-2}$ for Figure 8.4b.

For optical characterization of substrates containing multiple different shapes, the density of the features should be tuned to a suitably low value. If the structure coverage is too low, the optical signal-to-noise ratio is too weak in measurements. For three-shape samples, the hole density coverage (about $0.18 \mu\text{m}^{-2}$), as shown in Figure 8.4c, is used for each repetition of fabrication, which is formed from a 0.002 wt% PS solution and a 0.1 wt% PDDA solution. For a single-shape samples, the highest possible structure density can be fabricated to generate strong optical signals, as shown in Figure 8.4d, for which a 0.02 wt% PS concentration and a 0.2 wt% PDDA solution is used. Due to the electrostatic repulsion between the PS spheres, there is a plateau in the sphere density that can be achieved, which is about $3.2 \mu\text{m}^{-2}$ for the 119 nm diameter PS spheres. This plateau is reached at a PS concentration of about 0.01 wt%. Higher concentrations do not result in higher pattern densities. The 0.2 wt% PDDA solution used to obtain the highest structure coverage also turns out to be suitable for other size PS spheres. With this concentrated PDDA solution, saturated surface coverage can be attained, using a 220 nm diameter PS solution with about 0.08 wt%. In our case, the neighbor-to-neighbor distance is larger than a few tens of nanometers, hence plasmon hybridization effects due to lateral coupling are unlikely to play a dominant role [139].

8.2.2 Correction factor for multiple evaporation

Another important parameter for the repetitive fabrication process is the tilted angle θ for the evaporation. For ring-like structure geometry, the radius of the ring r depends on the PMMA layer thickness h_0 and the tilted angle θ since $r = h_0 \tan\theta$, as introduced in chapter 4.1. For the second fabrication cycle, the spin coated PMMA layer on a substrate, which has already nanostructures on it, is slightly thicker than the first time spin coated PMMA on a clean substrate, even using the same spin coating parameters. Due to the existence of the first set nanostructures on the substrate, the hydrophobicity of the substrate surface is enhanced, resulting in a thicker spin coated PMMA layer. Figure 8.5a and 8.5b show two-shape samples, which are fabricated by two repetitions of mask preparation and subsequent metal evaporation. We use exactly the same tilted

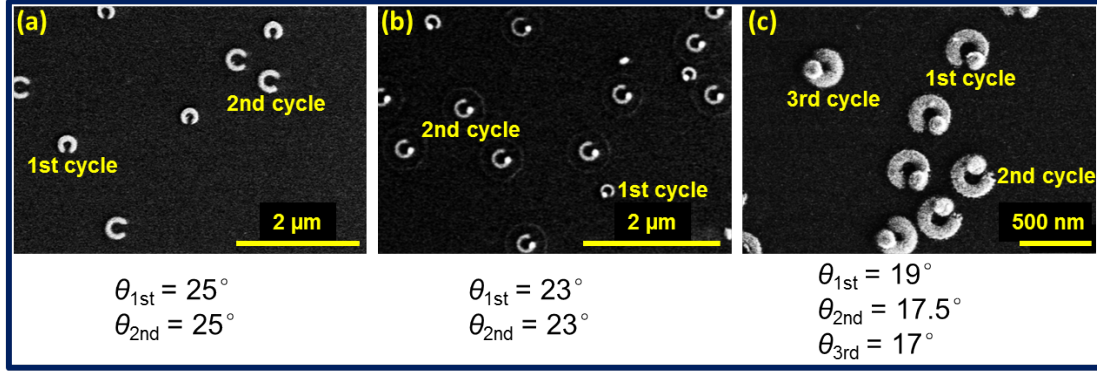


Figure 8.5: SEM images of the fabricated two- and three-shape samples with the tilted angles θ for each cycle evaporation. (a) Two 90° rotated SRR shapes, which are evaporated using the same tilted angle $\theta = 25^\circ$. (b) Two 120° rotated 3D SRR shapes, which are evaporated with the same tilted angle $\theta = 23^\circ$. (c) C_3 -symmetric 3D SRR shapes using tilted angle $\theta = 19^\circ$ for the first time, $\theta = 17.5^\circ$ for the second time, and $\theta = 17^\circ$ for the third time evaporation, respectively.

angle $\theta = 25^\circ$ for the two-SRR sample, and $\theta = 23^\circ$ for the two-3D SRR sample, but the size of each set structures is definitely different. The second set ring structures, which are evaporated in the second fabrication cycle, show a larger radius r than that of the first set, due to a larger thickness h_0 of the second spin coated PMMA layer. In order to obtain the same structure size for the first and second fabrication cycle, we introduce a correction factor $\Delta\theta = -1.5^\circ$. As shown in Figure 8.5c, the 3D SRR structures fabricated in the second cycle using a tilted evaporation angle $\theta_{2nd} = 19^\circ - 1.5^\circ = 17.5^\circ$, show the same size as the structures fabricated in the first cycle with $\theta_{1st} = 19^\circ$. For the third fabrication cycle, we use only 0.5° smaller evaporation angle than that in the second cycle, but the structures show already slightly smaller size than the ones in the second set, which means there is nearly no difference in the PMMA layer thickness which is spin coated on the samples with one and two set fabricated nanostructures on them. The very slightly increased concentration of the nanostructures on the substrate does not affect the surface hydrophobicity of the sample. Therefore, to achieve the same structure size in each fabrication cycle, we only need to use the correction factor $\Delta\theta$ of -1.5° for the second cycle, and then for the rest fabrication process always the same parameters as used for second cycle. Based on this, we can vary the structure size of each set elements of one single metasurface very precisely and reproducibly.

8.3 Multishape plasmonic nanostructures

Figure 8.6 shows the results of three different multi-shape single-layer metasurfaces fabricated with repetitive hole-mask lithography. In the SEM images (shown in the first row) clearly different structure geometries together on the same substrate with well separated arrangement are observed. All samples are measured using FTIR spectroscopy with 0° (black curve) and 90° (red curve) polarization (shown in the second row), as defined in the upper-right corner in Figure 8.6b. FDTD code is used for the simulations, which are shown in the third row. The period used in the simulation is the average distance of the neighbouring structures, which depends on the coverage over the entire substrate.

The first example is a two-shape sample, consisting of gold SRRs and disks (Figure 8.6a). In the spectra we see the typical first- and third-order SRR modes at about 3500 nm and 1400 nm for 0° polarization, and the second-order plasmon mode at around 1900 nm for 90° polarization. Additionally, a polarization-independent dipole mode of the disks is clearly observed at about 800 nm. The simulation agrees very well with our experimental results, except there is substantially larger spectral broadening of all the measured resonances due to the relative inhomogeneity of our large-area samples. As the SRR structures can be used for antenna-enhanced SEIRA to detect a monolayer of molecules, which is discussed in detail in chapter 4, and the disk structures provide a plasmon resonance near the visible range, this sample can combine SEIRA for molecules with vibrational modes around 1900 nm and 3500 nm and SERS with excitation around 800 nm for simultaneous measurements [140]. The plasmonic resonances can be modified very flexibly for different requirements using different fabrication parameters.

Particularly, for vibrational detection of various substances, it is essential to obtain infrared spectra of the entire fingerprint region, which means that several vibration bands should be plasmonically amplified. For example, ultrasensitive detection of TNT requires observation of the vibration bands at 6.45 and 7.4 μm [141]. RDX as another dangerous explosive exhibits fingerprint vibrations at 6.3, 7.5, 8.0, and 9.7 μm [142]. Commonly, very expensive quantum cascade lasers are used for this detection, and the whole vibrational region of interest cannot be spanned by a single laser. A simple resonant antenna chip with four different antenna sizes matching their plasmonic resonances with the vibrational bands, fabricated by our novel repetitive colloidal hole lithography method, would easily create a single substrate that can be used in a cheap compact FTIR spectrometer for this standoff detection.

Figure 8.6b shows another two-shape sample consisting of SRRs with two different sizes and perpendicular gap directions. Multi-resonance spectra can be easily achieved through this design. For 90° polarization, the first-order SRR mode

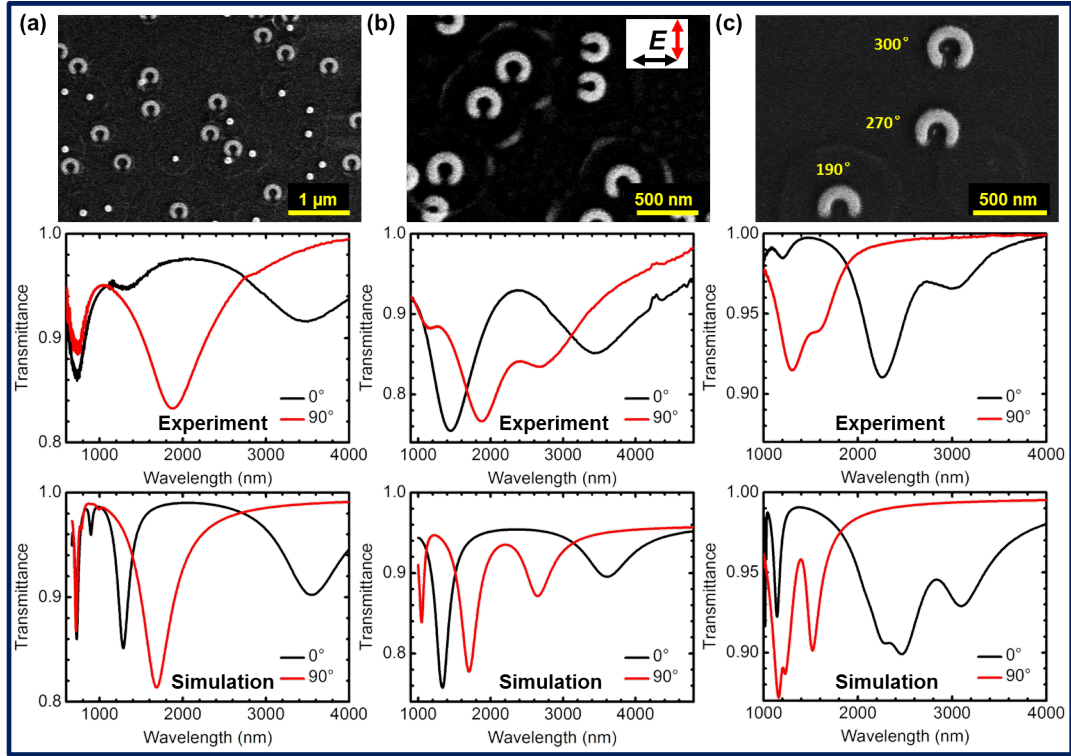


Figure 8.6: A variety of different multishape nanostructures fabricated by multiple repetition of hole-mask colloidal nanolithography (shown in the first row) and the corresponding optical spectra from FTIR measurements (shown in the second row) and FDTD simulations (shown in the third row). All the samples are measured with 0° (black curve) and 90° (red curve) polarization, which are defined and depicted in the Figure 8.6b upper-right corner. (a) Gold SRRs combined with disk structures. (b) Two different sized SRR structures with orthogonal gap directions. (c) Three-repetition SRR sample with different arc lengths.

of the smaller structures lies at about 2800 nm, the third-order mode at about 1200 nm, while the second-order mode of the larger structures is at around 1900 nm and these three modes are readily observed in both experimental and simulated spectra. However, for 0° polarization we only see two resonances: the first-order mode of the larger SRRs at about 3500 nm and one strong dip at around 1400 nm. This well-modulated resonance is due to the overlap of the second-order mode of the smaller SRRs and the third-order mode of the larger SRRs. This phenomenon indicates that by suitable design of multishape samples, we can also reduce the number of resonances in the multiline spectra or enhance the modulation depth of the expected resonance. Actually, a single-SRR sample already exhibits three resonances simultaneously under 45° polarization illumination, as discussed in chapter 4.3, but it is difficult to tune all the resonances independently. With this two-SRR design, more tunable resonances for a possible multi-line resonant SEIRA measurement are obtained, which is important for detection of a large number of different vibrational modes in a single molecule or even several different molecules at the same time. This sample might be modified in the future to serve as plasmonic parity-time (PT)-asymmetric metasurface [143] in the visible or near-IR for the case when two different materials are used and the resonances are kept the same. Our method would constitute a very elegant and simple fashion to achieve this functionality over large areas.

For many applications broadband spectra are required. Figure 8.6c shows one of the possible designs: a three-SRR-shape sample fabricated with three-repetition of hole-mask lithography. The three SRR geometries have the same radius and gap directions but different arc lengths, which are easily prepared by changing the evaporation parameters. The differences in the arc lengths are adjusted to ensure that the excited plasmon modes of the three SRRs are close enough to realize broadband features around 2000~3000 nm.

8.4 Large-area C_3 -symmetric 3D SRRs as chiral metamaterials

With the combination of the multishape deposition and 3D fabrication, even more flexible and complex structure designs can be realized, for example, large-area C_3 -symmetric chiral metasurfaces [15, 144, 145], which exhibit optical circular dichroism.

Figure 8.7 shows large-area 3D SRRs, which exhibit C_1 -, birefringent-, or even C_3 -symmetry, with the red arrows pointing to different gap directions in these samples. In principle, one could also stack different twisted layers above each other to realize a chiral design [146]. However, in this case, the relative alignment

plays a crucial role [147]. Additionally, stacking does not allow for interaction of the submersed layers with materials on the surface [148], for example in the case of refractive index sensing or SERS/SEIRA. Moreover, even though a C_1 -symmetric sample shows a signal when measured in a CD spectrometer, this signal arises due to elliptical birefringence and is not true evidence for circular dichroism. Only C_3 - or C_4 -symmetric nanostructures will exhibit optical chirality, as discussed in reference [2] (SI).

In order to demonstrate the potential of our multishape fabrication technique for creating novel optical functions in materials, we experimentally verify the optical CD of all the 3D SRR samples. Chiral structures cannot be superimposed on their mirror images [149], and the left- or right-handed version of them can only be distinguished from their interaction with circularly polarized light, therefore we usually examine the CD spectra to characterize them. As introduced before, we use $\Delta T = T_{RCP} - T_{LCP}$ to denote CD spectra in our experiment. A truly chiral structure with C_3 - or C_4 -symmetry, which makes the sample uniaxial in z -direction, shows an illumination direction ($+z$ and $-z$ direction) independent CD spectrum. Due to elliptical birefringence arising from the biaxiality of non- C_3 - or C_4 -symmetric samples, contributions of polarization conversion are expected to the measured spectra, which would change the sign of CD spectra for different illumination directions. CD of birefringent samples can be calculated with the formula 8.1. In consequence we measure transmittance of all our 3D SRR samples for perpendicularly incident left- and right-handed circularly polarized light with both forward and backward light propagation, as shown in Figure 8.7. Figures 8.7a and 8.7b show the SEM images (top) and the measured CD spectra for both illumination directions (bottom) of C_1 - and birefringent symmetric right-handed 3D SRRs. The CD spectra of both samples measured with forward (black curve) and backward (red curve) illuminations exhibit nearly mirror symmetry with respect to the zero line, confirming that there is no true chirality in the C_1 - and birefringent symmetric samples. The maximum transmittance differences ΔT of the C_1 -symmetric sample are about 5% at around 2500 nm and 8% to 10% at around 1300 nm. These values agree with the positions of the first- and the second-order SRR modes, respectively. For the birefringent symmetric sample, one maximum ΔT of about 2% to 4% is observed at around 2200 nm, and the other one at about 1200 nm. The spectral features of the two samples are similar, due to the same design of the structure geometry. The small blue shift of the CD responses of the birefringent sample stems from the relative smaller SRR-size.

As shown in Figure 8.7c, the CD spectra of C_3 -symmetric left-handed 3D SRRs for forward and backward illuminations are qualitatively similar to each other, except for broadening and some shift of the resonance due to fabrication and measurement tolerances, which can be easily improved by more accurate

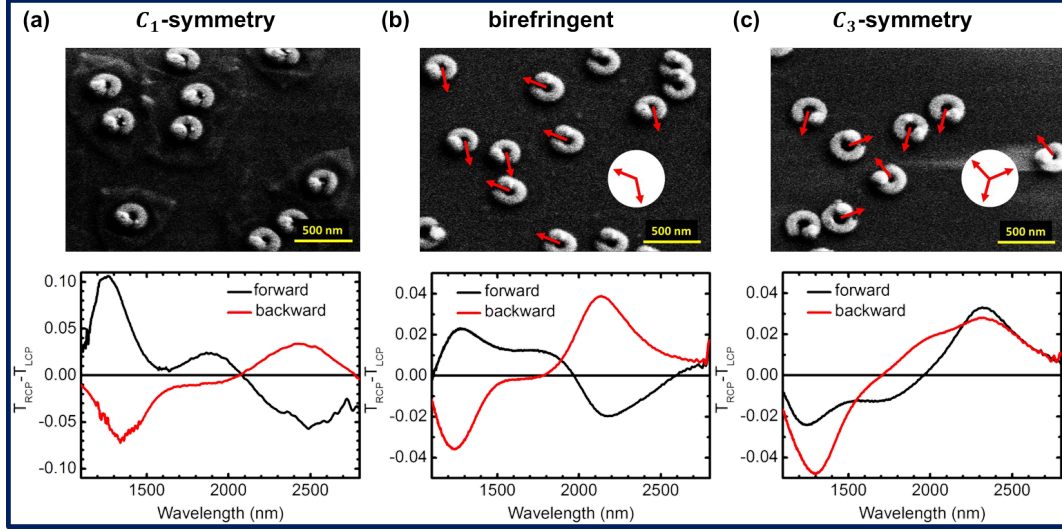


Figure 8.7: 3D SRRs with C_1 -symmetry (a), birefringent- (b) and C_3 -symmetry (c), which are fabricated via one, two, and three repetitions of hole-mask colloidal nanolithography, respectively. The SEM images are shown in the first row, with red arrows indicating the gap directions of the 3D SRRs. All the spectra are collected with an FTIR spectrometer using left-handed and right-handed circularly polarized light in forward (black curve) and backward (red curve) directions. In the second row we display the CD spectra of the three samples for both directions of illumination.

manufacturing in the future. However, compared to the samples in Figures 8.7a and 8.7b, this sample definitely exhibits the key signature of optical chirality, namely circular dichroism, which is independent of illumination directions. This confirms both the efficacy and the quality of our multishape fabrication method.

To further study the chirality of the samples, we compare the CD spectra of the 3D chiral SRRs with different handednesses. Figure 8.8a shows the SEM images of the right-handed and left-handed structures together with the corresponding CD spectra (blue label and curve for right-handed version and pink for left-handed version). It is clearly recognized that they exhibit opposite chiral responses, as expected. Again, two main resonances are observed at about 1300 nm and 2300 nm. Figure 8.8b depicts the corresponding simulations, which agree well with our experiment. The deviations arise mainly from the fact that the exact modeling of our experimental shape is very difficult. For simplicity a continuously sloping SRR shape is assumed, which is embedded in an average refractive index background material with $\varepsilon_{avg} = 1/2(\varepsilon_{air} + \varepsilon_{substrate})$. This is a somewhat idealized

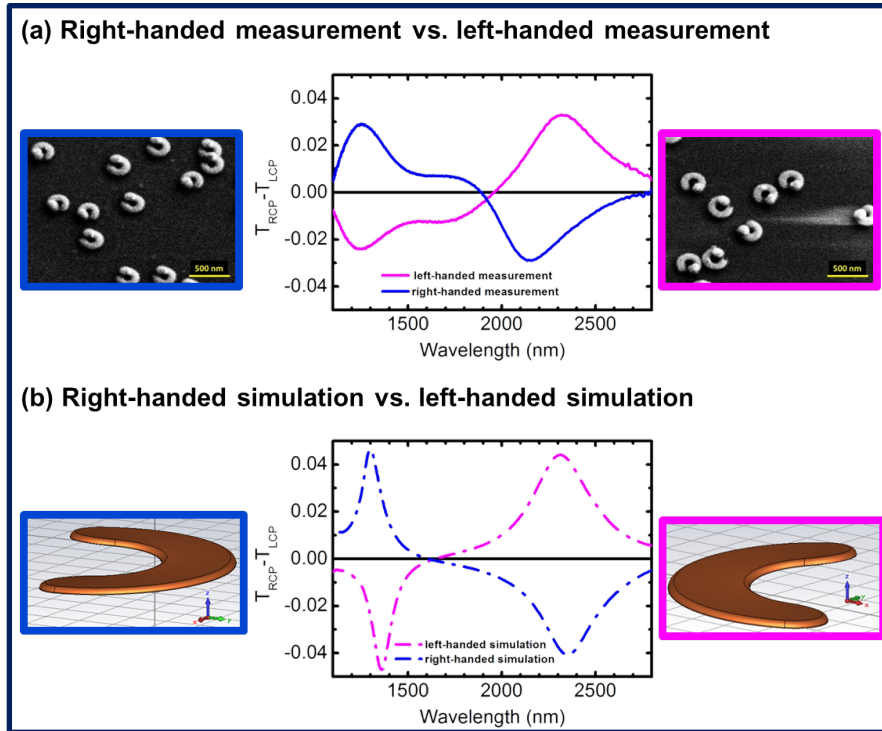


Figure 8.8: Comparison of the right-handed and left-handed 3D chiral SRRs. (a) SEM images of the right-handed chiral SRRs (blue label) and the C_3 -symmetric left-handed chiral SRRs (pink label). In the middle we show the calculated (as described above) CD spectrum (blue curve) of the right-handed sample compared to the forward measured CD spectrum (pink curve) of the left-handed sample. (b) Simulations of the right-handed (blue dash-dotted curve) and left-handed chiral SRRs (pink red dash-dotted curve).

scenario, as the real structure is a somewhat flatter SRR with one corner on the MgF_2 disk. Therefore, the theoretically predicted CD value is higher than the experimentally observed one, and the simulated resonances are much narrower without inhomogeneous broadening.

9 Summary and outlook

In conclusion, we demonstrated low-cost and large-area nanofabrication methods: hole-mask colloidal lithography and nanosphere lithography, in combination with angle-controlled evaporation for high-quality plasmonic nanostructures up to cm^2 size, which can be used for different applications, especially for sensing. The lower limit of the fabricated structure size is about 60 nm – 80 nm, due to the experimental limitations. The upper limit depends on the used PS sphere system. Small reproducible nanometer gaps over large areas, multiple materials, and 3D chiral structures are specifically well suited for our method.

We fabricated extremely homogeneous SRR metamaterials and proved their suitability for resonant antenna SEIRA enhancement up to 20000–fold. In particular, we showed high-quality asymmetric double SRRs with sharp and narrow optical Fano resonances in the near infrared, around $\lambda = 1.3 - 1.5 \mu\text{m}$, which are well suited for LSPR refractive index sensing with atto- or zeptoliter volumes. We achieve experimental sensitivities up to 520 nm/RIU and experimental figure of merit of 2.9. Annealing the sample at a temperature of 150 °C for 15 min can lead to a strong improvement of the shape and modulation depth of the Fano resonances due to reshaping of the metal during heating. Multi-particle oligomer geometries were presented, which can be fabricated reproducibly with sub–20 nm gaps, as well as in a gapless fashion with complex shapes. We analyzed the optical spectra and found fundamental as well as higher-order high-contrast plasmonic resonances. In gapless dimers with appropriate asymmetry, "self-induced" coupling between fundamental dipolar and higher-order plasmon modes within the same structures leads to well modulated Fano resonances. Refractive index sensors with a figure of merit more than 15 can be realized in these structures. With the large-area low-cost direct contact Au-Pd plasmonic hydrogen sensors, consisting of gold as lower disk and directly stacked palladium as upper disk, we obtain spectral shifts as large as 30 nm at about 4 vol.% H_2 , which is a strong improvement compared to previous indirect sensing designs. In the end, we demonstrated advanced use of hole-mask colloidal lithography with 3D and also multishape nanofabrications on the same substrate layer. These improvements allowed for great variety of structural design. We presented the flexibility of these fabrication methods on four different types of diverse plasmonic multishape single-layer metasurfaces with excellent optical functionality, namely plasmonic SRRs together with disks on a single substrate layer, which give a possible combination of SEIRA and SERS on the same sample;

9 Summary and outlook

an arrangement of differently oriented SRRs with different sizes, which would allow for multiline SEIRA measurements; a group of SRRs with different arc lengths at the same orientation, which give broadband resonant behavior; and finally C_3 -symmetric 3D chiral SRRs, which show truly chiral optical responses independent of propagation direction ($-z$ and $+z$).

In the future, we will improve the homogeneity of the low-coverage samples, prepared with hole-mask colloidal lithography, utilizing the critical Casimir forces [150] between the neighboring PS spheres, to realize large-area nanostructures with flexibly and well controlled densities, as well as periodic multishape metasurfaces. This is especially important to fabricate large-area plasmonic PT-asymmetric metasurfaces [143] in the visible or near-IR for the case when two different absorbing materials are used and the resonances are kept the same. These samples require very precisely control of the distance of the neighboring plasmonic elements, which can be tuned from the critical casimir potential [151] of the PS spheres.

Furthermore, our methods will allow the fabrication of low-cost and homogeneous large-area Fano-resonant asymmetric metamaterials [8] for plasmon-induced transparency assisted SEIRA, due to its ease of geometry variation. This should pave the road towards a whole new generation of low-cost high-efficiency infrared spectroscopy methods for pharmaceutical drug screening and few-biomolecule detection with zeptomolar sensitivity, thus making resonant plasmon-enhanced spectroscopy a standard bio- and medical lab tool.

Moreover, mass fabrication of low-cost large-area LSPR sensors with high sensitivities will be also realized soon. In addition, the large-area chiral metasurfaces will find use as tunable waveplates in the near- and mid-infrared spectral region, as enhancement antennas for vibrational circular dichroism, as well as chiral plasmonic enantiomer sensors [152], that could for example detect specifically glucose. These large-area fabrication methods will also open the door towards real-life plasmonic applications like optical gas sensors [115], biosensors [153], leak detectors [154], artificial nano-noses [155], and will be able to combine our structures in hybrid systems to engineer unprecedented functionalities in nanoplasmonic systems. This includes nonreciprocal materials such as bismuth iron garnet (BIG), that results in plasmonically enhanced Faraday rotation [13] or the magneto-optical Kerr effect; or materials such as palladium (Pd) or yttrium (Y) [156], which can give rise to complex plasmonic sensors; and also phase change materials such as VO_2 [157, 158].

Abbreviations

ADSR - asymmetric double split-ring resonator
AFM - atomic force microscopy
Au - gold
CaF₂ - calcium-fluoride
CD - circular dichroism
Cr - chromium
DFS - dark-field scattering
d-ODT - deuterated-octadecanethiol
FDTD - finite-difference time-domain
FEM - finite element method
FIT - finite integration technique
FOM - figure of merit
FTIR - Fourier transform infrared
FWHM - full width at half-maximum
IRRAS - infrared reflection absorption spectroscopy
LCP - left-handed circularly polarized
LSPR - localized surface plasmon resonance
MCT - mercury cadmium tellurium
NIR - near infrared
NMP - N-Methyl-2-pyrrolidone
ODT - octadecanethiol
Pd - palladium
PDDA - poly(diallyldimethylammonium chloride)
PMMA - poly(methylmethacrylate)
PS - polystyrene
PT - parity-time
RCP - right-handed circularly polarized
RIU - refractive index unit
SEIRA - surface-enhanced infrared absorption
SEM - scanning electron microscope
SERS - surface-enhanced Raman scattering
SPASER - surface plasmon laser
SRR - split-ring resonator

UV - ultraviolet
VIS - visible

Bibliography

- [1] Hentschel, M., Saliba, M., Vogelgesang, R., Giessen, H., Alivisatos, A. P., and Liu, N. *Nano Lett.* **10**, 2721 (2010).
- [2] Hentschel, M., Schäferling, M., Weiss, T., Liu, N., and Giessen, H. *Nano Lett.* **12**, 2542 (2012).
- [3] Smith, D. R., Padilla, W. J., Vier, D. C., Nemat-Nasser, S. C., and Schultz, S. *Phys. Rev. Lett.* **84**, 4184 (2000).
- [4] Neubrech, F., Kolb, T., Lovrincic, R., Fahsold, G., Pucci, A., Aizpurua, J., Cornelius, T. W., Toimil-Molares, M. E., Neumann, R., and Karim, S. *Appl. Phys. Lett.* **89**, 253140 (2006).
- [5] Neubrech, F., Pucci, A., Cornelius, T. W., Karim, S., Garcia-Etxarri, A., and Aizpurua, J. *Phys. Rev. Lett.* **101**, 157403 (2008).
- [6] Haes, A. J. and Duyne, R. P. V. *J. AM. CHEM. SOC.* **124**, 10596 (2002).
- [7] Fedotov, V. A., Rose, M., Prosvirnin, S. L., Papasimakis, N., and Zheludev, N. I. *Phys. Rev. Lett.* **99**, 147401 (2007).
- [8] Wu, C., Khankaev, A., Adato, R., Arju, N., Yanik, A. A., Altug, H., and Shvets, G. *Nat. Mater.* **11**, 69 (2012).
- [9] Gallinet, B. and Martin, O. J. F. *Phys. Rev. B* **83**, 235427 (2011).
- [10] Liu, N., Tang, M. L., Hentschel, M., Giessen, H., and Alivisatos, A. P. *Nat. Mater.* **10**, 631 (2011).
- [11] Stockman, M. I. *Phys. Rev. Lett.* **106**, 156802 (2011).
- [12] Noginov, M. A., Zhu, G., Belgrave, A. M., Bakker, R., Shalaev, V. M., Narimanov, E. E., Stout, S., Herz, E., Suteewong, T., and Wiesner, U. *Nature* **460**, 1110 (2009).
- [13] Chin, J. Y., Steinle, T., Wehlius, T., Dregely, D., Weiss, T., Belotelov, V. I., Stritzker, B., and Giessen, H. *Nat. Commun.* **4**, 1599 (2013).

- [14] Stern, L., Desiatov, B., Goykhman, I., and Levy, U. *Nat. Commun.* **4**, 1548 (2013).
- [15] Helgert, C., Pshenay-Severin, E., Falkner, M., Menzel, C., Rockstuhl, C., Kley, E., Tünnermann, A., Lederer, F., and Pertsch, T. *Nano Lett.* **11**, 4400 (2011).
- [16] Bergmair, I., Dastmalchi, B., Bergmair, M., Saeed, A., Hilber, W., Hesser, G., Helgert, C., Pshenay-Severin, E., Pertsch, T., Kley, E. B., Hübner, U., Shen, N. H., Penciu, R., Kafesaki, M., Soukoulis, C. M., Hingerl, K., Muehlberger, M., and Schoeftner, R. *Nanotechnology* **22**, 325301 (2011).
- [17] Aksu, S., Yanik, A. A., Adato, R., Artar, A., Huang, M., and Altug, H. *Nano Lett.* **10**, 2511 (2010).
- [18] Fischer, J., von Freymann, G., and Wegener, M. *Adv. Mater.* **22**, 3578 (2010).
- [19] Gansel, J. K., Thiel, M., Rill, M. S., Decker, M., Bade, K., Saile, V., von Freymann, G., Linden, S., and Wegener, M. *Science* **325**, 1513 (2009).
- [20] Radlke, A., Gissibl, T., Klotzbücher, T., Braun, P. V., and Giessen, H. *Adv. Mater.* **23**, 3018 (2011).
- [21] Spallas, J. P., Hawryluk, A. M., and Kania, D. R. *J. Vac. Sci. Technol. B* **13**, 1973 (1995).
- [22] Zhang, X., Sun, B., Friend, R. H., Guo, H., Nau, D., and Giessen, H. *Nano Lett.* **6**, 651 (2006).
- [23] Yin, X., Schäferling, M., Metzger, B., and Giessen, H. *Nano Lett.* **13**, 6238 (2013).
- [24] Kuzyk, A., Schreiber, R., Fan, Z., Pardatscher, G., Roller, E., Högele, A., Simmel, F. C., Govorov, A. O., and Liedl, T. *Nature* **483**, 311 (2012).
- [25] Fan, Z. and Govorov, A. O. *Nano Lett.* **10**, 2580 (2010).
- [26] Fan, Z. and Govorov, A. O. *Nano Lett.* **12**, 3283 (2012).
- [27] Decker, M., Klein, M. W., Wegener, M., and Linden, S. *Opt. Lett.* **32**, 856 (2007).
- [28] Husnik, M., Linden, S., Diehl, R., Niegemann, J., Busch, K., and Wegener, M. *Phys. Rev. Lett.* **109**, 233902 (2012).

- [29] Filter, R., Slowik, K., Straubel, J., Lederer, F., and Rockstuhl, C. *Opt. Lett.* **39**, 1246 (2014).
- [30] MacDonald, K. F., Samson, Z. L., Stockman, M. I., and Zheludev, N. I. *Nat. Photon.* **3**, 55 (2009).
- [31] Ren, M., Plum, E., Xu, J., and Zheludev, N. I. *Nat. Commun.* **3**, 833 (2012).
- [32] Fredriksson, H., Alaverdyan, Y., Dmitriev, A., Langhammer, C., Sutherland, D. S., Zäch, M., and Kasemo, B. *Adv. Mater.* **19**, 4297 (2007).
- [33] Shegai, T., Chen, S., Miljkovic, V. D., Zengin, G., Johansson, P., and Käll, M. *Nat. Commun.* **2**, 481 (2011).
- [34] Banthi, J. C., Meneses-Rodriguez, D., Garcia, F., Gonzalez, M. U., Garcia-Martin, A., Cebollada, A., and Armelles, G. *Adv. Mater.* **24**, 36 (2012).
- [35] Fischer, U. C. and Zingsheim, H. P. *J. Vac. Sci. Technol.* **19**, 881 (1981).
- [36] Haynes, C. L. and Van Duyne, R. P. *J. Phys. Chem. B* **105**, 5599 (2001).
- [37] Kosiorek, A., Kandulski, W., Glaczynska, H., and Giersig, M. *Small* **1**, 439 (2005).
- [38] Gwinner, M., Koroknay, E., Fu, L., Patoka, P., Kandulski, W., Giersig, M., and Giessen, H. *Small* **5**, 400–406 (2009).
- [39] Langhammer, C., Zoric, I., Kasemo, B., and Clemens, B. M. *Nano Lett.* **7**, 3122 (2007).
- [40] Shegai, T., Johansson, P., Langhammer, C., and Käll, M. *Nano Lett.* **12**, 2464 (2012).
- [41] Frank, B., Yin, X., Schäferling, M., Zhao, J., Hein, S. M., Braun, P. V., and Giessen, H. *ACS Nano* **7**, 6321 (2013).
- [42] Dmitriev, A., Pakizeh, T., Käll, M., and Sutherland, D. S. *Small* **3**, 294 (2007).
- [43] Esteban, R., Vogelgesang, R., Dorfmann, J., Dmitriev, A., Rockstuhl, C., Etrich, C., and Kern, K. *Nano Lett.* **8**, 3155 (2008).
- [44] Syrenova, S., Wadell, C., and Langhammer, C. *Nano Lett.* **14**, 2655 (2014).
- [45] Nemiroski, A., Gonidec, M., Fox, J. M., Jean-Remy, P., Turnage, E., and Whitesides, G. M. *ACS Nano* **8**, 11061 (2014).

- [46] Novotny, L. and Hecht, B. *Principles of Nano-Optics*. Cambridge university press, (2008).
- [47] Bohren, C. F. and Huffman, D. R. *Absorption and Scattering of Light by Small Particles*. John Wiley & Sons, Inc, (1983).
- [48] Hummel, R. E. *Optische Eigenschaften von Metallen and Legierungen*. Springer Verlag, (1971).
- [49] Ashcroft, N. W. and Mermin, N. D. *Solid State Physics*. Saunders College Publishing, (1976).
- [50] Johnson, P. B. and Christy, R. W. *Phy. Rev. B* **6**, 4370–4379 (1972).
- [51] Kerker, M. *The Scattering of Light and other Electromagnetic Radiation*. Academic Press, (1969).
- [52] Moon, S., Kim, D. J., Kim, K., Kim, D., Lee, H., Lee, K., and Haam, S. *Appl. Opt.* **49**, 484–491 (2010).
- [53] Veselago, V. *Sov. Phys. Usp.* **10**, 8 (1968).
- [54] Engheta, N. and Ziolkowski, R. W., editors. *Metamaterials: Physics and Engineering Explorations*. Wiley & Sons, (2006).
- [55] Zouhdi, S., Sihvola, A., and Vinogradov, A. P., editors. *Metamaterials and Plasmonics: Fundamentals, Modelling, Applications*. New York: Springer-Verlag, (2008).
- [56] Pendry, J. and Smith, D. *Physics Today* **57**, 37–44 (2004).
- [57] Linden, S. and Wegener, M. *Physik Journal* **5**, 12 (2006).
- [58] Rockstuhl, C., Lederer, F., Etrich, C., Pertsch, T., and Scharf, T. *Phys. Rev. Lett.* **99**, 017401 (2007).
- [59] Sarychev, A. K., Shvets, G., and Shalaev, V. M. *Phy. Rev. E* **73**, 036609 (2006).
- [60] Wood, R. W. *Proc. R. Soc. Lond. Ser. A* **18**, 269 (1902).
- [61] Fano, U. *Phys. Rev.* **50**, 573 (1936).
- [62] Lukyanchuk, B., Zheludev, N. I., Maier, S. A., Halas, N. J., Nordlander, P., Giessen, H., and Chong, C. T. *Nat. Mater.* **9**, 707 (2010).

- [63] Alzar, C. L. G., Martinez, M. A. G., and Nussenzveig, P. *Am. J. Phys.* **70**, 37 (2002).
- [64] Joe, Y. S., Satanin, A. M., and Kim, C. S. *Phy. Scr.* **74**, 259 (2006).
- [65] Lamb, W. E. and Retherford, R. C. *Phy. Rev.* **84**, 222 (1951).
- [66] Wacker, A. Master's thesis, University Stuttgart, (2009).
- [67] McFarland, A. D., Young, M. A., Dieringer, J. A., and Van Duyne, R. P. *J. Phys. Chem. B* **109**, 11279 (2005).
- [68] Odom, T. W. and Nehl, C. L. *ACS Nano* **2**, 612 (2008).
- [69] Nordlander, P. *ACS Nano* **3**, 488 (2009).
- [70] Hao, F., Nordlander, P., Sonnefraud, Y., Dorpe, P., and Maier, S. *ACS Nano* **3**, 643–652 (2009).
- [71] Kundu, J., Le, F., Nordlander, P., and Halas, N. J. *Chem. Phys. Lett.* **452**, 115 (2008).
- [72] Le, F., Brandl, D. W., Urzhumov, Y. A., Wang, H., Kundu, J., Halas, N. J., Aizpurua, J., and Nordlander, P. *ACS Nano* **2**, 707 (2008).
- [73] Cubukcu, E., Zhang, S., Park, Y. S., Bartal, G., and Zhang, X. *Appl. Phys. Lett.* **95**, 043113 (2009).
- [74] Prycet, I. M., Kelaitat, Y. A., Aydint, K., and Atwater, H. A. *ACS Nano* **5**, 8167 (2011).
- [75] Lahiri, B., Khokhar, A. Z., De La Rue, R. M., McMeekin, S. G., and Johnson, N. P. *Opt. Express* **17**, 1107 (2009).
- [76] Lahiri, B., McMeekin, S. G., Rue, R. M. D. L., and Johnson, N. P. *Appl. Phys. Lett.* **98**, 153116 (2011).
- [77] Schreiber, F. *Prog. Surf. Sci.* **65**, 151 (2000).
- [78] Yang, C. S. C., Richter, L. J., Stephenson, J. C., and Briggman, K. A. *Langmuir* **18**, 7549 (2002).
- [79] Aizpurua, J., Bryant, G. W., Richter, L. J., de Abajo, F. J. G., Kelley, B. K., and Mallouk, T. *Phy. Rev. B* **71**, 235420 (2005).
- [80] Zuloaga, J. and Nordlander, P. *Nano Lett.* **11**, 1280 (2011).

- [81] Enders, D. and Pucci, A. *Appl. Phys. Lett.* **88**, 184104 (2006).
- [82] Adato, R., Yanik, A. A., Amsden, J. J., Kaplan, D. L., Omenetto, F. G., Hong, M. K., Erramilli, S., and Altug, H. *Proc. Natl. Acad. Sci. U.S.A.* **106**, 19227 (2009).
- [83] Raether, H. *Surface Plasmons*. Springer-Verlag, (1986).
- [84] Halas, N. J., Lal, S., Chang, W., Link, S., and Nordlander, P. *Chem. Rev.* **111**, 3913 (2011).
- [85] Zhang, S., Genov, D. A., Wang, Y., Liu, M., and Zhang, X. *Phys. Rev. Lett.* **101**, 047401 (2008).
- [86] Tassin, P., Zhang, L., Koschny, T., Economou, E. N., and Soukoulis, C. M. *Phys. Rev. Lett.* **102**, 05390 (2009).
- [87] Liu, N., Langguth, L., Weiss, T., Kästel, J., Fleischhauer, M., Pfau, T., and Giessen, H. *Nat. Mater.* **8**, 758 (2009).
- [88] Dregely, D., Hentschel, M., and Giessen, H. *ACS Nano* **5**, 8202 (2011).
- [89] Liu, N., Weiss, T., Mesch, M., Langguth, L., Eigenthaler, U., Hirscher, M., Sönnichsen, C., and Giessen, H. *Nano Lett.* **10**, 1103 (2010).
- [90] Becker, J., Trügler, A., Jakab, A., Hohenester, U., and Sönnichsen, C. *Plasmonics* **5**, 161 (2010).
- [91] Lal, S., Link, S., and Halas, N. J. *Nat. Photon.* **1**, 641 (2007).
- [92] Liao, H., Nehl, C. L., and Hafner, J. H. *Nanomedicine* **1**, 201 (2006).
- [93] Singh, R., Al-Naib, I. A. I., Yang, Y., Chowdhury, D. R., and Cao, W. *Appl. Phys. Lett.* **99**, 201107 (2011).
- [94] Al-Naib, I. A. I., Jansen, C., Born, N., and Koch, M. *Appl. Phys. Lett.* **98**, 091107 (2011).
- [95] Chen, K., Drachev, V. P., Borneman, J. D., Kildishev, A. V., and Shalaev, V. M. *Nano Lett.* **10**, 916 (2010).
- [96] Shao, L., Ruther, M., Linden, S., Essig, S., Busch, K., Weissmüller, J., and Wegener, M. *Adv. Mater.* **22**, 5173 (2010).
- [97] Ruther, M., Shao, L., Linden, S., Weissmüller, J., and Wegener, M. *Appl. Phys. Lett.* **98**, 013112 (2011).

- [98] Young, T. F., Chang, J. F., and Ueng, H. Y. *Thin Solid Films* **322**, 319 (1998).
- [99] Willets, K. A. and Duynne, R. P. V. *Annu. Rev. Phys. Chem.* **58**, 267–297 (2007).
- [100] Sherry, L. J., Chang, S. H., Schatz, G. C., Duynne, R. P. V., Wiley, B. J., and Xia, Y. *Nano Lett.* **5**, 2034 (2005).
- [101] Mirin, N., K.Bao, and Nordlander, P. *J. Phy. Chem. A* **113**, 4028–4034 (2009).
- [102] Mirin, N. A., Bao, K., and Nordlander, P. *J. Phys. Chem. A* **113**, 4028 (2009).
- [103] Lassiter, J. B., Sobhani, H., Fan, J. A., Kundu, J., Capasso, F., Nordlander, P., and Halas, N. J. *Nano Lett.* **10**, 3184 (2010).
- [104] Fan, J. A., Wu, C. H., Bao, K., Bao, J. M., Bardhan, R., Halas, N. J., Manoharan, V. N., Nordlander, P., Shvets, G., and Capasso, F. *Science* **328**, 1135 (2010).
- [105] Brandl, D. W., Mirin, N. A., and Nordlander, P. *J. Phys. Chem. B* **110**, 12302–12310 (2006).
- [106] Alegret, J., Rindzevicius, T., Pakizeh, T., Alaverdyan, Y., Gunnarsson, L., and Käll, M. *J. Phy. Chem. C* **112**, 14313 (2008).
- [107] Fan, J. A., Bao, K., Wu, C. H., Bao, J. M., Bardhan, R., Halas, N. J., Manoharan, V. N., Shvets, G., Nordlander, P., and Capasso, F. *Nano Lett.* **10**, 4680 (2010).
- [108] Rahmani, M., Tahmasebi, T., Lin, Y., Lukyanchuk, B., Liew, T. Y. F., and Hong, M. H. *Nanotechnology* **22**, 245204 (2010).
- [109] Rahmani, M., Lukyanchuk, B., Ng, B., Tavakkoli, K. G. A., Liew, T. Y. F., and Hong, M. H. *Opt. Express* **19**, 4949 (2011).
- [110] Papasimakis, N., Fedotov, V. A., Zheludev, N. I., and Prosvirnin, S. L. *Phys. Rev. Lett.* **101**, 253903 (2008).
- [111] Chen, J. X., Wang, P., Chen, C. C., Lu, Y. H., Ming, H., and Zhan, Q. W. *Opt. Express* **19**, 5970 (2011).
- [112] Mukherjee, S., Sobhani, H., Lassiter, J. B., Bardhan, R., Nordlander, P., and Halas, N. J. *Nano Lett.* **10**, 2694 (2010).

- [113] Stockman, M. I. *Nature* **467**, 541 (2010).
- [114] Verellen, N., Sonnefraud, Y., Sobhani, H., Hao, F., Moshchalkov, V. V., Dorpe, P. V., Nordlander, P., and Maier, S. A. *Nano Lett.* **9**, 1663 (2009).
- [115] Tittl, A., Mai, P., Taubert, R., Dregely, D., Liu, N., and Giessen, H. *Nano Lett.* **11**, 4366 (2011).
- [116] Zhang, S. P., Bao, K., Halas, N. J., Xu, H. X., and Nordlander, P. *Nano Lett.* **11**, 1657 (2011).
- [117] Fang, Z., Cai, J., Yan, Z., Nordlander, P., Halas, N. J., and Zhu, X. *Nano Lett.* **11**, 1657 (2011).
- [118] Hentschel, M., Dregely, D., Vogelgesang, R., Giessen, H., and Liu, N. *ACS Nano* **5**, 2042 (2011).
- [119] Hao, F., Sonnefraud, Y., Dorpe, P. V., and Maier, S. A. *Nano Lett.* **8**, 3983 (2008).
- [120] Yoshimura, K., Langhammer, C., and Dam, B. *MRS Bulletin* **38**, 495 (2013).
- [121] Zoric, I., Larsson, E. M., Kasemo, B., and Langhammer, C. *Adv. Mater.* **22**, 4628 (2010).
- [122] Langhammer, C., Larsson, E. M., Zhdanov, V. P., and Zoric, I. *J. Phy. Chem. C* **116**, 21201 (2012).
- [123] Bardhan, R., Hedges, L. O., Pint, C. L., Javey, A., Whitelam, S., and Urban, J. J. *Nat. Mater.* **12**, 905 (2013).
- [124] Langhammer, C., Larsson, E. M., Kasemo, B., and Zoric, I. *Nano Lett.* **10**, 3529 (2010).
- [125] Wadell, C., Antosiewicz, T. J., and Langhammer, C. *Nano Lett.* **12**, 4784 (2012).
- [126] Tittl, A., Yin, X., Giessen, H., Tian, X.-D., Tian, Z.-Q., Kremers, C., Chigrin, D. N., and Liu, N. *Nano Lett.* **12**, 1816 (2013).
- [127] Lewis, F. A. *Int. J. Hydrogen Energy* **20**, 587 (1995).
- [128] Frazier, G. A. and Glosser, R. *J. Phys. D: Appl. Phys.* **12**, L113 (1979).
- [129] Shegai, T. and Langhammer, C. *Adv. Mater.* **23**, 4409 (2011).

- [130] Rottkay, K. V., Rubin, M., and Duine, P. A. *J. Appl. Phys.* **85**, 408 (1999).
- [131] Dahlin, A. B., Tegenfeldt, J. O., and Hök, F. *Anal. Chem.* **78**, 4416 (2006).
- [132] Strohfeldt, N., Tittl, A., and Giessen, H. *Opt. Mater. Express* **3**, 194 (2013).
- [133] Taubert, R., Dregely, D., Stroucken, T., Christ, A., and Giessen, H. *Nat. Commun.* **3**, 691 (2012).
- [134] Davis, T. J. and Hendry, E. *Phys. Rev. B* **87**, 085405 (2013).
- [135] Eftekhari, F. and Davis, T. J. *Phys. Rev. B* **86**, 075428h (2012).
- [136] Hendry, E., Mikhaylovskiy, R. V., Barron, L. D., Kadodwala, M., and Davis, T. J. *Nano Lett.* **12**, 3640 (2012).
- [137] Decker, M., Ruther, M., Kriegler, C. E., Zhou, J., Soukoulis, C. M., Linden, S., and Wegener, M. *Opt. Lett.* **34**, 2501 (2009).
- [138] Hentschel, M., Wu, L., Schäferling, M., Bai, P., Li, E. P., and Giessen, H. *ACS Nano* **6**, 10355 (2012).
- [139] Liu, N. and Giessen, H. *Angew. Chem.* **49**, 9838 (2010).
- [140] D'Andrea, C., Bochterle, J., Toma, A., Huck, C., Neubrech, F., Messina, E., Fazio, B., Marago, O. M., Fabrizio, E. D., de La Chapelle, M. L., Gucciardi, P. G., and Pucci, A. *ACS Nano* **7**, 3522 (2013).
- [141] Pushkarsky, M. B., Dunayevskiy, I. G., Prasanna, M., Tsekoun, A. G., Go, R., and Patel, C. K. N. *Proc. Natl. Acad. Sci. USA* **103**, 19630 (2006).
- [142] Morales-Rodríguez, M. E., Senesac, L. R., Rajic, S., Lavrik, N. V., Smith, D. B., and Datskos, P. G. *Opt. Lett.* **38**, 507 (2013).
- [143] Lawrence, M., Xu, N., Zhang, X., Cong, L., Han, J., Zhang, W., and Zhang, S. *Phys. Rev. Lett.* **113**, 093901 (2014).
- [144] Rockstuhl, C., Menzel, C., Paul, T., and Lederer, F. *Phys. Rev. B* **79**, 035321 (2009).
- [145] Menzel, C., Rockstuhl, C., Paul, T., and Lederer, F. *Appl. Phys. Lett.* **93**, 233106 (2008).
- [146] Zhao, Y., Belkin, M. A., and Alu, A. *Nat. Commun.* **3**, 870 (2012).
- [147] Hentschel, M., Schäferling, M., Metzger, B., and Giessen, H. *Nano Lett.* **13**, 600 (2013).

- [148] Schäferling, M., Yin, X., Engheta, N., and Giessen, H. *ACS Photon.* **1**, 530 (2014).
- [149] Thomson, W. H. and Kelvin, L. *Baltimore lecture*. C. J. Clay and Sons, (1884).
- [150] Hertlein, C., Helden, L., Gambassi, A., Dietrich, S., and Bechinger, C. *Nature* **451**, 172 (2008).
- [151] Gambassi, A., Maciolek, A., Hertlein, C., Nellen, U., Helden, L., Bechinger, C., and Dietrich, S. *Phy. Rev. E* **80**, 061143 (2009).
- [152] Ghosh, A. and Fischer, P. *Phys. Rev. Lett.* **97**, 173002 (2006).
- [153] Yanik, A. A., Cetin, A. E., Huang, M., Artar, A., Mousavi, S. H., Khanikaev, A., Connor, J. H., Shvets, G., and Altug, H. *PNAS* **108**, 11784 (2011).
- [154] Bévenot, X., Trouillet, A., Veillas, C., Gagnaire, H., and Clément, M. *Sensors and Actuators B* **67**, 57 (2000).
- [155] Gardner, J. W. and Bartlett, P. N. *Sensors and Actuators B* **18**, 210 (1994).
- [156] Strohfeldt, N., Tittl, A., Schäferling, M., Neubrech, F., Kreibig, U., Griessen, R., and Giessen, H. *Nano Lett.* **14**, 1140 (2014).
- [157] Appavoo, K., Lei, D. Y., Sonnefraud, Y., Wang, B., Pantelides, S. T., Maier, S. A., and Haglund, Jr., R. F. *Nano Lett.* **12**, 780 (2012).
- [158] Michel, A.-K. U., Chigrin, D. N., Maß, T. W. W., Schönauer, K., Salinga, M., Wuttig, M., and Taubner, T. *Nano Lett.* **13**, 3470 (2013).

Acknowledgement

I would like to thank all the people who have helped me in this work:

- **Prof. Dr. Harald Giessen** for giving me this interesting topic, for enlightening me on different new ideas, and for the tremendous support during my work.
- **Prof. Dr. Clemens Bechinger** for kindly being my second reviser.
- **Prof. Dr. Günter Wunner** for kindly being the chairman of my PhD examination.
- **Prof. Dr. Paul V. Braun** and **Chunjie Zhang** for many useful suggestions in my experiment and for the help for most of my publications.
- **Prof. Dr. Paul Mulvaney** and **Sarah Jaber** for the collaboration to improve the fabrication techniques and to receive more beautiful results.
- **Dr. Sven Burger** for his help with the simulations of my oligomer structures, and **Dr. Frank Neubrech** for the SEIRA measurements.
- **Bettina Frank** for her great help in my experiments and many helpful discussions during my work, and for her proof reading of this thesis.
- **Nikolai Strohfeldt** for his great help with the measurements and discussions.
- **Dr. Venla Manninen** for her proof reading of this thesis.
- **Monika Ubl** and **Ramon Walter** for their support and kind help in the clean room.
- **All my dear colleagues in 4th Physics Institute** for the friendly working atmosphere and for all their help in my work.
- **Dr. Christine von Rekowski** for her support in administrative stuffs.
- last, but not least, my husband **Peng Li** and my **family** for their support and solicitude from China.

Curriculum vitae

JUN ZHAO

Engelboldstrasse 95

70569 Stuttgart

joanna.zhao10222@gmail.com



PROFESSIONAL OVERVIEW

Jun Zhao (★22.10.1983) graduated from University of Stuttgart with a diploma in Physics in 2010 and started her Ph.D. thesis on low-cost fabrication of large-area complex plasmonic nanostructures for sensing applications.

EDUCATION

- 2010 Diplom-Physikerin (Master of Science): Physics
University of Stuttgart - Stuttgart, Germany
- 2003 Bachelor of Science: Physics
University of Wuhan - Wuhan, Hubei, China
- 2002 High School Diploma
Wuhan No. 2 Middle School - Wuhan, Hubei, China

PROFESSIONAL EXPERIENCE

- 05/2010 – now Scientific assistant
University of Stuttgart
Fabrication of large-area plasmonic nanostructures
Localized surface plasmon resonance sensing application
Advisor for Advanced Physical Laboratory
- 03/2007 – 04/2010 Student assistant
University of Stuttgart
Evaporation in high vacuum
Optical measurements of plasmonic nanostructures
- 02/2007 – 03/2007 Office worker
IBM - Stuttgart

FELLOWSHIPS AND AWARDS

Chinese government award for outstanding self-financed students abroad 2012

